THE EFFECT OF ASPECT RATIO ON THE AERODYNAMIC FORCES AND FREE END PRESSURE DISTRIBUTION FOR A SURFACE-MOUNTED FINITE HEIGHT CYLINDER

A Thesis Submitted to the College of
Graduate and Postdoctoral Studies
In Partial Fulfillment of the Requirements
For the Degree of Master of Science
In the Department of Mechanical Engineering
University of Saskatchewan
Saskatoon

By

Adam Beitel

Permission to Use

In presenting this thesis/dissertation in partial fulfillment of the requirements for a Postgraduate degree from the University of Saskatchewan, I agree that the Libraries of this University may make it freely available for inspection. I further agree that permission for copying of this thesis/dissertation in any manner, in whole or in part, for scholarly purposes may be granted by the professor who supervised my thesis/dissertation work or, in their absence, by the Head of the Department or the Dean of the College in which my thesis work was done. It is understood that any copying or publication or use of this thesis/dissertation or parts thereof for financial gain shall not be allowed without my written permission. It is also understood that due recognition shall be given to me and to the University of Saskatchewan in any scholarly use which may be made of any material in my thesis/dissertation.

DISCLAIMER

Reference in this thesis/dissertation to any specific commercial products, process, or service by trade name, trademark, manufacturer, or otherwise, does not constitute or imply its endorsement, recommendation, or favoring by the University of Saskatchewan. The views and opinions of the author expressed herein do not state or reflect those of the University of Saskatchewan, and shall not be used for advertising or product endorsement purposes.

Requests for permission to copy or to make other uses of materials in this thesis/dissertation in whole or part should be addressed to:

Head of the Department of Mechanical Engineering

57 Campus Drive

University of Saskatchewan

Saskatoon, Saskatchewan S7J 5A9

Canada

OR

Dean

College of Graduate and Postdoctoral Studies

University of Saskatchewan

105 Administration Place

Saskatoon, Saskatchewan S7N 5A2

Canada

Abstract

The surface-mounted finite-height cylinder is a fundamental engineering shape and can be found in a multitude of industrial applications. As a result, the local flow field is of great importance in the design of cylindrical components such as heat exchangers or buildings. While two-dimensional (2-D or "infinite") cylinders are well-understood, the effects of the ground plane and the cylinder free end are significant and require further study. Of particular interest in this thesis is the pressure distribution on the free end of the cylinder, and a mean normal force that develops from it. A vast majority of studies on this topic have focused on short cylinders with a small aspect ratio (AR = height/diameter). The work in this thesis is an attempt to characterize how the pressure distribution and mean aerodynamic forces are influenced by the aspect ratio of the cylinder and the boundary layer thickness of the flow. The little-researched mean normal force, the mean drag force and its resultant mean bending moment, and the associated vortex shedding in the wake are investigated, along with the mean surface pressures and pressure fluctuations for the cylinder free end. A cylinder was designed for use in measuring these parameters for 22 evenly spaced aspect ratios in a range from $0.5 \leq AR \leq 11$, and an additional cylinder and boundary layer were used to generate data for four different values of relative boundary layer thickness in the range $0.60 \leq \delta/D \leq 2.86$.

The results of this research fit in well with published data, and reveal that the flow regimes appear to be marked by two critical aspect ratios, located approximately at AR = 2.5 and AR = 6. Below the lower critical AR, the boundary layer and ground plane effects are dominant, and the Strouhal number and the mean drag and mean normal force coefficients are drastically reduced. The mean bending moment coefficient is high at low AR, possibly owing to the high point of action of the drag force caused by the velocity distribution in the boundary layer. Between the two critical aspect ratios, the mean force coefficients and Strouhal number are relatively insensitive to AR. Above the upper critical AR, the mean drag coefficient increases towards the value for a 2-D cylinder, while the mean normal force coefficient reduces, and is expected to approach a small, constant value. A vertical wall shear force that acts in the opposite direction of the free end pressures may account for the difference between the mean normal force results obtained from integration and those obtained from direct measurements. For high AR, the bending moment coefficient and point of action are relatively unchanged. The free end

pressure distributions reveal similar features to previously published data, including “eye-like” enclosed regions of minimum pressure on the upstream half of the cylinder face, and an enclosed region of maximum pressure on the downstream half of the cylinder face. The eye-like structures disappear above the upper critical AR, and are replaced with a band of minimum pressure, upon which the pressure distribution is no longer influenced by aspect ratio. These two critical AR, along with the free end surface pressures and aerodynamic forces, are influenced by the boundary layer thickness, such that a thicker boundary layer creates higher critical aspect ratios.

This work is among the first to use consistent flow conditions in showing the effect of two critical aspect ratios on multiple fluid forces and flow structures over a large range of AR. This includes the mean normal force and bending moment. The range of values for the critical aspect ratios is narrowed by the use of small incremental changes in the cylinder aspect ratio. The pressure distributions, and the pressure fluctuations, on the cylinder free end were established in greater detail than earlier published studies as well, and the effects of a change in aspect ratio and boundary layer thickness can be clearly seen. It is hoped that the work contained herein will be an aid to the design and optimization of finite cylinders in future engineering applications.

Acknowledgments

I would like to thank, first and foremost my supervisor, Professor David Sumner, for his advice, guidance and support throughout this project. Your insight was truly invaluable and this project would not be what it is without all your assistance. I've truly enjoyed getting to know you and work with you closely. I wish you the best in the future.

Thanks also to my advisory committee members, Professors J. D. Bugg and K. A. Mazurek for their suggestions and as I proceeded with the project. A special thanks also to Shawn Reinink, for all his help in keeping the wind tunnel in working order and handling every technical issue that arose, and Dan Vessey, for his craftsmanship and input on the cylinders. The entire faculty of the Department of Mechanical Engineering has been kind, welcoming, and helpful in my time as a Master's student, and I would like to extend my sincere gratitude to the faculty members who became friends and colleagues.

I would like to thank my fellow Master's students as well. You made every day here enjoyable and I will count you among my lifelong friends.

To my parents, siblings, and girlfriend, thank you for all you have done to support me over the course of this program. Your love and patience has helped me in many ways over the past two years.

Finally I would like to acknowledge the financial support from the University of Saskatchewan Graduate Scholarship, Dr. David Sumner, and the Natural Sciences and Engineering Research Council of Canada (NSERC), which is greatly appreciated.

Table of Contents

List of Symbols

English Symbols

A	Area of the cylinder free end [m^2]
AR	Aspect ratio, H/D
C_D	Mean drag coefficient
C_{ij}	Calibration coefficient
C_{My}	Mean bending moment coefficient
C_N	Mean normal force coefficient
C_P	Mean static pressure coefficient
C_P'	Static pressure RMS fluctuation coefficient
D	Cylinder diameter [m]
E_i	Load cell voltage, where i is the number of the load cell [V]
f	Vortex shedding frequency [Hz]
F_D	Mean drag force [N]
F_N	Mean normal force [N]
f_s	Sampling frequency [Hz]
H	Cylinder height [m]
H_δ	Boundary layer shape factor, δ^*/θ
Lu	Turbulence integral length scale [m]
M_y	Mean bending moment [N·m]
n	Number of samples
P	Mean surface static pressure [Pa]
P_0	Stagnation pressure [Pa]
P_∞	Freestream static pressure [Pa]
q_∞	Freestream dynamic pressure [Pa]
r	Cylinder radius [m]
Re	Reynolds number based on cylinder diameter, $U_\infty D/\nu_\infty$

Re_x	Reynolds number based on distance from the leading edge of the ground plane, $U_\infty(0.895 - x)/\nu_\infty$
Re_θ	Ground plane Reynolds number based on momentum thickness, $U_\infty\theta/\nu_\infty$
S	Sutherland temperature [K]
St	Strouhal number, fD/U_∞
T	Temperature [K]
T_0	Reference temperature [K]
TI	Longitudinal or streamwise turbulence intensity, u'/U_∞
U	Mean velocity [m/s]
u	Velocity component in the x-direction [m/s]
$u(t)$	Measurement of streamwise velocity at a particular time instant [m/s]
$U(z)$	Boundary layer mean velocity profile [m/s]
u'	RMS velocity fluctuation [m/s]
U_∞	Freestream velocity [m/s]
v	Velocity component in the y-direction [m/s]
w	Velocity component in the z-direction [m/s]
x	Streamwise coordinate [m]
y	Cross-stream coordinate [m]
z	Wall-normal coordinate [m]

Greek Symbols

δ	Boundary layer thickness [m]
δ^*	Displacement thickness [m]
ζ	Damping ratio
Θ	Cylinder angular position [°]
θ	Momentum thickness [m]
μ_0	Reference viscosity [kg/m·s]

μ_∞	Freestream dynamic viscosity [kg/m·s]
ν_∞	Freestream kinematic viscosity [m^2/s]
ρ_∞	Freestream density (kg/m^3)
τ	Time separation [s]
$\varphi(x)$	Error in a representative variable (x)

1 Introduction

1.1 Background

A cylinder is a fundamental shape that is used frequently in engineering design. Often, it is placed in a scenario where it is exposed to a cross-stream flow, and the cylinder may experience high wind loads or fluid forces. The cylinder is a fundamental example of a bluff (non-streamlined) body, associated with a large wake and a region of separated flow, which contribute to these large forces. Significant work has been undertaken in the past to come to a good understanding of the flow conditions around a cylinder and the associated forces that result from these flows. Past experiments have focused on two-dimensional (2-D), or "infinite", cylinders, where the cylinder length greatly exceeds its diameter, and the effects of the cylinder ends are not significant. Infinite cylinders offer a good representation of the behaviour at the center portion of a tall cylinder, and numerous review articles (including Coutanceau and Defaye (1991) and Williamson (1996)) and books (by Sumer and Fredsoe (1997) and Zdravkovich (1997)) have covered the associated flow patterns. For a wide range of Reynolds numbers, the wake region behind the cylinder is characterized by alternately shed vortices from the two sides of the cylinder that form a regular Karman vortex street pattern. The resulting fluctuations in pressure experienced by the cylinder can contribute to noise and vibration. The differences in pressure caused by the flow are a major contributor to the fluid forces experienced by the cylinder, and for most Reynolds numbers and engineering applications, the pressure contribution to the forces is stronger than the skin friction contribution. A strong understanding of the pressures and forces experienced by a cylinder will lead to better designs for future applications.

In many engineering applications involving the flow around a cylinder, the cylinder cannot be considered 2-D or infinite. Instead, the cylinders are three-dimensional (3-D) or "finite" (e.g. Okamoto and Sunabashiri (1992), Tanaka and Murata (1999), Sumner, Heseltine and Dansereau (2004), and Krajnović (2011)), and the flow pattern becomes more complex. For a surface-mounted finite-height cylinder, the junction between the cylinder and the surface (or ground plane) and the top of the cylinder (the tip or free end) both influence the flow field, the wake, and the forces. Recent studies of the flow around surface-mounted finite-height cylinders and square prisms have led to new models of the wake (e.g. Wang and Zhou (2009), Bourgeois, Sattari and Martinuzzi (2011), and Krajnović (2011)), but many questions still remain, especially concerning

the effect of the slenderness, or aspect ratio, of the finite cylinder. The research presented in this thesis is an attempt to generate information that will lead to an improved understanding of how the forces and pressure experienced by the finite cylinder are influenced by the aspect ratio and the flow conditions on the ground plane.

Finite cylinders in practice will typically have at least one connection to a ground plane, with the other end remaining free. Therefore, studies of finite cylinders tend to be based on a cantilever configuration, to allow for the effects of both end conditions to be analyzed. A schematic of the general flow setup for the cylinder investigated in this thesis research project can be seen in Figure 1.1.

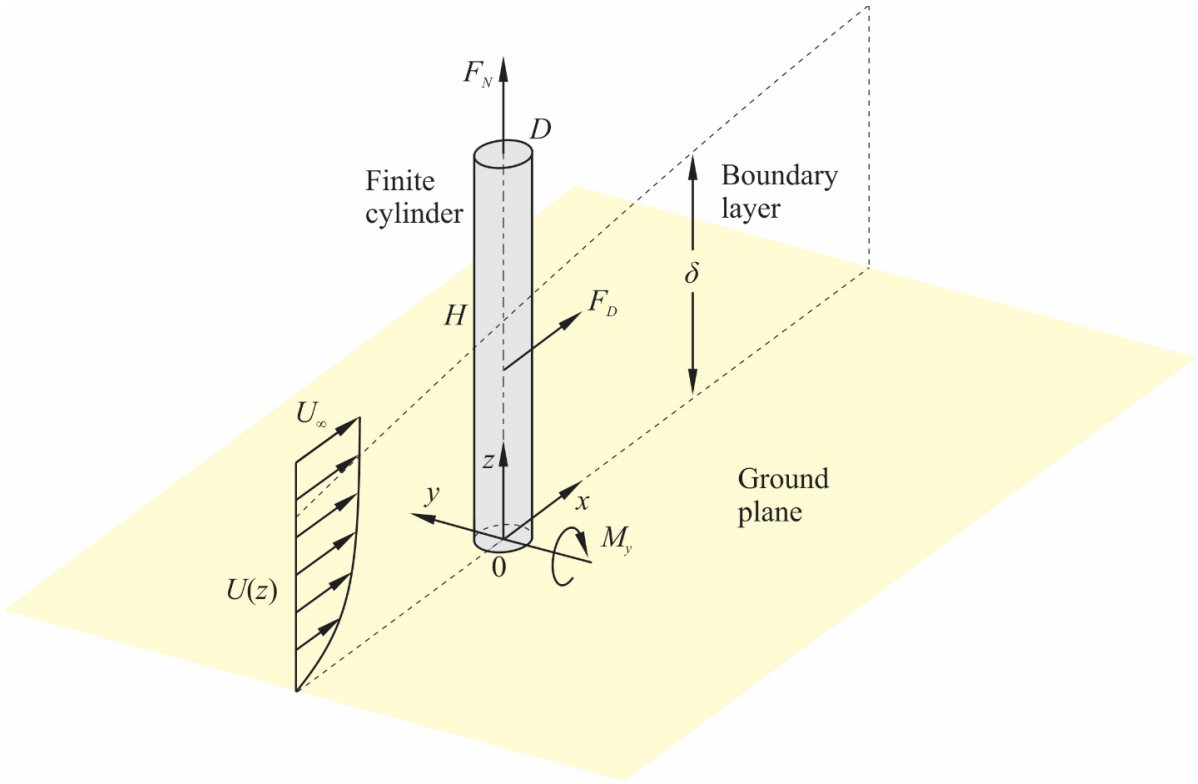

Figure 1.1: Schematic of the flow around a surface-mounted finite-height cylinder of diameter D and height H. The origin of the coordinate axis is at the center of the junction between the cylinder and ground plane. The coordinate directions x, y, and z are shown in the figure as orthogonal directions from the origin, where x is the streamwise direction, y is the transverse (or cross-stream) direction, and z is the vertical (or wall normal) direction. The freestream velocity, U_∞, gives rise to the boundary layer mean velocity profile, $U(z)$, and the boundary layer height, δ. The oncoming flow creates a mean drag force, F_D, a mean normal force, F_N, and a mean moment about the y-axis, M_y. Figure created by D. Sumner (used with permission).

The cylinder with diameter, D, and height, H, is immersed in a freestream flow velocity, U_∞. Flow characteristics often change with the Reynolds number, $\mathrm{Re} = U_\infty D/\nu_\infty$, where ν_∞ is the kinematic viscosity of the fluid. Pressures are represented by the non-dimensional pressure coefficient $C_P = (P - P_\infty)/(\frac{1}{2}\rho_\infty U_\infty^2)$, where P is the measured pressure, P_∞ is the freestream static pressure, and ρ_∞ is the fluid density. The denominator of the coefficient is the freestream dynamic pressure, q_∞. The mean drag and mean normal forces and the mean bending moment are similarly non-dimensionalized into their respective coefficients as the mean drag coefficient $C_D = 2F_D/(\rho_\infty U_\infty^2 HD)$, mean normal coefficient $C_N = 2F_N/(\rho_\infty U_\infty^2 \pi D^2/4)$, and the mean bending moment coefficient $C_{My} = 2M_y/(\rho_\infty U_\infty^2 H^2 D)$. The normal force and bending moment have not received much attention in the literature, and are defined here in a manner similar to the drag force. The mean normal force is non-dimensionalized by the freestream dynamic pressure and the area of the cylinder free end ($A = \pi D^2/4$). The mean bending moment is non-dimensionalized by the freestream dynamic pressure, the frontal area of the cylinder, and the cylinder height. The bending moment is defined positive in the clockwise direction, as shown in Figure 1.1. Vortex shedding frequencies are non-dimensionalized as the Strouhal number, $\mathrm{St} = fD/U_\infty$, where f is the vortex shedding frequency. The slenderness of the cylinder is represented by its aspect ratio, $\mathrm{AR} = H/D$. Measurements in x, y and z are non-dimensionalized by the cylinder diameter. This is also true for the boundary layer thickness, δ, which represents the location above the ground plane at which the streamwise velocity component is 99% of U_∞. The boundary layer thickness is mainly represented in dimensionless form as δ/D but δ/H is also used.

The flow around a finite cylinder is predominantly influenced by three parameters: the freestream Reynolds number, Re; the cylinder aspect ratio, AR; and the relative boundary layer thickness, δ/D. The Reynolds number is known to have a strong influence on the flow around 2-D cylinders (Coutanceau and Defaye 1991, Williamson 1996), but prior research has not looked extensively at how these effects translate to finite cylinders. Of these three parameters, the aspect ratio is the best understood, although gaps still remain in this area. Existing studies on finite cylinder forces and pressures tend to focus mainly on a single aspect ratio, or several low aspect ratios, where $\mathrm{AR} \leq 2$. This has led to a gap in the knowledge base, especially regarding how the free end pressures change at higher AR (Sumner 2013). Past research on finite cylinder

wakes has led to the discovery of a critical aspect ratio (Okamoto and Yagita 1973, Sumner, Heseltine and Dansereau 2004) where the flow pattern appears to change. However, due to the large increment between tested AR, the exact location of this critical AR has not been verified, and it is also sensitive to several flow parameters (such as δ/D). A lack of standard flow conditions in prior research has led to difficulties determining the effect of changes in individual flow parameters, especially the boundary layer thickness, δ/D or δ/H. It is expected that the boundary layer thickness has an influence on all the flow forces and pressures, including the critical aspect ratio, but is not frequently varied in a single experiment. A number of the fluid forces have received little attention in the literature as well, including the mean normal force that arises primarily from the free-end pressures (there is also a contribution from shear forces acting in the z-direction), and a mean bending moment that results primarily from the drag of the cantilevered cylinder (there is also a small contribution from the normal force and its point of action). Improving the knowledge of these quantities is likely to lead to better designs in future engineering applications.

1.2 Objectives

To come to an increased understanding of the flow around a finite cylinder, five objectives were set:

1. Develop an understanding of how the mean drag force, mean normal force, mean bending moment, vortex shedding, and free-end pressure distribution are influenced by the aspect ratio of the finite cylinder;
2. Determine how the boundary layer thickness influences the effects of aspect ratio, and which parameter is the dominant influencing parameter on the flow;
3. Define, measure and record the behaviour of the mean normal force;
4. Measure the mean bending moment at the base of the cylinder, and verify whether it is solely influenced by the drag force;
5. Enhance the understanding of the flow on the free-end surface by obtaining detailed pressure distributions.

1.3 Scope

This thesis work takes an experimental approach, using wind tunnel experiments, aimed at determining how the aspect ratio changes the flow around a surface-mounted finite-height cylinder. The main measures of these effects are the surface pressures that are caused by the flow field and the aerodynamic forces that result from them. On the cylinder free end, separation of the flow leads to a pressure distribution that is indicative of the flow above the free end. This research pays special attention to these pressures, focusing on obtaining pressure distributions for high AR, where there are few results reported in the literature (Sumner 2013). The mean pressures and pressure fluctuations are measured using high-frequency pressure transducers. The freestream flow also causes several forces to be developed, the most prominent of which is the mean drag force, which pushes the cylinder in the flow direction. Because of the cantilever connection of the cylinder, there is a mean bending moment developed by this drag force that tends to tip the cylinder over. Both the drag force and the resultant moment are measured with a force balance in these experiments. On the free end surface of the cylinder, the surface pressure coefficients are noted to be negative (from published data), creating a small force that tends to pull the cylinder vertically upwards and away from the ground plane. This normal force is also measured using the force balance, and the time-averaged surface pressures are measured using high-frequency pressure transducers. The vortex shedding frequencies behind the cylinder are measured using a hot-wire probe.

The important contribution of this work is to measure the influence of the aspect ratio, and 22 evenly spaced aspect ratios in the range of $0.5 \leq \mathrm{AR} \leq 11$ were used for all parameters to accomplish this. Each quantity was also measured while the cylinders were within two different boundary layers. Measurements that required a force balance were also completed with a second, smaller cylinder. By these methods, force measurements were completed for two thin ($\delta/D = 0.60$ and $\delta/D = 0.92$) and two thick ($\delta/D = 1.88$ and $\delta/D = 2.86$) relative boundary layer thicknesses. Pressure measurements were only completed for $\delta/D = 0.60$ and $\delta/D = 1.88$, while the measurements for $\delta/D = 0.92$ and $\delta/D = 2.86$ were only completed for five AR within the range of $1 \leq \mathrm{AR} \leq 9$. This range of AR and boundary layer thicknesses will aid in the understanding of how both the aspect ratio and the boundary layer influence the fluid forces and pressures, and hopefully determine which parameter is the strongest contributor.

A number of considerations were made to limit the scope of the experimental work. Forces were measured for a range of Reynolds number ($2.8x10^4 \leq Re \leq 1.0x10^5$), but pressure measurements were made for only $Re = 6.5x10^4$, and force measurements are reported for this same value. This Re was within the subcritical flow regime between $350 < Re < 2x10^5$, as suggested by Coutanceau and Defaye (1991). Within the subcritical regime, the cylinder flow is characterized by an attached laminar boundary layer before a separation point approximately 80° from the forward stagnation point. Further experiments should investigate the effects of moving outside the subcritical regime. The boundary layers used in this work were all relatively thick, and experiments with very thin boundary layers would help to confirm the amount of influence the boundary layer has on the fluid forces. The circumferential surface pressure on the cylinder was not measured for comparison with the drag force. It was not possible to use a small AR increment for the smaller-diameter cylinders, and so it was difficult to discern whether the exact location of the critical AR is maintained for different relative boundary layers.

The overall goal of this study is to develop an improved understanding of how the flow around a finite cylinder is affected by the aspect ratio of the cylinder. The small changes in the cylinder height between tests will give one of the most detailed looks (compared to published studies) at how various forces are influenced by the aspect ratio of the cylinder and the boundary layer in which it is immersed. The measurement of surface pressures will produce the most detailed representation to date of the free-end pressure distribution (Sumner 2013). It is the hope that the changes that are seen in the force and pressure measurements can ultimately be correlated with studies of the wake regions behind finite cylinders (e.g. Sumner, Heseltine and Dansereau (2004) and Krajnović (2011)) to determine how the aspect ratio affects flow structures, and how those structures in turn influence the forces and pressures on finite cylinders in practice.

1.4 Outline of the Thesis

This thesis is composed of five chapters plus appendices. Chapter 2 is a review of the literature that is available and the prior studies on finite cylinders. Chapter 3 contains a detailed account of the methods used in the experiments and the instrumentation used to complete the measurements. Chapter 4 outlines the results of the experiments, including discussions of the

force results and the free end pressure distributions. Chapter 5 contains important conclusions about the results and advice for future work. Appendix A contains the free end pressure distributions that were generated from published data, while Appendix B contains the free end pressure distributions generated by the current experiments. Appendix C contains profiles for the pressures along the flow-aligned centerline of the free end. Appendix D contains the contours of the free end pressure fluctuations. Appendix E contains the permissions obtained for figures used in the literature review portion of the thesis.

2 Literature Review

2.1 Introduction

The flow over cylinders is a topic of vital importance in engineering due to its relevance to real objects. Cylindrical objects are frequently used in buildings and transportation, commonly chosen for both aesthetic reasons and a comparatively low drag relative to square prisms of the same characteristic width. Cylinders can be found anywhere and in a wide range of applications, including chimney stacks (Holmes 2001), fluid storage tanks, and structural elements such as cables (Vandiver 1983) or solid columns. Often, these cylinders are exposed to cross-flow winds, which leads to high wind loading. The associated heat transfer is important to understand because cylinders are often used for cooling towers, pin fins, and heat transfer tubes or other heat transfer units, both large and small, such as electrical circuit board components (Tsutsui, Igarashi and Nakamura 2000). Smokestacks are usually cylindrical as well, and the flow around them can impact the dispersion of any potentially dangerous particulate being exhausted from the top. As a result of the shedding of vortices into the cylinder wake, cylinders are also susceptible to flow induced vibration, causing unwanted sound and structural instability (Porteous, Moreau and Doolan 2014).

The flow around an infinite cylinder has been well researched, and its main features are understood. Many studies are now focusing more on surface-mounted finite-height cylinders, as the ground plane and the cylinder end can have a significant effect on the flow structures that are seen. Finite cylinders in practice will generally have at least one connection to a ground plane, with the other end remaining free. Studies of finite cylinders therefore tend to be based on a cantilever configuration, to allow for the effects of both end conditions to be analyzed. A schematic of the general flow setup for the cantilever configuration investigated in this research was shown in Figure 1.1.

The flow past the free end of a finite cylinder has previously been investigated through a number of different approaches. Early studies tended to focus on surface oil visualization (e.g. Sparrow and Samie (1981), Roh and Park (2001)), where a thin film of oil is seeded with small particles, and air flow moves the oil film around the model. The appearance of the oil and particles at the end of the test can indicate how the flow interacts with the cylinder surface. Smoke flow visualization, where the flow is seeded with smoke particles, was also used in early

studies (e.g. Kawamura et al. (1984), Tsutsui, Igarashi and Nakamura (2000)) to see prominent structures in the flow. In later tests, this technique is expanded upon, and particle image velocimetry (PIV) was used (e.g. Pattenden, Turnock and Zhang (2005), Rostamy et al. (2012, 2013), Sumner et al. (2015)) to see instantaneous flow structures, capturing information in a two-dimensional flow plane and offering information on instantaneous velocities. Flow velocities and vortex shedding frequencies have also been obtained using hot wire anemometry (e.g. Sumner, Heseltine and Dansereau (2004), Adaramola et al. (2006)). Time-averaged flow pressures are measured in some studies with pressure probes, which can be located in the flow or on the surface of the cylinder itself (e.g. Hiwada et al. (1984), Sumner, Heseltine and Dansereau (2004), Tsutsui (2012)). Recently, numerical simulations, such as Reynolds averaged Navier-Stokes (RANS) simulations (e.g. Majumdar and Rodi (1989)), and large eddy simulations (LES) (e.g. Pattenden et al. (2006), Frederich et al. (2007), Krajnović (2011)), have been attempted to build a better understanding of the instantaneous flow structures.

A basic understanding of the main flow features for the flow past a finite cylinder and their associated formation mechanisms has been developed, as outlined in detail by Krajnović (2011), but many of the predominant theories on the interaction of wake structures and mechanisms are based on measurements of finite square prisms (e.g. Wang and Zhou (2009), Bourgeois, Sattari and Martinuzzi (2011), McClean and Sumner (2014), Sumner et al. (2017)). Square prisms have fixed separation points at their corners, which makes the wake behaviour more consistent, and much of the recent progress on the development of these downstream wake structures has been made using square prisms. Much of this newly developed theory may be applicable to the case of a finite cylinder, though the variable separation points and curved leading edge create complicated flow structures, and may require a unique explanation.

The flow around a finite cylinder is a developing field of study, and many questions still remain, but the main structures of the flow are generally known. As seen in Figure 2.1, the flow can be broken up into three main components: the Karman vortex structures, the horseshoe vortex system, and the tip flow (Roh and Park 2003). The Karman vortex structures are generated similarly to those seen for a two-dimensional (2-D) cylinder, but the end effects strongly influence these vortices. The horseshoe vortex forms upstream of the cylinder, near the ground plane, and is swept out to the sides of the cylinder. The flow over the free end is seen to

create a pair of counter rotating tip vortices and a downwash flow, directed towards the ground plane. These components will be described below in three sections: the wake system, ground plane structures, and tip flow structures, though the main focus will be on the tip flow, since this flow is most relevant to the thesis research.

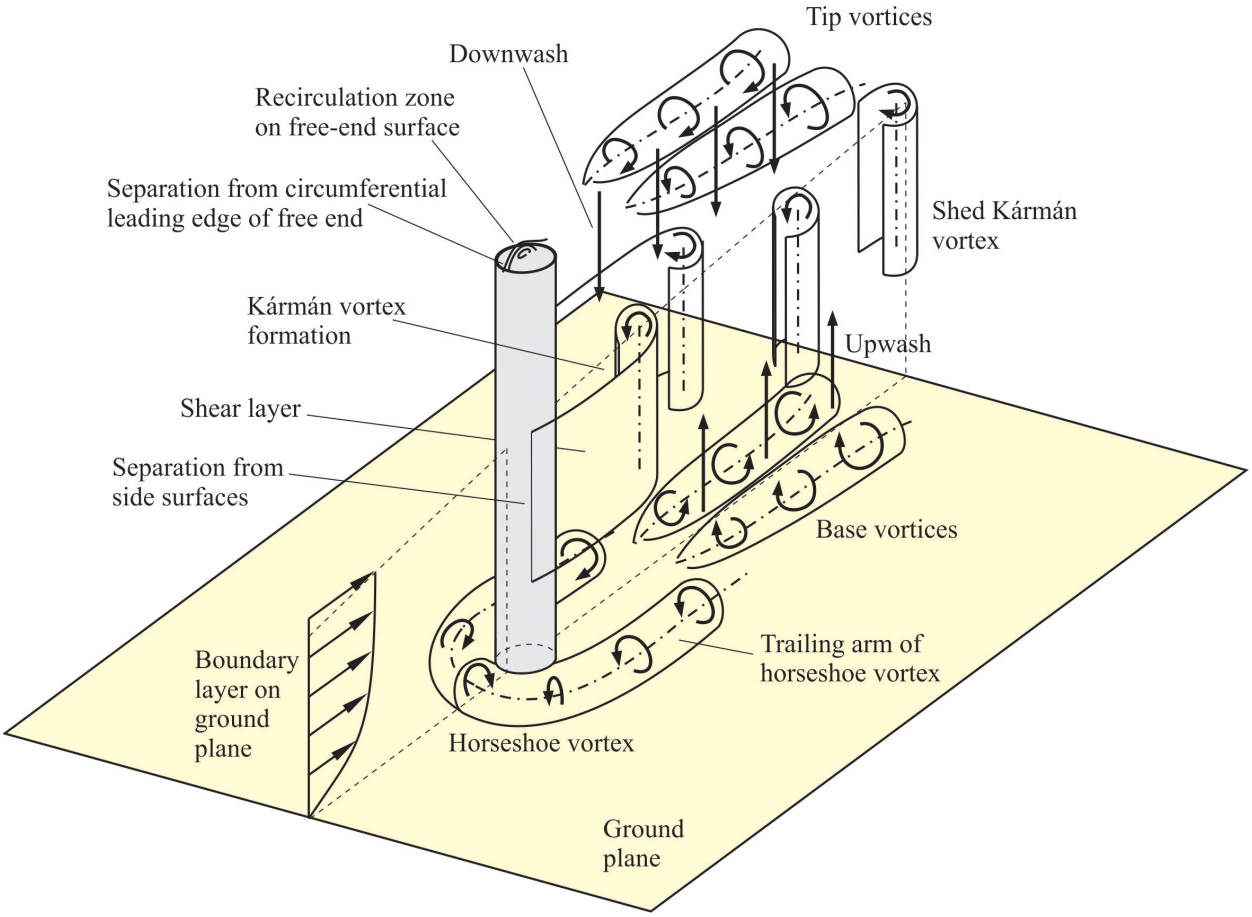

Figure 2.1: Schematic of the flow field behind a surface-mounted finite-height cylinder above the critical aspect ratio, based on the work of Sumner, Heseltine and Dansereau (2004). Figure created by D. Sumner (used with permission).

2.2 Wake System

The wake (a low pressure region behind the body) of a finite cylinder is different from an infinite cylinder due to both free-end and ground effects. While the center region of a sufficiently long finite cylinder may behave similarly to a 2-D cylinder, the effects of the free-end and the ground plane strongly influence the flow field for a wide range of AR. The wake structures include the trailing arms of the horseshoe vortex and base vortex structures close to the ground plane. In addition, at least two counter-rotating tip vortices are seen, and the upwash and downwash flows, seen in Figure 2.2 behind the cylinder, interfere with regular Karman vortex shedding. The upwash flow is an upward-directed velocity field originating from the ground plane, while the downwash is a downward-directed velocity field that begins near the cylinder free end. The downwash flow tends to increase the base pressure (the pressure on the cylinder surface measured 180° from the front stagnation point), which will decrease the drag for a finite cylinder from that of an infinite cylinder (Kawamura et al. 1984). Downwash flow is a significant issue for chimney stacks, as the downward-directed velocity field may carry potentially dangerous particulates into populous areas instead of higher into the atmosphere (Adaramola, Sumner and Bergstrom 2010).

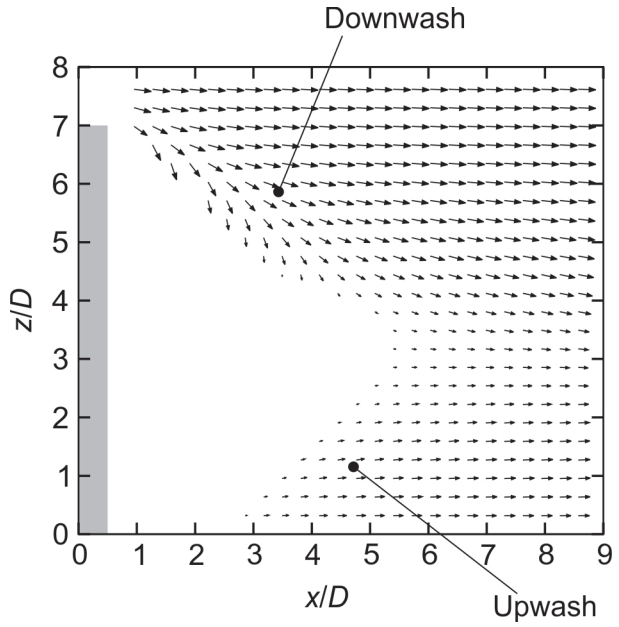

Figure 2.2: Mean flow field of the recirculation zone in the vertical symmetry plane for *u* and *w* in-plane velocity vector components. The upwash and downwash flows are clearly seen behind a cylinder of AR = 7. Flow direction is from left to right. Figure created by D. Sumner, based on Sumner, Heseltine and Dansereau (2004) (used with permission).

The main difference in the vortex shedding for a finite cylinder is the influence of the downwash flow from the tip of the cylinder. The downwash flow interferes with the formation of the Karman vortex structures, especially near the free end. The downwash extends below the free end and into the wake and suppresses vortex shedding until sufficiently far from the free end. Figure 2.2 shows the vector form of this downwash, and Figure 2.3 displays flow visualization.

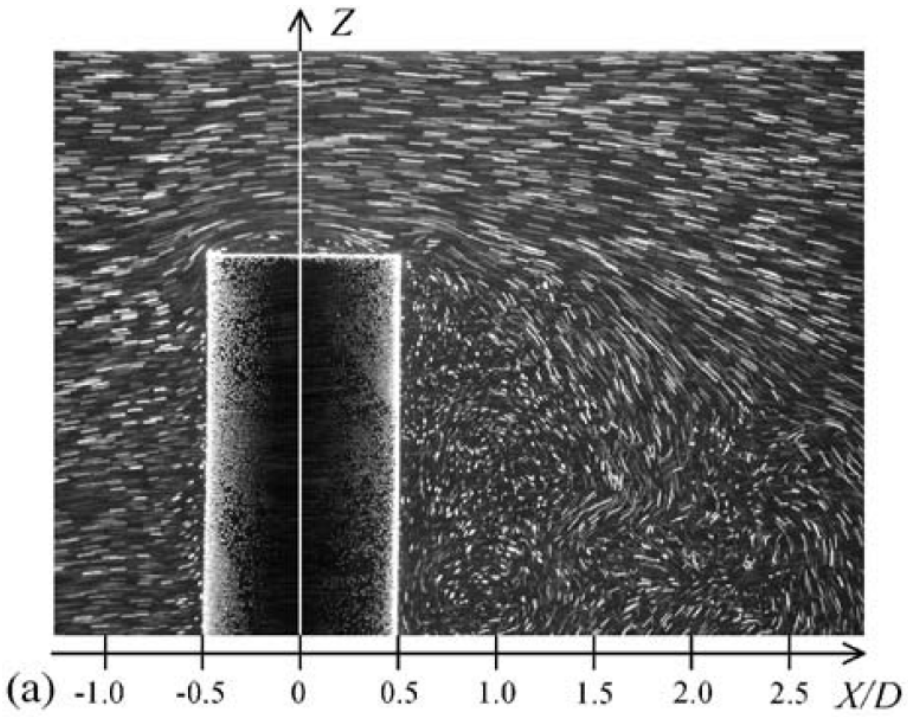

Figure 2.3: Flow visualization of the downwash (Re = $2x10^5$, D = 30 mm, AR = 6, δ/D = 0.93) from Park and Lee (2004). Flow direction is from left to right. Reprinted from Journal of Fluids and Structures, vol. 19, C.W. Park and S.J. Lee, Effects of free-end corner shape on flow structure around a finite cylinder, pp. 141-158, Copyright (2004), with permission from Elsevier.

Depending on the freestream flow conditions and the characteristics of the cylinder in question, vortex shedding may be entirely suppressed at low AR. The Strouhal number is generally reduced to a value of St ≈ 0.16 for a finite cylinder compared to an infinite cylinder in the subcritical regime (Sumner, Heseltine and Dansereau 2004). Okamoto and Yagita (1973) measured St for several different AR and found that the vortex shedding frequency decreases

strongly with a decreasing AR. In addition to this, there was no spectral peak for measurements within $z = 2D$ of the free end, and St increased at distances farther from the free end, reaching a constant value $4D$ from the free end. This indicates that the frequency is less affected farther from the free end. They found a similar result for the separation points on the cylinder sides, in that they moved forward as AR was decreased, and attributed this also to the effect of the free end flow. This earlier separation creates a wider wake and formation region, and a slower separation velocity, which could account for the lower Strouhal number (Kawamura et al. 1984). Near the tip, a small upward-directed flow is seen near the separation point (Kawamura et al. 1984). Also, close to the tip, some authors (e.g. Park and Lee (2004), Pattenden, Turnock and Zhang (2005)) have reported finding a smaller Strouhal number, of the order St ≈ 0.07-0.09, which they attribute to trailing or tip vortices.

Okamoto and Sunabashiri (1992) found that the flow pattern behind a finite cylinder changed drastically at AR = 4. They measured the length of the recirculation region as well, determining its maximum length was when AR = 4. At AR = 7, the recirculation length decreases, as downwash flow is confined to the tip region and does not extend all the way to the ground plane. Okamoto and Sunabashiri (1992) also showed that the vortex axes of the Karman vortex street are bent downstream by the downwash. Familiar Karman vortex shedding is suppressed for AR < 4. This value is referred to as a critical aspect ratio, though its exact value is not agreed upon, and may lie anywhere between AR = 3 and AR = 7 depending on flow conditions such as δ/D or δ/H. For these low AR, the downwash dominates the wake, and antisymmetric Karman vortex shedding is replaced with symmetric vortex shedding, called an "arch vortex" (Pattenden, Turnock and Zhang 2005). The downwash is likely to assist in the formation of arch vortices, as the downwash flow would tend to induce a vorticity in the recirculation region that matches that of the Karman axes when bent towards each other. It may also contribute to the bending of those axes. The arch vortex, seen in Figure 2.4, has two legs that extend all the way to the ground, as confirmed by Okamoto and Sunabashiri (1992). Sumner, Heseltine and Dansereau (2004) showed that these arch vortex axes were not vertical, but were inclined slightly in the flow direction, up to an angle of 30 degrees. Krajnović (2011) produced results from a large eddy simulation (LES), shown in Figure 2.5, that agreed with this, and generated a detailed picture of the top of an arch vortex, though the cylinder in this study was of AR = 6, which is expected to be above the critical aspect ratio. This inclination is due to

the downwash being much stronger near the top of the cylinder, while the middle part of the wake is influenced by the Karman vortices and freestream flow. Sumner et al. (2017) investigated this downstream flow region with PIV, seeing a similar arch vortex and also evidence for an additional cross-stream vortex forming behind the cylinder, near the ground plane.

The lower part of the wake, near the ground plane, is inhabited by two main vortex pairs, and a corresponding upwash flow. The first vortex pair represents the ends of the upstream horseshoe vortex as they are pushed by the freestream and curl around the cylinder sides (see Figure 2.1). This counter-rotating pair tends to spin such that the top curls in towards the cylinder. Within this pair, there appears to be a second set of vortices, rotating in the opposite direction (Tanaka and Murata 1999), which are termed the base vortices, but exist only above the critical aspect ratio, AR = 3 (Sumner, Heseltine and Dansereau 2004), and above a sufficiently high boundary layer thickness (Wang et al. 2006). These base vortices (see Figure 2.1) rotate away from the cylinder and may have a strong influence on the upwash flow from the ground plane. These vortex structures are described in more detail in Section 2.3.

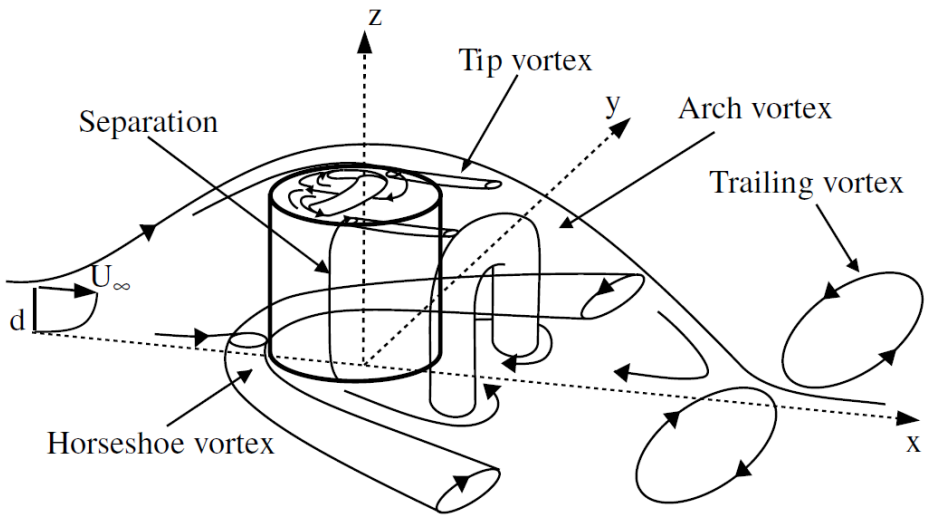

Figure 2.4: Schematic of the flow around a short cylinder from Pattenden, Turnock and Zhang (2005). Reprinted from Experiments in Fluids, Measurements of the flow over a low-aspect-ratio cylinder mounted on a ground plane, vol. 39, 2005, R.J. Pattenden, S.R.Turnock and X. Zhang, pp. 10-21, with permission of Springer.

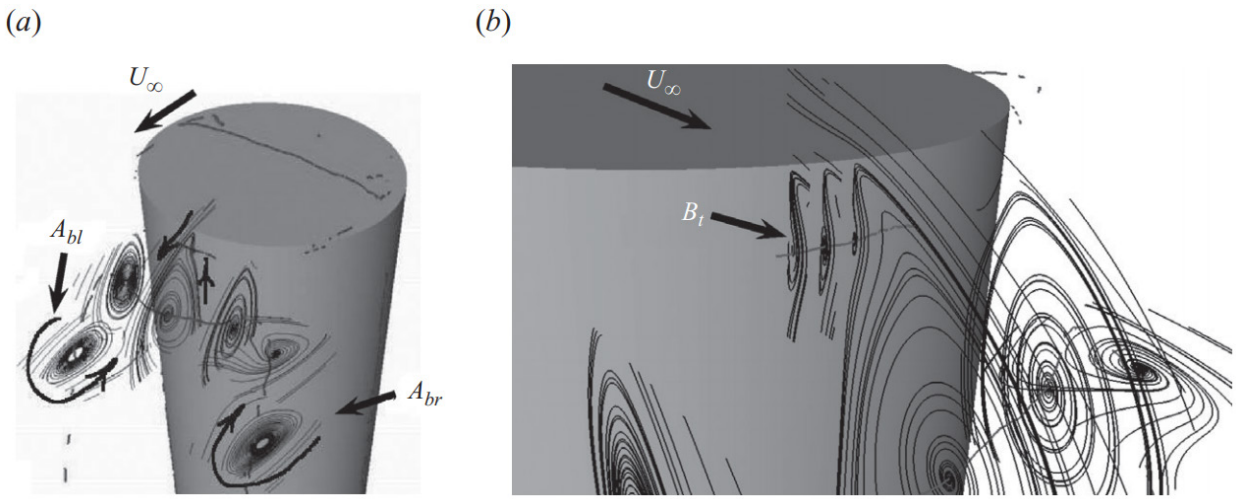

Figure 2.5: Streamlines showing the top of the arch vortex and the induced vortex from LES for AR = 6 from Krajnović (2011). Reprinted from S. Krajnović, Flow around a tall finite cylinder explored by large eddy simulation, The Journal of Fluid Mechanics, vol. 676, pp. 294-317, 2011, reproduced with permission from Cambridge University Press.

The tip vortex structures that are seen in Figure 2.1 and Figure 2.4 with streamwise axes will be described in more detail in Section 2.4. The tip vortices may be responsible for the downwash, as their sense of rotation would act to pull fluid into a downward-directed velocity field at the center of the wake. However, there is not enough information to confirm this, as the tip vortex formation mechanism is not well understood. The trailing vortices in the far wake of Figure 2.4 are not well described in the literature, but they do have the same sense of rotation as the tip vortices. It is possible that these two structures are the same, and the tip vortices persist downstream but are influenced by the downwash flow, as suggested by the work of Sumner, Heseltine and Dansereau (2004), shown in Figure 2.6. The tip vortices are distinct from the base vortices, having the opposite sense of rotation. Bourgeois, Sattari and Martinuzzi (2011) categorized the streamwise vorticity distribution as a quadrupole type system (with the tip and base vortices representing four streamwise vortical structures with alternating sense of rotation) above the critical aspect ratio, and a dipole type (where the two tip vortices represent two structures with alternating sense of vorticity) below the critical aspect ratio. The images from Sumner, Heseltine and Dansereau (2004), show these two configurations, with the quadrupole type being represented in Figure 2.6 (a,b, and c), and the dipole type being represented in Figure 2.6 (d).

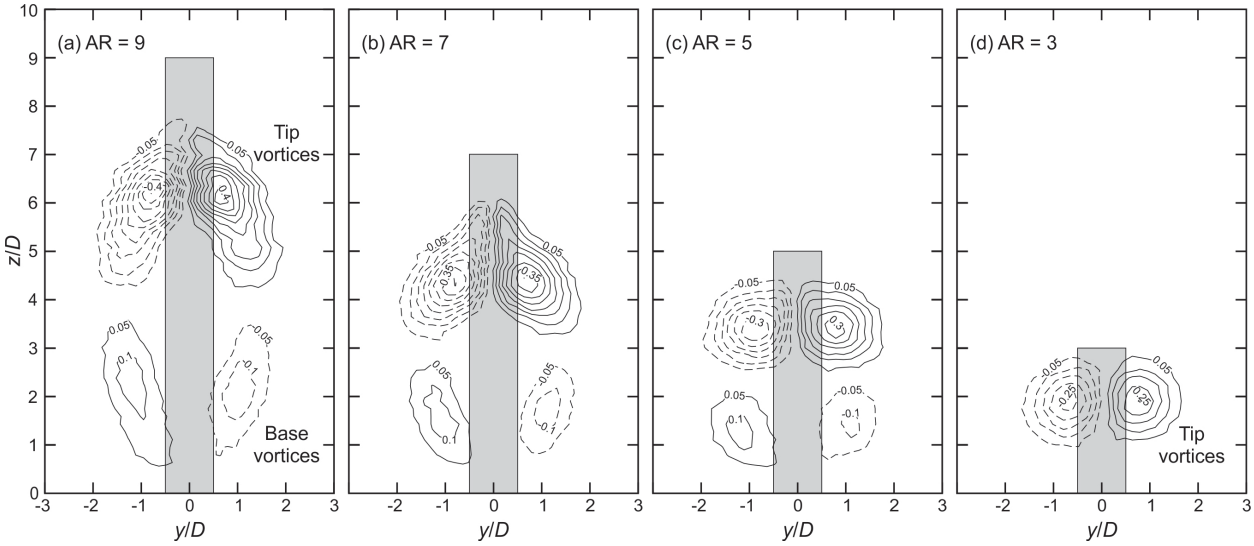

Figure 2.6: Time-averaged vorticity field in the wake of finite cylinders of varying aspect ratio, with a) AR= 9, b) AR = 7, c) AR = 5, d) AR = 3. Circulation is shown in the *y-z* plane, at *x/D* = 6. Solid lines represent CCW vorticity, dashed lines represent CW vorticity, clearly showing the tip and base vortices. Figure created by D. Sumner, based on Sumner, Heseltine and Dansereau (2004) (used with permission).

Due to the fixed separation points offered by square prisms, the defining flow features for finite cylinders have mainly been extrapolated from studies using square prisms. The work of Wang and Zhou (2009) and Bourgeois, Sattari and Martinuzzi (2011) have attempted to offer explanations for the shape of the wake. Wang and Zhou (2009) hypothesized a single arch vortex extending over the prism with curved legs, such that a cross-stream planar cut would create the illusion of tip and base vortex structures, which were seen clearly in Sumner, Heseltine and Dansereau (2004). Bourgeois, Sattari and Martinuzzi (2011) offered a half-loop explanation, where an arch vortex sheds one leg at a time, and the shed vortex axis bends down to stay connected to its partner. As this review is about the current state of literature on finite cylinders, the consequences of these models will not be detailed here. The flow around a cylinder is more complex than that of a finite square prism, as the variable separation points and curved leading edge lead to complicated interactions between the flow structures, and it is unknown whether these same models can be applied to finite cylinders. The current model suggests an arch vortex below the trailing edge of the free end for low AR, as seen in the work of Pattenden, Turnock and Zhang (2005) in Figure 2.4, and supported by the work of Krajnović (2011) and Sumner et al. (2017). This does little to fully explain the interaction between the free end flow and the

vortex shedding, and may not describe the flow at higher AR. More research must be done to characterize both square prism and cylinder flows, as they are both very common in engineering applications.

2.3 Ground Plane Flow Structures

One of the main ground plane structures of the finite cylinder flow field is the horseshoe vortex system. This vortex occurs upstream of the cylinder at its connection to the ground plane. The primary vortex here is caused by the cylinder creating an adverse pressure gradient in the fluid in front of it, pushing back on the incoming fluid (Baker 1980). This adverse pressure gradient aids in causing the local separation of the boundary layer from the ground plane. The separated flow then rolls up, creating the primary horseshoe vortex. This vortex forms around the cylinder and the ends are pushed downstream by the oncoming fluid, forming a horseshoe-shaped axis. The ends of this axis are often seen in velocity measurements normal to the flow, and can be recognized as ground plane vortices where the sense of rotation is to curl towards the cylinder. Under the primary vortex, the reversing flow separates once more, creating a secondary vortex, which influences a second primary vortex behind the first, as seen in Figure 2.7. The naming convention of Baker, seen in Figure 2.7, will be used in the thesis.

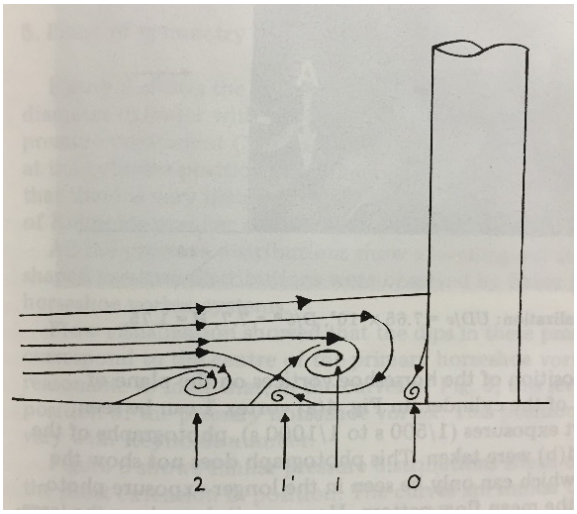

Figure 2.7: Schematic visualization of the horseshoe vortex (Baker 1980). Flow is from left to right. Vortex l is the primary horseshoe vortex, and Vortex l' is its wall image, Vortex O is the image on the cylinder wall, and Vortex 2 is the secondary horseshoe vortex. Reprinted from Journal of Wind Engineering and Industrial Aerodynamics, vol. 6, C.J. Baker, The turbulent horseshoe vortex, pp. 9-23, Copyright (1980), with permission from Elsevier.

These vortices are expected to continue to influence smaller vortices until they are no longer visible with flow visualization techniques, and Baker (1980) suggested at least six vortices were seen, three primary and three secondary vortices, a number confirmed also by Chen et al. (2012) and Pattenden, Turnock and Zhang (2005). Krajnović (2011) was not able to confirm the number of vortices due to the mesh size, but was able to note that the vortex image on the cylinder wall, Vortex O, persists only until the separation point. The size of these vortices does not appear to depend on Re, but the location of the vortices will move closer to the cylinder with lower AR when AR < 1.5, and when the boundary layer thins (Baker 1980). The horseshoe vortex has been confirmed to exist as low as AR = 0.35 (Tsutsui, Igarashi and Nakamura 2000). The size and strength of the horseshoe vortex scales with both δ/D and the "bluffness" of the structure.

Baker (1979) investigated the horseshoe vortex in a laminar boundary layer, and found that it tended to oscillate in two distinct modes in this flow regime. In the first, a regular oscillatory mode, the primary horseshoe vortex is seen to oscillate upstream and downstream. The mechanism for this is described by Baker (1979). The primary vortex, Vortex 1, moves upstream, and becomes isolated from Vortex 2 as the connection is cut off. When Vortex 1 moves forward, so too does its induced vortex on the ground plane, Vortex 1'. Because Vortex 1' tends to pull Vortex 2 towards the ground, Vortex 2 rises when Vortex 1 moves upstream. As Vortex 1 moves closer to the cylinder, it becomes influenced more by its wall image, Vortex O, which pushes it lower to the ground plane. Here, it becomes more influenced by its ground image, which pushes it back into Vortex 2. This oscillatory motion only occurs in the laminar regime. At higher flow speeds, the horseshoe vortex is unstable and shows up as a mean flow structure (Baker 1980). This instability was also seen by Krajnović (2011) and Pattenden, Turnock and Zhang (2005). However, their instantaneous results showed that the primary horseshoe vortex will frequently decay and Vortex 2 will move upstream to replace it.

In the turbulent regime, investigated by Baker (1980), only four predominant vortices are seen, Vortex 1, Vortex 1', Vortex 2, and Vortex O, which is formed as the primary vortex pulls on the fluid flowing down the cylinder sides. The pressure minimum on the ground plane exists under Vortex 1. The pressure distributions could not be seen to vary with Re, though a

decreased boundary layer thickness will increase the pressure. This negative pressure could be a strong driving force for scour on erodible beds.

The horseshoe vortex system is clearly identified in many studies, but is not the only vortex structure close to the ground plane. The existence of a pair of streamwise, counter-rotating base vortices has also been reported for aspect ratios above the critical aspect ratio (Sumner, Heseltine and Dansereau 2004). These base vortices are differentiated from the horseshoe vortices by their opposite rotation, making them also counter-rotating to the tip vortex structures, which are discussed in Section 2.4. The base vortices are generally seen closer to the cylinder and higher above the ground plane compared to the horseshoe vortex. Sumner, Heseltine and Dansereau (2004) theorized that the base vortex structures may be Karman vortex axes that are bent, owing to the sense of rotation and the fact that both structures seem to disappear below AR = 3. This disappearance is generally attributed to the downwash flow, which Krajnović (2011) says is helped by the horseshoe vortex creating its own weak downwash in the same region at low AR. Krajnović (2011) identified the base vortices in his large eddy simulation, but did not offer an explanation for how they are formed. It can be seen that the base vortices have the same sense of rotation as the image of the horseshoe vortex that is induced on the cylinder surface (Vortex O). There is a possibility that these two structures may interact or in fact be the same structure, though this has not been tested, and Krajnović (2011) asserted that the wall image vortex disappears at the separation point. An upwash flow from the ground plane induced by the counter-rotating base vortices is generally seen as well (Krajnović 2011, Sumner, Heseltine and Dansereau 2004). Figure 2.8 displays flow details from the work of Krajnović (2011).

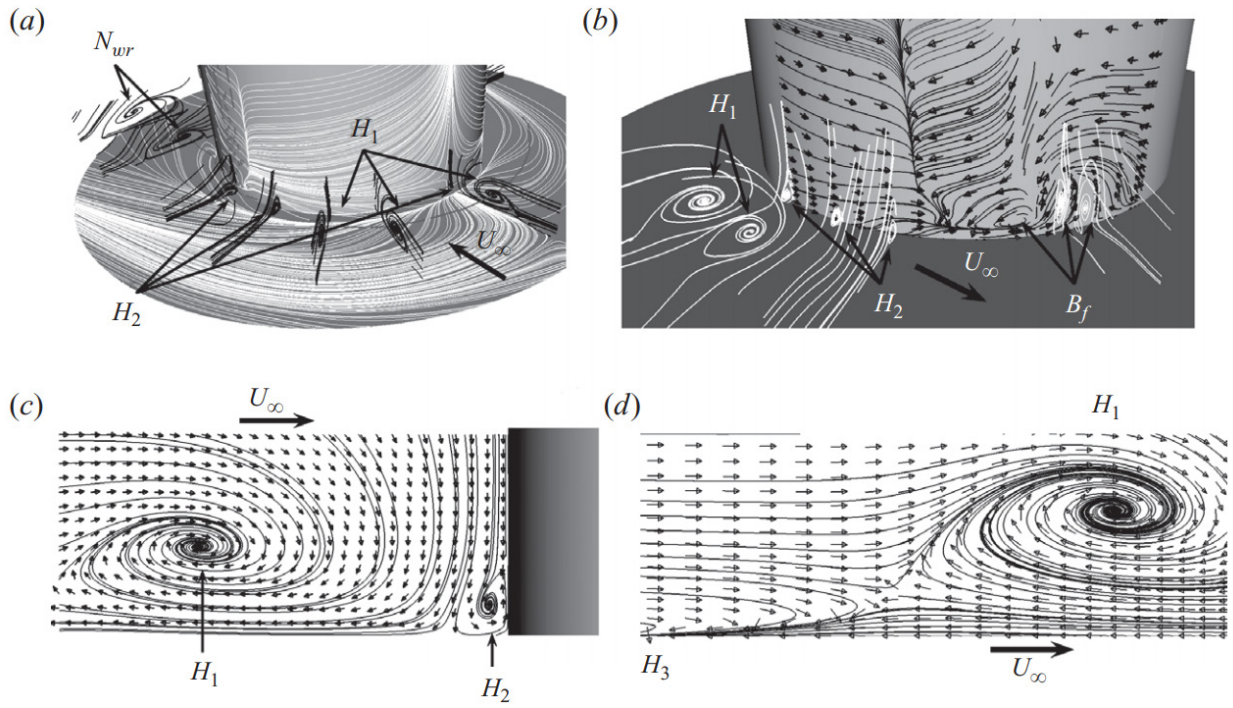

Figure 2.8: Visualization of the horseshoe vortex from large eddy simulations for a) the front, b) the rear, c) front *x-z* plane, and d) zoomed front *x-z* plane for a cylinder of AR = 6 and Re = $2x10^4$ from Krajnović (2011). Reprinted from S. Krajnović, Flow around a tall finite cylinder explored by large eddy simulation, The Journal of Fluid Mechanics, vol. 676, pp. 294-317, 2011, reproduced with permission from Cambridge University Press.

Pattenden, Turnock and Zhang (2005) performed surface flow visualization on the ground plane of a cylinder with AR = 1, and found an additional vortex that forms in the back corner of the trailing half of the cylinder. This vortex has an opposite sense of rotation to the primary horseshoe vortex. Krajnović (2011) found this vortex as well, noting that it has the same sense of rotation as the secondary vortex induced on the side of the cylinder. This vortex can be seen as vortex B_f in Figure 2.8 (b). Krajnović implies that the additional vortex is formed by the influence of the recirculating region. This small vortex does not persist long, as it is overcome by the backflow and the base vortex, although it has the same sense of rotation as the base vortex. Behind the cylinder, the downwash flow from the free end seems to reattach on the cylinder and forms a vortex that is essentially a mirror of the horseshoe vortex on the back half of the cylinder. This structure was seen in both computational work by Krajnović (2011) and PIV by Rostamy et al. (2012), and affects the flow downstream of the region, aiding in breaking up vortex B_f and other structures. Recent work by Rinoshika, Rinoshika, and Fujimoto (2017)

may have found this vortex also existing for an AR = 1 cylinder, indicating that it may exist for smaller AR, though it appears to be caused by different factors. This region of flow is complex and its effects on the cylinder are unknown, prompting a need for further study.

The horseshoe vortex system is the dominant structure at the junction between the cylinder and the ground plane. Because almost all cylinders must have a connection to a type of ground plane, horseshoe vortices are seen in almost all real cylinder flows. The associated negative ground pressure and upwash flows become a concern for erodible beds at risk of scour or places such as the joint of an airplane wing to the fuselage. Because the near-wall vorticity can influence heat transfer and mass transfer as well, generating a good understanding of the complex flow near the ground plane is necessary.

2.4 Free End Flow Structures

Flow over the free end of a finite cylinder is complex and requires more research before it is fully understood. The free end flow structures can have a significant impact on all other components of the flow, so they are of real importance in characterizing the complete flow over a finite cylinder. Features such as the tip vortices (in the upper wake) and mushroom vortex (above the free end) may influence the development of other structures like the downwash flow, which interferes with wake structures, vortex shedding, and fluid forces. The key features of the free end flow field are flow separation from the leading edge, the recirculation zone, and the mushroom vortex. There are several secondary structures as well, including tip vortices, a secondary recirculation zone, and saddle points, among others. These will be described in the current section.

Measurements of surface properties on the free end must be done with a type of instrumented cylinder, as few probe techniques can get close enough to the cylinder without risk of interference. Because of the difficulty of accurately measuring these components before advanced computer software, relatively little was done to study the free end until the early 1980s. One early study was completed by Kawamura et al. (1984), who used smoke flow visualization at a subcritical Re to view the flow over the free end. They observed an arc in the flow, showing separation from the leading edge and reattachment on the downstream half of the free end, for cylinders of both AR = 1 and AR = 8. Reattachment was not seen for AR = 4, which they

attributed to an upwash flow on the sides of the cylinder near the free end. The result at AR = 4 was not seen in any other sources consulted (and may be due to an error in their test conditions), but it may be evidence that the tip flow is sensitive to many parameters and could be unstable. The smoke flow also showed evidence of the downwash flow coming from the free end, along with the cross-stream vortex that it may induce directly below the free end.

Kawamura et al. (1984) theorized that flow coming from the free end and flow from the sides would combine to form a "trailing vortex" with a streamwise axis that angles down due to the downwash. They conducted surface oil flow visualization as well, revealing a pair of vortical patterns on the free end surface. These "eye-like spots" (Roh and Park 2001) are the site of minimum surface pressure, and are less prominent at AR = 1. Within the recirculation zone, the flow moves upstream near the free end surface, forming a "mushroom vortex" (Kawamura et al. 1984). This information was combined with the information of the ground plane structures and the wake measurements by Holscher and Niemann (1996) into a preliminary idea of the mean flow around a cylinder, seen in Figure 2.9. Because most tests at this time occurred on low-AR cylinders, this schematic is applicable mainly to cylinders below the critical aspect ratio. Holscher and Niemann represented a two-vortex structure on the free end, indicating the existence of a smaller secondary separation bubble near the leading edge.

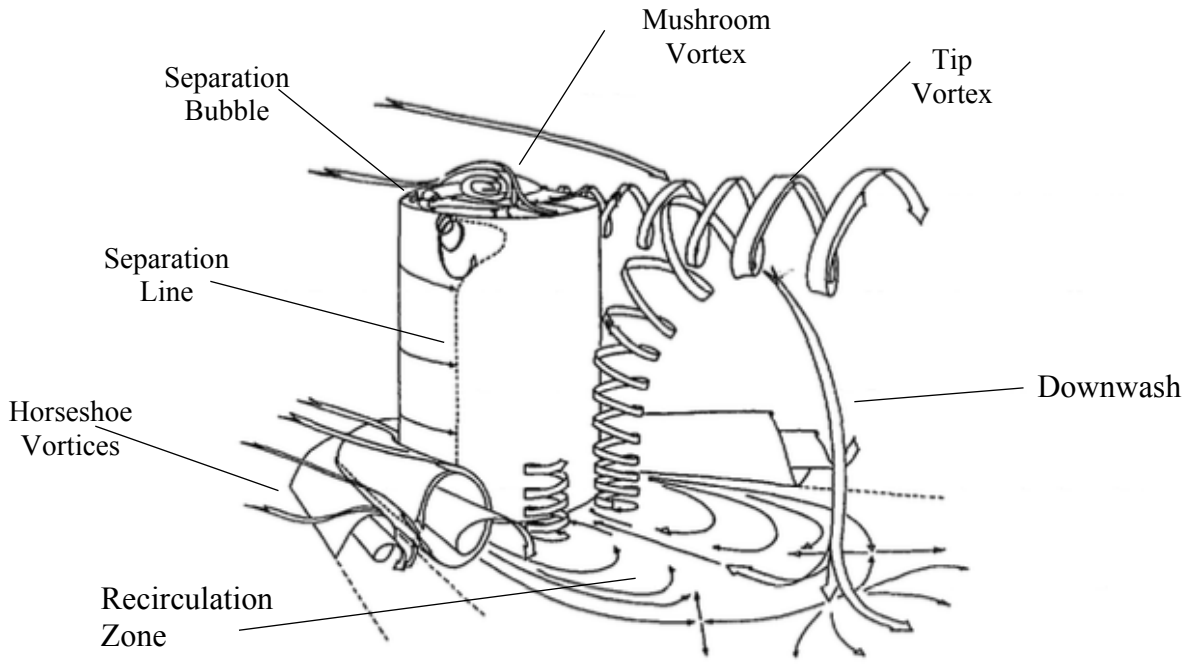

Figure 2.9: Schematic of the flow around a finite cylinder from Holscher and Niemann (1996). Flow is from left to right. Reprinted from Journal of Wind Engineering and Industrial Aerodynamics, vol. 65, N. Hölscher, H-J Niemann, Turbulence and separation induced pressure fluctuations on a finite circular cylinder — application of a linear unsteady strip theory, pp. 335-346, Copyright (1996), with permission from Elsevier.

This model shows the recirculating region on the free end, along with tip vortices and horseshoe vortices, while showing the Karman vortex being entrained into the tip vortex. It does not show the base vortex structures (which are not always seen) or the arch vortex, and has less detail on the free end, due to the available data at the time. The separation line on the cylinder illustrates the upwash described in Kawamura et al. (1984), which delays the separation near the free end. Tsutsui, Igarashi and Nakamura (2000) investigated the free end further, and found that the heat transfer and pressure contours were both related to the surface film visualization, with the reattachment region (downstream of the recirculation zone) corresponding to maximum pressure and maximum heat transfer. The minima for these quantities were found beneath the recirculation region. Roh and Park (2001) attempted to clarify the flow using oil-film measurements. Because the right "eye", when viewed from above, rotates clockwise, and the left eye rotates counterclockwise, a saddle must exist between them, and this point could be seen in

their oil film visualization as well. The reattachment region seems to generally take an arc shape (Kawamura et al. (1984), Tsutsui, Igarashi and Nakamura (2000)), but Roh and Park (2001) viewed three nodes on the reattachment line, two attachment nodal points, marked B and B' in Figure 2.10, and a separation saddle point, marked A in Figure 2.10. The flow appears to reattach at B and B', leaking out to meet at the saddle point A, at which point it again separates from the cylinder. This may correspond with the site of maximum pressure that Tsutsui, Igarashi and Nakamura (2000) found to lie on the reattachment line.

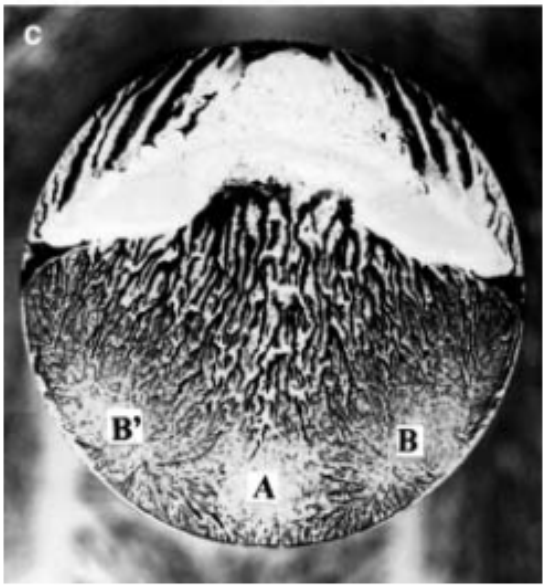

Figure 2.10: Surface oil flow visualization on the free end from Roh and Park (2001). B' and B represent nodal reattachment points, while A is a separation saddle point. Flow is from top to bottom. Reprinted from Heat and Mass Transfer, Surface flow pattern and local mass transfer on the free-end surface of a finite circular cylinder, vol. 38, 2001, S.C. Roh and S.O. Park, pp. 1-5, with permission of Springer.

Roh and Park (2003) revisited these data, combined with their own laser light sheet tests, in an attempt to capture the tip vortices. The results showed vortices evolving for the entire length of the top of the cylinder. Two sets of counter-rotating vortices were visualized: a pair of "tornado-like vortices" originating from the foci and a pair of "side-tip vortices" (Roh and Park 2003), as seen in Figure 2.11. These results appear to be consistent with their laser light sheet visualization, but do not agree with previous, or future, studies that show reattachment on the cylinder.

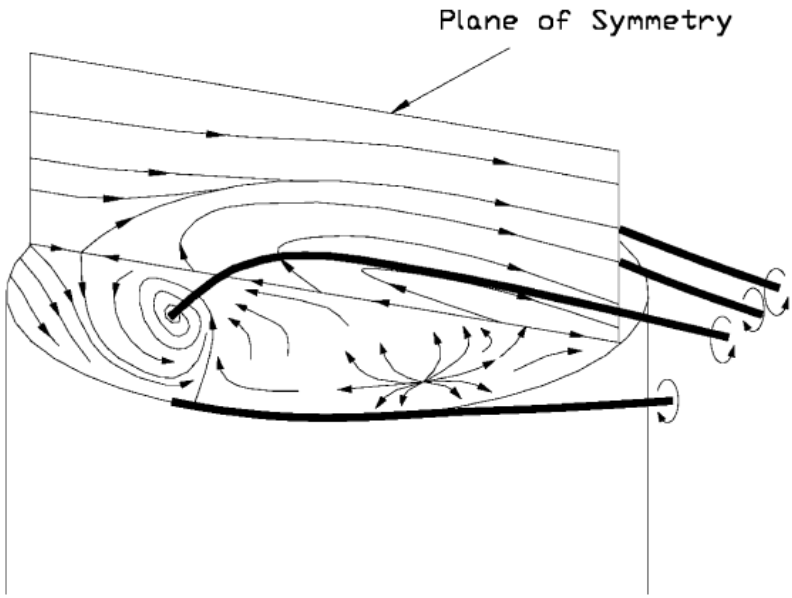

Figure 2.11: Predicted flow from the cylinder free end from Roh and Park (2003). Flow is from left to right. Reprinted from Experiments in Fluids, Vortical flow over the free end surface of a finite circular cylinder mounted on a flat plate, vol. 34, 2003, S.C. Roh and S.O. Park, pp. 63-67, with permission of Springer.

Research on free-end flow began to accelerate when PIV and numerical simulations became available, and higher resolution was possible. Pattenden, Turnock and Zhang (2005) used PIV to investigate the free end flow for AR = 1, and Re = 2 x 10^5. They did not find the same flow structures as Roh and Park (2003), concluding instead that the flow reattaches at the saddle point, located at x/D = 0.17 downstream of the center of the cylinder (corresponding to x = 0). This disproves the "tornado-like vortices" from Roh and Park (2003). Pattenden, Turnock and Zhang (2005) asserted that the two eye structures were foci of a cross-stream vortex axis formed by the recirculating region, in agreement with Kawamura et al. (1984) and the proposed mushroom vortex. Between these eyes, the saddle point was seen to be a separation point, where the reversing flow from the recirculation region separates from the surface and forms its own vortex as the reversed flow turns towards the sides. The tip vortices seen by Roh and Park (2003) were also seen by Sumner, Heseltine and Dansereau (2004) and Pattenden, Turnock and Zhang (2005), and these structures, of which the left side vortex has a negative (clockwise) rotation and the right vortex has positive (counter-clockwise) rotation, were seen to carry far downstream, angling slightly downwards immediately after leaving the cylinder. This downward

movement is attributed to the influence of the downwash flow. The mechanism for the formation of these tip vortices was suggested by Park and Lee (2004), stating that the tip vortex is caused by the interaction between the entrained ambient fluids and the downwash flow. An alternate explanation was offered by Pattenden, Turnock and Zhang (2005), that the shear layers at the sides and over the top interact to form the vortices. This is similar to the explanation of Kawamura et al. (1984), who asserted that the tip vortices were formed by the interaction of the downwash flow and the small upwash that was seen from the sides of the cylinder near the free end.

Hain, Kähler and Michaelis (2008) performed tomographic and time-resolved PIV in an attempt to resolve the flow over the free end. The instantaneous measurements revealed high unsteadiness in the flow field. Tip vortex structures were seen in the mean flow, but were not well-defined during instantaneous measurements. In fact, they were accompanied by weak counter-rotating vortex structures that existed between the two main tip vortices, seen in Figure 2.12, which may support the hypothesis of Roh and Park (2003). However, the predominant tip vortices were accompanied by many other small vortices, and these inner structures may be related to the smaller vortices. Hain, Kähler, and Michaelis (2008) showed PIV in the *x*-*z* plane as well, seen in Figure 2.13, confirming the appearance of the mushroom vortex, and representing the high gradient in the shear layer bordering the separated flow.

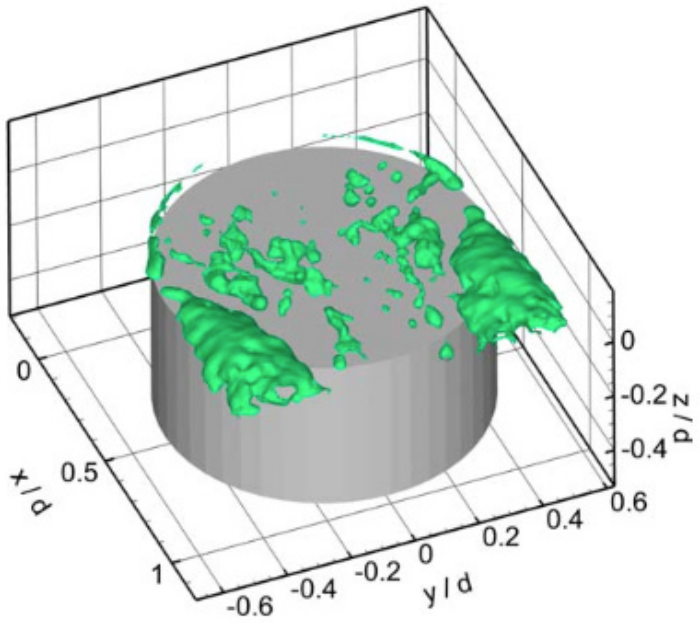

Figure 2.12: Vortex patterns off the free end using PIV measurements from Hain, Kähler and Michaelis (2008). Flow is from top left to bottom right. In this figure, d is the cylinder diameter. Reprinted from Experiments in Fluids, Tomographic and time resolved PIV measurements on a finite cylinder mounted on a flat plate. vol. 45, 2008, R. Hain, C.J. Kähler and D. Michaelis, pp. 715-724, with permission of Springer.

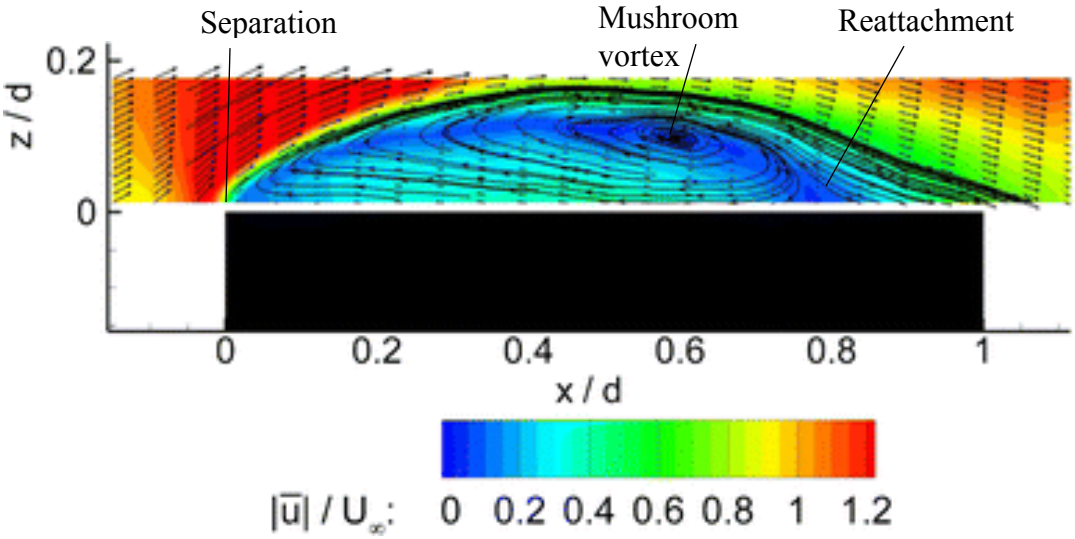

Figure 2.13: Velocity contour and vectors in the *x*-*z* plane above the free-end from Hain, Kähler and Michaelis (2008). Note that the origin of the coordinate system is at the leading edge of the cylinder in this case. Flow is from left to right. In this figure, d is the cylinder diameter and $|\bar{u}|$ is the mean flow velocity. Reprinted from Experiments in Fluids, Tomographic and time resolved PIV measurements on a finite cylinder mounted on a flat plate. vol. 45, 2008, R. Hain, C.J. Kähler and D. Michaelis, pp. 715-724, with permission of Springer.

The reattachment line is further back than that found by Pattenden, Turnock and Zhang (2005), who used AR = 1, while Hain, Kähler, and Michaelis (2008) used AR = 2.167. Tsutsui (2012) confirmed that the reattachment point will move forward at lower aspect ratios, so these data are consistent. Tsutsui (2012) also presented a model of the flow based on oil film measurements, seen in Figure 2.14, which contains a second separation bubble caused by the separation of the reversing recirculating flow.

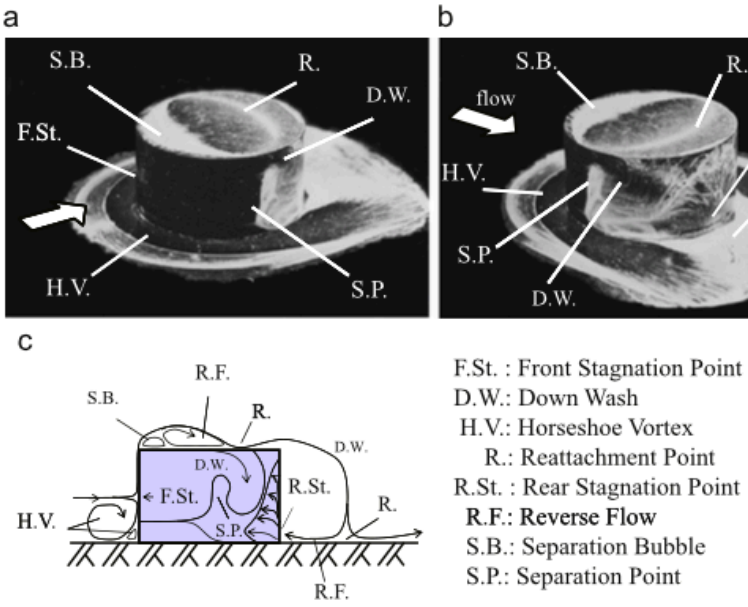

Figure 2.14: Summary of flow around a short finite cylinder a) front ¾ view b) rear ¾ view from Tsutsui (2012). Reprinted from Journal of Wind Engineering and Industrial Aerodynamics, vol. 104, T. Tsutsui, Flow around a cylindrical structure mounted in a plane turbulent boundary layer, pp. 239-247, Copyright (2012), with permission from Elsevier.

Numerical simulations have also been used in recent years to develop a better understanding of the small scale structures near the free end. Krajnović (2011) performed large eddy simulations (LES) for a finite cylinder of AR = 6. Krajnović found that the two foci were in fact the ends of a large vortex caused by the recirculating flow on the free end, forming the mushroom vortex. He also found the smaller recirculating region that occurs close to the leading edge, as proposed by other authors (e.g. Holscher and Niemann (1996), Tsutsui (2012)).

Krajnović was able to also confirm the work of Hain, Kähler, and Michaelis (2008), in showing that the tip vortices were time-averaged structures, and only small structures were visible instantaneously. However, these structures were shown to have a dominant rotation in the direction of the time-averaged tip vortex. Both Hain, Kähler, and Michaelis (2008) and Krajnović (2011) saw two instantaneous counter-rotating vortices located with the same position and rotation of the time-averaged vortices, with one side stronger than the other.

2.5 Pressure Distribution

A number of studies have investigated the mean static pressure distribution on the free end of a finite cylinder. The published pressure distributions have, however, focused on only a small portion of the possible cylinder configurations (Re, AR, δ/D), and much is still to be discovered. Figure 2.15 summarizes the published studies as they relate to the cylinder aspect ratio. There is a clear gap of information on the pressure distributions for mid-level aspect ratios ($2 < AR \leq 7$). Differences in the published pressure data indicate that a change occurs between low and high AR, so this region must be investigated to garner a complete understanding of how the flow is influenced by aspect ratio. The range for mid-level AR is defined here based on prior research. Published data exist mostly for small AR, below the critical AR. An aspect ratio of AR = 2 was chosen as the upper bound for low AR because it is both below the critical AR and has a significant number of studies associated with it. An aspect ratio of AR = 7 was chosen as the upper bound for mid-level AR based on the work of Fox and West (1993), summarizing the work of Okamoto and Yagita (1973) and Farivar (1981), who indicate that there is a noticeable change in the fluid behaviour close to this aspect ratio.

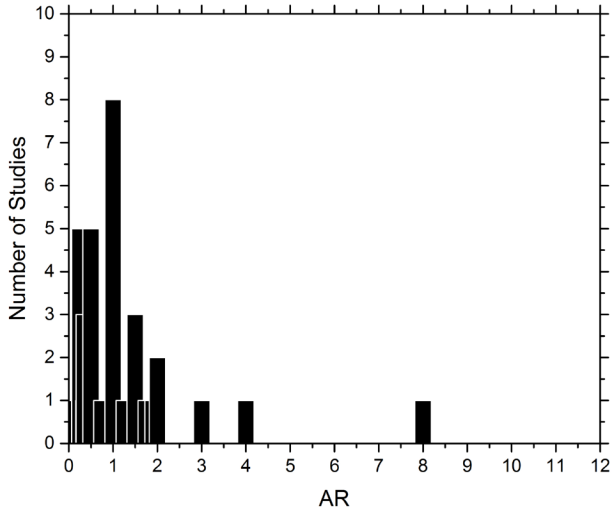

Figure 2.15: Comparison of studies in which pressure distributions have been collected for the free end of a finite cylinder. There is a clear focus on low AR, and a significant lack of information for AR > 2.

The pressure distributions in this research were undertaken to fill in the gaps (as illustrated in Figure 2.15) left by prior experiments, which began as early as 1967 (Purdy, Maher and Frederick 1967). The current experiment adds two tests to each of the aspect ratios (besides zero) up to AR = 11 shown in Figure 2.15, ensuring the effect of aspect ratio in this range can be captured.

The current research also uses a higher resolution of pressure taps than prior studies. Most studies do not report the layout of their pressure taps, and as such their resolution is unknown, but Tsutsui (2012) placed taps within at least 3 mm of each other, with an increased concentration close to the edge of his cylinder. Studies to this point have not placed pressure taps on the cylinder edge, as the shape of the tap would be compromised by the edge and the accuracy of the pressures would then be compromised as well. The present work has a tap placed near the edge, but does not attempt to resolve the surface pressures in between the tap and the outer cylinder edge.

The published free-end pressure distributions are difficult to form conclusions from due to variance in their formatting. There is consensus that the surface pressures should be represented

using the non-dimensionalized pressure coefficient, $C_P(r,\Theta) = 2((P - P_\infty)/(\rho_\infty U_\infty^2))$ on a 2-D plot of the free end surface, where r is the radius of the cylinder and Θ is the angle of the pressure tap, measured clockwise from the $-x$ axis. Few authors report their rotational increment, though 15° is common (e.g. Purdy, Maher and Frederick (1967), Ozmen (2013)). The layout of the pressure taps, and the radial spacing between each tap, Δr, is more frequently addressed, and layouts can be quite varied, including straight layouts (e.g. $\Delta r/D = 0.019$, as in Yoshida and Hongo (1983) and $\Delta r/D = 0.05$, as in Dobriloff and Nitsche (2009)), straight layouts with increased resolution near the edge (e.g. $\Delta r/D = 0.013$ to $\Delta r/D = 0.13$, as in Ozmen (2013)), and an S-shaped pattern (e.g. $\Delta r/D = 0.0375$, as in Tsutsui (2012)). The published data include figures of both whole and half portions of the cylinder free end, and figures with an isometric view as opposed to a 2-D view. Some authors chose to use numbered contours to represent C_P, while those that selected a colour map did so without a consistent colour scheme. It is therefore difficult to know whether the aspect ratio has a definite effect on the flow around the free end.

For this reason, the existing pressure distributions were collected and digitized using Origin software. This method enabled a dataset to be generated for each plot, allowing contours to be generated in a consistent format. In all, 38 plots were compiled from 14 studies, spanning a range of AR from AR = 0.09 to AR = 8. Because these studies all occurred in different locations by different researchers, the methods, systems, boundary layers, flow conditions and Reynolds numbers are different. The thesis will span a larger range of AR while maintaining the same flow conditions (Re, δ/D). While these published data lack a consistency that would ease the determination of AR effects, they still offer some valuable insight, showing important areas of interest, including regions of high and low C_P, lines of potential reattachment, "eye-like" structures, and strong gradients throughout. These pressure features can give a clue as to the behaviour of the flow around the free end, and aid in the comprehension of the flow field itself.

The shapes of the contours reveal interesting effects as AR is changed. At the lowest AR, the region of minimum pressure is small and at the front edge of the cylinder. The maximum pressure region is very large, occupying the entire back half of the cylinder and up to 60% of the forward half, as in Figure 2.16 (a). There is very little pressure variation in this region, but there is a strong pressure gradient from its edge up to the minimum pressure region. As AR is increased, the size of the minimum pressure region increases and moves away from the leading

edge, as in Figure 2.16 (b). The size of this minimum pressure region appears to depend on both the aspect ratio and the boundary layer thickness, as there is a lack of trend consistency among the different data sets. In a few cases, particularly higher AR such as AR = 4 and AR = 8, there is evidence that two "eyelets" of minimum pressure develop on the front half of the face (e.g. Kawamura, et al. (1984), Hiwada, et al. (1984), Dobriloff and Nitsche (2009)), which can be seen in Figure 2.16 (c). These eyelets may be the ends of the mushroom or arch vortex formed on the upper surface, but there is not enough evidence in the available data to confirm whether they truly exist or are just an anomaly in the data. Research with consistent flow and boundary layer conditions is required to confirm the existence of these eyelet structures.

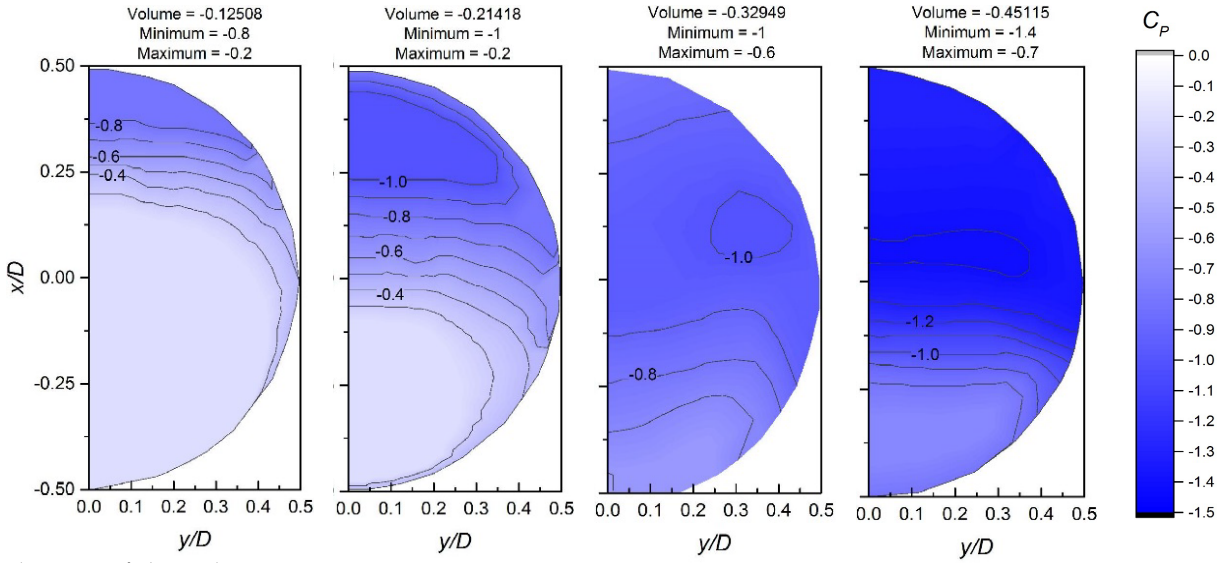

a) Tsutsui (2012), AR = 0.25, Re = $1x10^5$, δ/H = 2.6

b) Tsutsui (2012), AR = 1, Re = $1x10^5$, δ/H = 1.5

c) Hiwada et al. 1984, AR = 4, Re = $3.2x10^4$, δ/H = 0.25

d) Kawamura et al. 1984, AR = 8, Re = $3.2x10^4$, δ/H = 0.125

Figure 2.16: Comparison of C_P contours generated in Origin from published data. Flow is from top to bottom. Volume in this case refers to the integrated value for C_N. The contour lines are spaced for every inrement of C_P = 0.1.

The general trend is that the pressures decrease as AR increases. The lowest value is C_P = -1.4, and the highest value is C_P = 0. This means that the pressure coefficient everywhere on the surface of the free end is negative; it is directed away from the cylinder face. This means that there must be a net upward normal force generated by the pressure, though this force has not yet been reported in the literature. Because the current work will generate pressure contours for a significant range and increment of AR, it is an opportune time to study this normal force as well.

2.6 Drag Coefficient

The existing results for the pressure distributions revealed evidence of an overlooked force (the normal force) and significant gaps in knowledge, and so a similar compilation was done for the published mean drag coefficient (C_D) data with varying AR. Data were obtained from a variety of sources in the literature in which the mean drag coefficient is measured over several AR. Sources where C_D was only measured for a single AR, where the focus was on another component of the flow, were not considered, as variance in experimental conditions were expected to make it difficult to identify a trend from these data.

The C_D data were collected from published studies that measured the drag force at multiple aspect ratios with a force balance. Results are presented in Figure 2.17. It is clear that the published results are somewhat scattered, but a clear pattern of behaviour can be seen. The scatter can be attributed to differences in Re, δ, roughness of the cylinder, and turbulence in the flow. The fact that most previous studies have only focused on a narrow range of AR, or only used large increments in AR, makes it difficult to come to any definitive conclusion on how AR influences C_D. It appears that, in the drag coefficient plots, there is a sharply rising region for low AR, and then a fairly constant region, with a second possible rise seen in some tests for higher AR. While the main focus of the thesis research was to measure the normal force, it was convenient to also measure the drag force and improve the knowledge in this area as well.

The mean aerodynamic bending moment on the cylinder, primarily caused by the mean drag force, was another quantity that did not appear to be well-documented in any of the prior studies, though it is mentioned in ESDU 81017 (1981) and Taniguchi, Sakamoto and Arie (1981). However, the effects of the free end and the boundary layer thickness on the ground plane are expected to change the magnitude of this moment, and it would be worthwhile to study

the moment as well. Because the present work looks at a wide range of aspect ratio, and must use a force balance for the normal force, investigations of the drag force and bending moment were added to the measurements to extend the value of this work without requiring additional experiments.

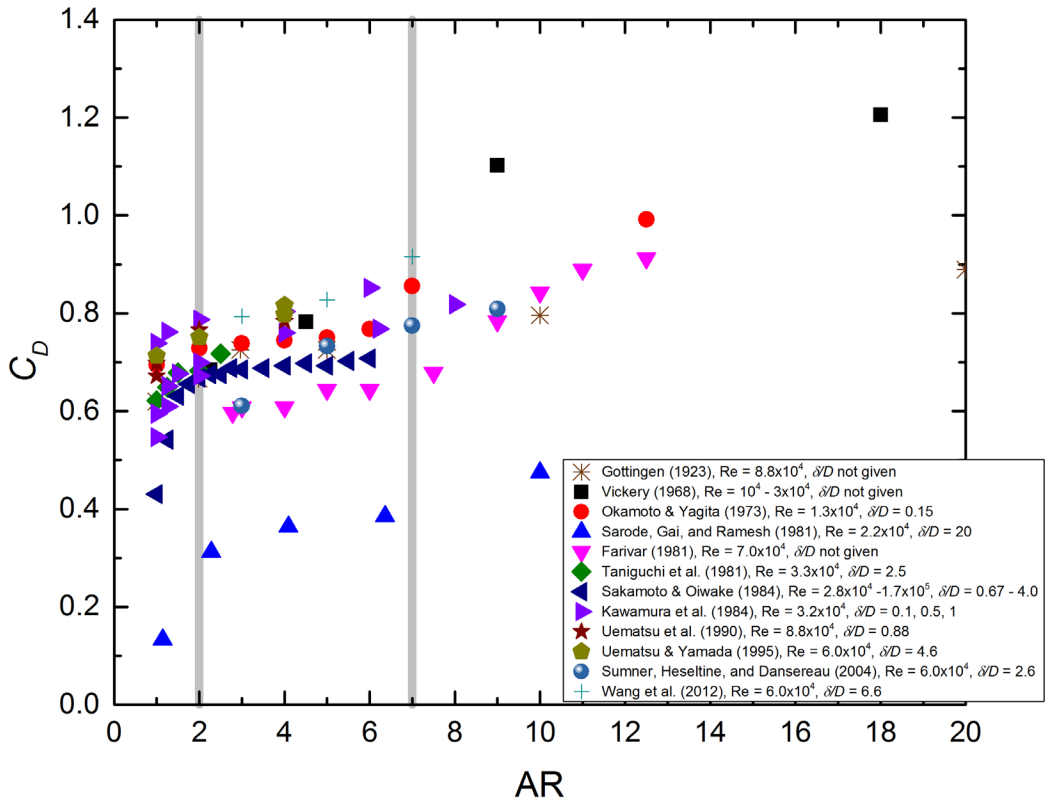

Figure 2.17: Published data for the effect of aspect ratio on the mean drag coefficient of a surface-mounted finite cylinder. Vertical lines show boundaries between regimes of different C_D behavior.

From the results in Figure 2.17, it can be noticed that the drag coefficient data of Sarode, Gai and Ramesh (1981) are much smaller than those in other studies. This difference may be a result of the very large relative boundary layer height that was used for their study ($\delta/D = 20$), which would be expected to drastically lower the drag force. However, since they did not report their definition for the drag coefficient, and few other studies have investigated boundary layers this large, it is difficult to confirm the reason for their lower C_D data. To better understand how

AR influences C_D, a large range of AR must be examined, using a small increment in AR, all in a single study, so as to have consistent experimental conditions (Re, δ/D, etc.).

2.7 Summary

Finite cylinder flows are complex as a result of the fluid interactions with the ground plane and the free end of the cylinder. A summary figure for the flow can be seen in Figure 2.18. At the cylinder connection to the ground plane, the adverse pressure gradient caused by the cylinder forces the oncoming flow to separate from the ground plane and roll up into a cross-stream vortex. The ends of this vortex are swept downstream by the freestream flow, forming a horseshoe shape around the cylinder. This horseshoe vortex can be seen in cross-stream plane measurements behind the cylinder, being close to the ground with a vorticity such that the vortex curls towards the cylinder. This vortex induces several smaller vortices on the cylinder wall and ground plane, and is inherently unstable, fluctuating in position and decaying, to be replaced with a second vortex that forms behind it. The flow behind the cylinder is more complicated. A pair of streamwise counter-rotating base vortices, rotating opposite the horseshoe vortices, but closer to the cylinder, has been reported for aspect ratios above a critical value. This critical aspect ratio could be between AR = 3 and AR = 7, depending on the flow conditions such as Re and boundary layer thickness. Another set of small vortices occurs close to the cylinder, caused by the recirculation, though the mechanism for the formation of this vortex has not yet been confirmed. It dies quickly in the wake as a result of the base vortices and backflow. There is a vortex that mirrors the horseshoe vortex on the lower rear half of the cylinder as well, but it is not shown in this figure.

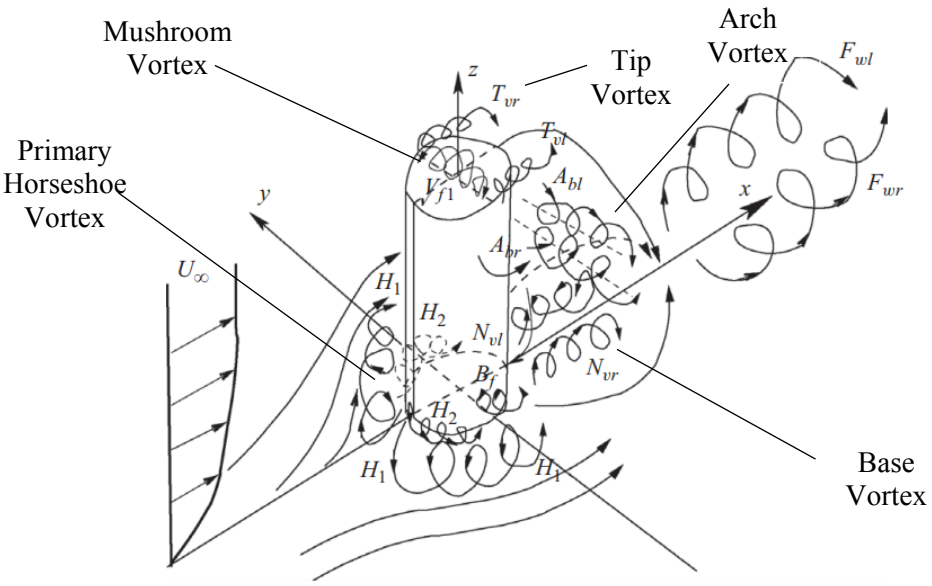

Figure 2.18: Summary of flow around a tall finite cylinder (Krajnović 2011). Vortices F_{wl} and F_{wr} are not described in the text but are presumed to be trailing vortices. Reprinted from S. Krajnović, Flow around a tall finite cylinder explored by large eddy simulation, The Journal of Fluid Mechanics, vol. 676, pp. 294-317, 2011, reproduced with permission from Cambridge University Press.

Figure 2.19 summarizes the flow over the free end. Flow around the free end separates at the leading edge, and reattaches on an arced line that lies closer to the trailing edge. The reattachment line moves forward for lower aspect ratios. The flow recirculates and forms a mushroom vortex on the surface, the bent axis of which forms two notable foci at the points of pressure minima on the surface. The recirculating flow may separate as well, forming a small recirculation bubble near the leading edge. This separation bubble has not been confirmed to appear in all tests. Somewhere along the side edge of the free end, two counter-rotating tip vortices, with opposite rotation from that of the base vortices, appear in time-averaged flow measurements. Flow from the tip angles toward the ground plane, creating a downwash flow, which induces a small cross-stream vortex in the near wake by the trailing edge of the cylinder.

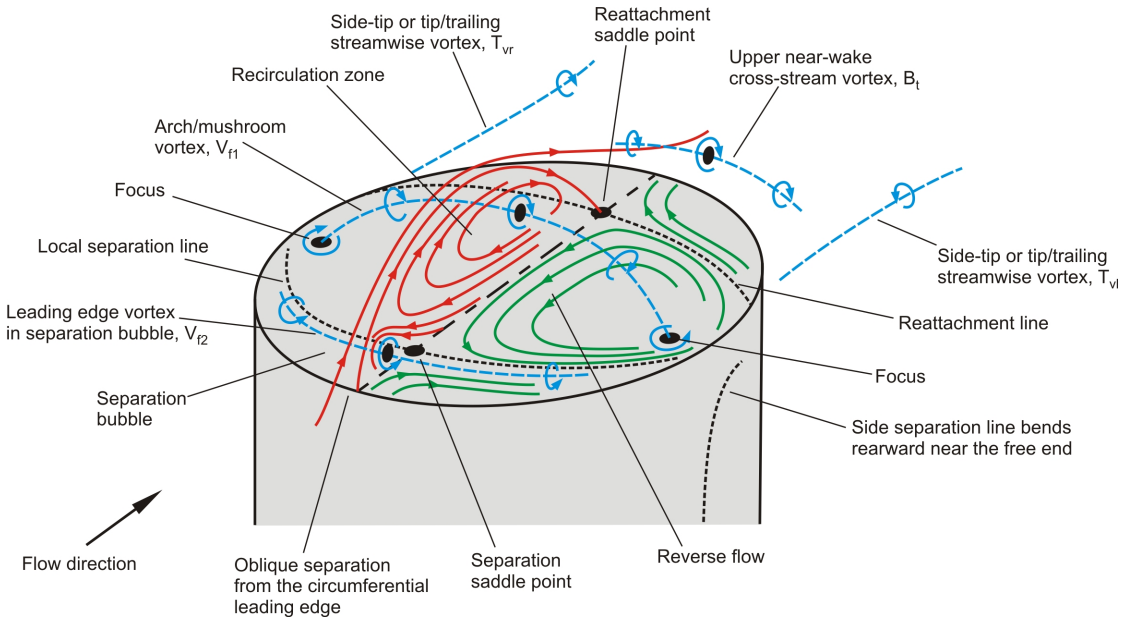

Figure 2.19: Summary of the free end flow structures from Sumner (2013). Reprinted from Journal of Fluids and Structures, vol. 43, D. Sumner, Flow above the free end of a surface-mounted finite-height circular cylinder: A review, pp. 41-63, Copyright (2013), with permission from Elsevier.

Karman vortex shedding is sometimes seen for a 3-D cylinder, as in a 2-D cylinder. However, below the critical aspect ratio, vortex shedding is mostly suppressed because the effects of the free end extend down all the way to the ground plane. These tip effects, mostly downwash, turn the antisymmetric Karman vortices into a symmetrically shed arch vortex. This arch vortex has inclined legs, seen as A_{bl} and A_{br} in Figure 2.18, which is also attributed to the downwash flow. Finite cylinders tend to have earlier separation from the sides when compared to an infinite cylinder, due to the increased base pressure caused by the downwash, though the effects of the free end can delay separation significantly near the free end, as in Figure 2.9. Despite the earlier separation, the effects of the tip flow tend to decrease the drag of the finite cylinder because of this higher base pressure. Most tests have been carried out at low aspect ratios, below the critical ratio, and the most likely wake models have come from these studies. It is not known whether these same flow structures will carry over to higher aspect ratios, or how the dominant structures change for a cylinder when familiar antisymmetric Karman vortex shedding becomes evident.

While there has been much study on finite cylinders, there is still much to be resolved about the flow. The upstream horseshoe vortex system and its instability is fairly well understood. However, the downstream flow structures at the ground plane are still left with questions. The formation mechanisms for the base vortices and the other small vortices that impinge on the rear wall of the cylinder (as shown in Figures 2.8 and 2.18) have not yet been studied in detail, though there is evidence that both exist. The same can be said for the small separation bubble, and the vortices within it, at the leading edge of the free end (as shown in Figure 2.19), as this has not been seen by all researchers. This may be due to a lack of clarity from oil film visualization, because the separation bubble is much smaller than the mushroom vortex and could easily be missed. The tip vortices are not very well understood either. They appear to be time-averaged structures, but whether they appear in phase-averaged measurements has yet to be confirmed. Further, the initiation site of these potential structures is not well understood, nor is the mechanism of their formation; they may be formed by the downwash, or help create the downwash. More study of the far wake would help to clarify their connection to the more familiar streamwise counter-rotating tip vortex pair, to see if these structures are in fact the same. General pressure contours on the free end surface have been made, but these pressures are time-averaged and very little data exist for the fluctuations of pressure on the free end surface. Behind the cylinder, the arch vortex system that is believed to form is not well described in the literature, and it is unknown what happens to it at higher aspect ratios. It is unknown whether the wake models for the finite square prism can in fact apply to the finite circular cylinder as well. In addition to these specific conditions, the effects of defining parameters of the flow are also not fully understood. Changes in Re, δ/D and AR must be more carefully investigated. A majority of tests on finite cylinders have been completed thus far on AR below the critical value (see Figure 2.15), and mainly in the subcritical Re regime, with very little information on flow at lower and higher Re. More study is needed to confirm the flow features that have been observed, and come to a better understanding of finite cylinder flow.

3 Experimental Set-up and Instrumentation

3.1 Introduction

In order to effectively study how aspect ratio influences the pressure distribution on the free end of a finite cylinder, an experimental apparatus was designed with pressure taps distributed on its free end, that could have its aspect ratio increased in small increments. The cylinders were mounted vertically to the force balance in a low-speed wind tunnel in order to measure the aerodynamic forces and moments. This chapter will outline the measurement systems that were used for this thesis research. Section 3.2 describes the wind tunnel, and the measurement systems for the freestream properties. Section 3.3 discusses the ZOC17 pressure transducers that were used to measure the surface pressures, while Section 3.4 describes the hot-wire probes used to measure the boundary layer velocity distribution and vortex shedding frequency. Section 3.5 details the cylinder models that were designed for the experiments, and Section 3.6 reports the freestream flow conditions. Section 3.7 reports on the two boundary layers that were used and their respective characteristics. Section 3.8 considers the calibration of the force balance, Section 3.9 outlines the experimental method, and Section 3.10 analyzes the uncertainty in the experiments.

3.2 Wind Tunnel

The experiments were conducted in the University of Saskatchewan wind tunnel, which is of a low-speed, closed-return type. A constant speed, variable-pitch fan, powered by a 100-hp electric motor, allows the flow in the test section to be set reliably between U_∞ = 5 m/s and U_∞ = 48.5 m/s. The wind tunnel can be run at higher velocity, but the maximum range of the currently used pressure transducers limits the allowable speed. Figure 3.1 shows a schematic representation of the wind tunnel.

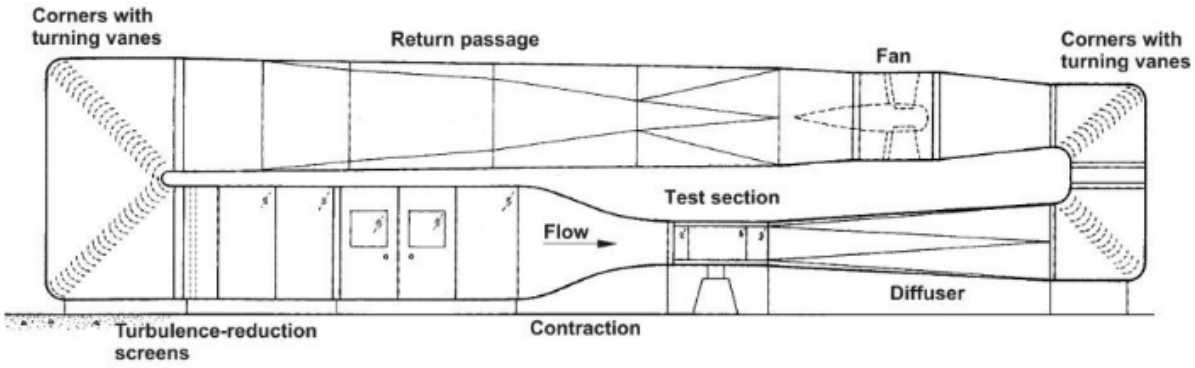

Figure 3.1: Schematic of the low-speed wind tunnel.

The air flow expands through a diffuser downstream of the fan and passes through two corners with turning vanes that smooth the velocity profile and reduce the losses from the 180° turn. The flow then runs through two turbulence reduction screens and enters a 2.97 x 2.4 x 7.0 m (height x width x length) settling chamber, before being accelerated through a 7:1 contraction. The test section of the wind tunnel measures 0.91 x 1.13 x 1.96 m (height x width x length). An aluminum ground plane is set up on the floor of the test section.

A three-axis traversing wing is mounted in the test section and is controlled by three stepper motors to move in the x, y, and z directions, with positioning precision of 0.006 mm, 0.012 mm and 0.013 mm, respectively. The stepper motors are controlled by IM1007 microstep drivers, through an NI PCI7344 motor controller card that is controlled using LabVIEW software installed on the wind tunnel's desktop computer.

A fourth stepper motor is used to control the rotation of the force balance turntable. The six-component force balance is composed of HBM PLC single-point load cells with a maximum capacity of 50 N. Three of the load cells measure vertical forces and moments in a T - bar configuration, while three more lie horizontally to measure drag and twisting forces. This configuration allows for the measurement of lift (F_L), drag (F_D), and normal (F_N) forces, as well as pitching (M_P), rolling (M_R), and yawing (M_Y) moments. The force balance had been previously calibrated for the measurement of F_L, F_D, and M_P, but was recalibrated to measure F_D, F_N, and M_y for this thesis research (see Section 3.8).

The data acquisition system (DAQ) uses a 16-bit National Instruments PCIe-6295 card, which is equipped with a multiplexer capable of 1.25 MS/s (mega samples per second) and is installed in the wind tunnel's desktop computer, where the data are output in LabVIEW.

The freestream static pressure (P_∞) and stagnation pressures (P_0) are measured by a United Sensor 3.2-mm-diameter Pitot-static probe, extending 160 mm from the test section wall, sitting 400 mm above the ground plane and 400 mm downstream of the entrance of the test section. This probe also has a built-in Type T thermocouple to measure the freestream air temperature, T_∞. The freestream density is calculated using the ideal gas equation, $\rho_\infty = P_\infty / RT_\infty$, where R is the gas constant for air (287 J/(kg·K)). The kinematic viscosity of the air, ν_∞, is calculated using the Sutherland equation as given below,

$$\nu_\infty = \frac{1}{\rho_\infty}\frac{\mu_\infty}{\mu_0} = \frac{\mu_0}{\rho_\infty}\frac{(T_\infty/T_0)^{\frac{3}{2}}(T_0+S)}{(T_\infty+S)}, \tag{3.1}$$

where T_0 = 273 K, $\mu_0 = 1.453\text{x}10^{-6}$ kg/(s·m), and S = 110.4 K, similar to equation (1.27) in White (2003). The value of μ_0 is known for a given T_0, and S is a constant chosen for air.

The static pressure line from the Pitot-static probe is used as a reference pressure for each differential pressure transducer. The main line is directed to a Datametrics Barocel Type 600A-1000T-513-H21X-4 absolute pressure transducer for direct measurement of P_∞. This transducer has a range of 1000 Torr (mmHg), and a reported accuracy of 0.15% of reading. The static pressure line also goes to a Datametrics Barocel Type 590D-10W-2QB-VIX-4D differential pressure transducer, and is used as the reference pressure against the stagnation pressure (P_0) line from the Pitot-static probe for measurement of the freestream dynamic pressure, $q_\infty = P_0 - P_\infty$. This transducer has a range of 10 inH_2O, and an accuracy of 0.053%, as described in detail in Section 3.10. Both transducers mentioned here are set to acquire data during the experiments at a sampling rate of 1 kHz, over a sampling period of 10 s. The remaining static pressure lines run to the two Scanivalve ZOC17 differential pressure scanners (described in Section 3.3).

3.3 ZOC17 Pressure Transducers

The two main sensors used to measure the static pressure distribution on the free end of the cylinder are ZOC17IP/8px DeltaP (ZOC17) differential pressure scanners from Scanivalve. These sensors have 8 inputs each, which means that two of them must be used to allow for 15 surface pressures to be measured at one time. ZOC stands for Zero-Operate-Calibrate, corresponding to the three modes in which the transducers can operate. These transducers allow the zero pressure output voltage and calibration curves of the 8 transducers to be checked and reset while remaining in-line. The ZOC17s for this experiment are muxless (they have no internal multiplexer), but the data acquisition card has its own multiplexer. The multiplexer is capable of switching at 50 kHz, and measurements are taken at 1 kHz. For time-averaged measurements, data are recorded and averaged over a period of 10 seconds. The ZOC17 is a piezoresistive differential pressure transducer. It is supplied with the freestream static pressure, P_∞, from the Pitot-static probe, as a reference pressure. The difference between the static pressure (P_∞) and the measured pressure (P) on the free end of the cylinder applies a mechanical strain to a conductive element, which produces a change in electrical resistance, a signal that can be related to the pressure. These sensors operate very well at high frequencies, and so are ideal for high frequency time-averaging. The full scale of the ZOC17 sensors is only 2.5 kPa, but the pressures being measured are very small as they only manifest as the differential pressure with respect to the freestream static pressure, (P - P_∞).

The 15 pressure lines from the instrumented cylinder (described in Section 3.5) are directed to these two pressure scanners. The lines are distributed such that the pressures from each half of the cylinder are sent to one ZOC17 unit. The remaining pneumatic inputs on the ZOC17 units are connected to the control and calibration pressures. These two lines come from a control panel with two regulators. A supply pressure, provided by a compressor in the basement of the Engineering Building, is connected to this control panel. The first regulator steps the supply pressure down to 90 psi (620.5 kPa). This pressure is directed to the ZOC17 units as a control pressure. The control pressure sets the ZOC calibration valve into purge, isolate or calibrate mode, allowing the ZOC sensors to be calibrated on-line. The second regulator steps the pressure down to 5 inH_2O (1225 Pa), and this pressure is directed to the ZOCs to be used as the calibration pressure.

The ZOC units come prepared with an internal calibration system. The ZOC17 pressure scanners are accurate and reliable, but are susceptible to a small amount of drift over long periods. The drift is very small, on the order of 0.1 Pa over a full day of measurements, but the small size of the measured pressures makes this a concern. Because of this, in regular wake measurements using a seven hole probe (e.g. Sumner, Heseltine and Dansereau (2004), Ogunremi and Sumner (2015)), the ZOC is recalibrated every 200 measurement points. For calibration, the unit is supplied with a calibration pressure of 3 inH_2O (from a compressor in the basement of the Engineering Building) that is set by a regulator, and is supplied to each of the measurement ports. A measurement is taken for each pressure and an offset and gain are generated from the known pressure, before the ZOC is switched back to the regular measurement mode. A Moore Type 40 pressure regulator is used for this purpose. It is reported to have an uncertainty of 0.03% of the regulated pressure. The regulated pressure is set by a dial, and the pressure is read by a BOC Edwards Type 590DF differential pressure transducer, with a range of 10 inH_2O and an accuracy of 0.05% reading, at a sampling rate of 1 kHz over a sampling period of 10 s. Because the pressure tests require only 180 measurement cycles, the ZOC units are set to recalibrate every 100 points for this set of experiments, meaning they are calibrated both at the start of, and midway through, each test. The effect of these errors and how they were found is described more fully in Section 3.10.

3.4 Hot-wire Anemometry Probe

The boundary layer velocity measurements were made with a Dantec hot-wire probe, mounted in the traversing wing. The probe is a CTA (constant temperature anemometer) type probe. A current is provided to a thin wire to maintain a constant temperature, and the current is adjusted based on the heat loss from forced convection. The voltage output can be calibrated with the air speed. This type of probe is capable of measuring both mean and fluctuating velocity components. Probes were connected to a Dantec Streamline anemometer unit, and run with Streamline software.

The probe used in the boundary layer was a Dantec 55P15 boundary layer hot-wire probe with a 90 degree mounting bracket. This probe has a single 5-μm-diameter platinum-plated tungsten wire with a length of 1.25 mm between the prongs. It has bent offset prongs so that the

probe body is away from the measurement volume and does not disturb the flow for measurements close to the wall. The probe was mounted parallel to the flow and was raised in increments from z = 1 mm to z = 300 mm to measure the full height of the boundary layer at the center of the ground plane. For the boundary layer measurements, the sampling frequency was 1 kHz, and samples were taken over 10 s.

To measure the vortex shedding frequencies, a Dantec 55P11 straight single-wire probe was used, but this probe was not calibrated. The specifications of this probe are identical except that the prongs are not bent, so the wire lies directly in front of the probe body. The probe was located 1D from the rear of the cylinder, and 1D from the y-axis centerline at the half-height of the cylinder for these measurements. The sampling frequency for this set of measurements was 5 kHz, and 100 measurements were taken for 1 s each, from which an averaged power spectrum was obtained.

Calibration of the boundary layer probe was done over a wide range of temperatures, from 22°C up to 38°C, to accommodate the entirety of the possible temperature range within a day of constant operation. The thin boundary layer was measured using this probe. The mean voltage data were used to generate a series of polynomial curves describing the behaviour of the sensor under different freestream temperatures. The measured voltage from the hot-wire was normalized for a temperature range and interpolated between the two closest temperature curves. The accuracy of the hot-wire measurement was tested by comparison to the freestream velocity from the Pitot-static probe, and found to vary by less than 2 m/s. This difference is significant, but was consistent for all freestream measurements. Because all results were normalized to the hot-wire measurement of freestream velocity (as opposed to the Pitot probe measurement), the results for the boundary layer thickness are not expected to have been affected. The thick boundary layer was measured using a recalibrated curve that showed a difference of only ± 0.2 m/s with the freestream.

3.5 Experimental Models

Two sets of cylinders were constructed for the experiments. The large diameter cylinders, with D = 48 mm, were segmented to enable the aspect ratio to be changed from AR = 0.5 to AR = 11 in increments of 0.5. The small diameter cylinders, with D = 31.5 mm, came in only five

aspect ratios, AR = 9, 7, 5, 3, and 1. The large diameter cylinders had a cylindrical cap with an aspect ratio of 0.25. A set of 15 pressure taps was distributed on the cap, and rotating the cylinder (using the force balance's turntable) allowed most of the surface to be measured by these taps. A series of collars (with heights of 0.5*D*, 1*D*, and 2*D*) allowed for the aspect ratio to be adjusted in steps of AR = 0.5. The cylinder base had an aspect ratio of 0.25, meaning the smallest AR was also 0.5. This choice was made to incorporate room for the locking mechanism on the collars while keeping a small minimum AR. Cylinders with AR < 1 have been extensively studied (e.g. Yoshida and Hongo (1983), Tsutsui (2012)), so it would not be worthwhile to focus heavily on this region. The increment of AR = 0.5 between possible aspect ratios was small enough to offer a close representation of the trends in the results within the possible time frame of the work. The base of the cylinder, the mounting collar, is pin-connected to a mounting bracket, which is mounted to the rotating force balance that is driven by a stepping motor. This stepping motor allows the cylinder to be rotated in steps of 1°.

The diameter of D = 48 mm was chosen for the large-diameter cylinders to allow the aspect ratio to be increased to AR = 11 without interference from the test section walls. This decision keeps the blockage ratio, the cylinder frontal area as a percentage of the test section cross-sectional area, below 3% for the maximum aspect ratio, AR = 11, while the cylinder height remains no greater than 63% of the test section above the ground plane. The roof of the test section has a slot cut into it to accommodate connections for a cylinder that spans the height of the test section. This hole was covered with aluminum tape for all experiments. Tests were completed at the highest aspect ratio for scenarios both with and without the tape covering, and with an additional flat plate installed to limit the roof boundary layer, and it was determined that the results were unaffected, meaning that the roof conditions were sufficiently far away as to not affect the flow around the cylinder.

The collars are joined by a pin-slot connection. A tight fit tolerance prevents side-to-side movement inside the connection. The slotted piece rotates ¼ turn once it engages the pin, and the rotation is stopped when the edge faces of the two collars meet. This tight fit prevents rotation by friction and ensures a smooth, unnoticeable joint between the two pieces. The quarter-turn joint design ensures that the pressure taps are always in the same position when the cylinder is connected, regardless of height.

The layout of the pressure taps on the free end was modelled after a previous experiment (Tsutsui 2012), but modified for better resolution. A schematic of the instrumented cap that was designed for use in the experiment, along with top and bottom views of the fabricated cap, is shown in Figure 3.2. The pressure taps are spaced such that there is 3 mm radially between them, and 10° in the tangential direction. The design used in Tsutsui (2012) was modified by offsetting the pressure taps on one half of the cylinder by 1.5 mm radially, effectively doubling the resolution. The layout of the pressure taps has the shape of a curve to ensure that the pressure taps do not interfere with the flow over top of any of the other taps, regardless of the angle at which the cylinder is oriented. The cylinder was rotated 180° in both directions so that each pressure tap measured a complete locus of 360 points. Because there is an offset of the pressure tap layout on the two sides, this method generates a full representation of the surface pressure, with 1.5 mm radially and 1° tangentially between each measurement point.

a)

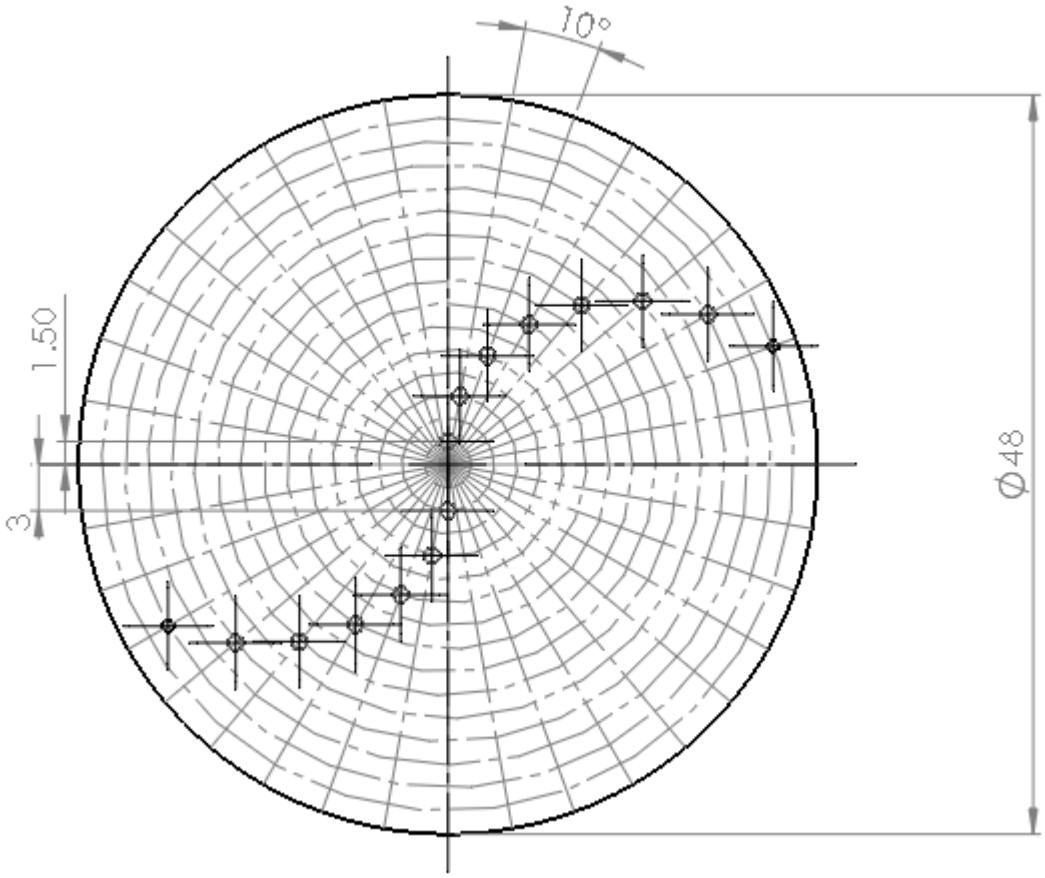

b)

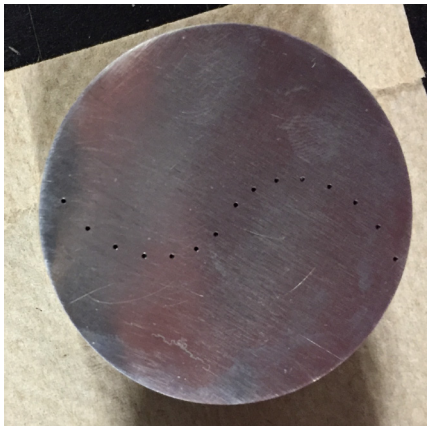

c)

Figure 3.2: a) Pressure tap layout for the instrumented cylinder cap (dimensions in mm) and b) fabricated cylinder cap, with sharp edges on the free end, and c) stainless steel tubulations connected to the underside of the cap.

The pressure taps, constructed of 0.040” (1 mm) stainless steel tubulations with a 0.030” (0.762 mm) inner diameter, are connected by urethane tubing to a circular pneumatic connector, from which the pressure runs through more urethane tubing into the two Scanivalve ZOC17 pressure scanners. The purpose of the pneumatic connector is to allow the pressure lines to be split and easily reattached in the proper order with reliable connections. This allows the collars to be added successively without having to completely disconnect all 15 pressure lines individually. The pneumatic connector is a 24 port circular connector from Scanivalve, shown in Figure 3.3.

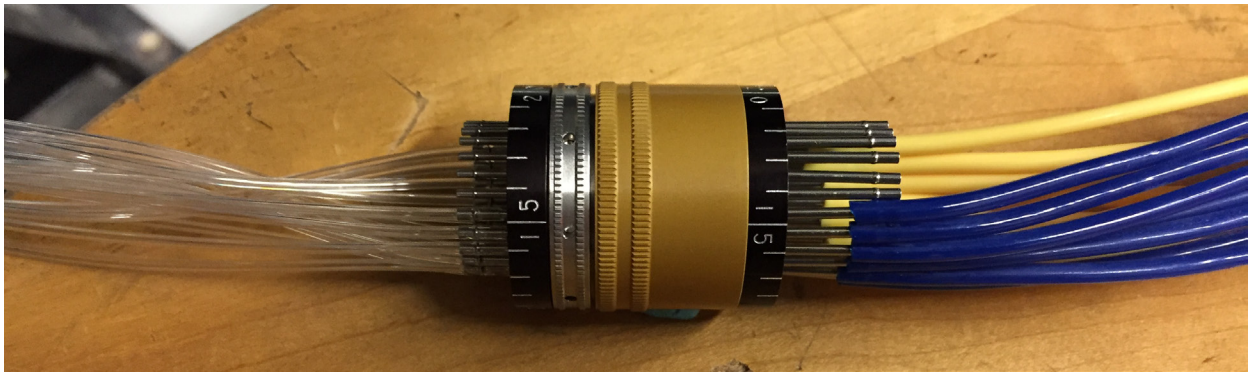

Figure 3.3: 24D round pneumatic connector from Scanivalve.

Theoretically, the flow within the pressure lines is static in steady flow, so the pressure drop though the lines is negligible during the measurement period when measuring a mean (time-averaged) pressure. This does introduce a difficulty when attempting to measure instantaneous pressure variations. For an instantaneous measurement, the pressure will be changing in the tubing. This means that there may be some pressure drop in the lines as a result of their length. The other consequence of tubing is that it tends to damp out pressure fluctuations, making these difficult to measure. To counteract this, the pressure lines were made as short as possible while still allowing the tallest cylinder to rotate without interference. The selected tubes were in two sections. The first section, of 0.040” urethane tubing, was 1 m long and ran from the cylinder cap to the connector. The second section of tubing had an inner diameter of 0.063” and was 2 m long, running from the connector to the Scanivalve ZOC17 pressure scanners. The damping ratio for this system is $\zeta = 0.11$ (Holman 2001), meaning the pressure fluctuations should only have minor attenuation by the pressure lines. Though their accuracy cannot be verified, due to a

lack of existing data on the topic, the current results offer a chance to compare the fluctuations to the pressure distributions and locations of certain flow structures.

3.6 Flow Conditions

The large-diameter cylinder is mounted so that it sits 1 mm over top of the ground plane, and is connected to the base by a thinner joint that sits inside a 1.5 mm gap from the hole in the ground plane (Figure 3.4). This closely mimics a true ground plane connection. The narrower part of the cylinder passes through the ground plane, but a similarly narrow gap prevents it from making contact with the ground plane, preventing contact that would affect the force measurements. The freestream velocity for the large-diameter cylinder was kept steady at U_∞ = 22.5 m/s, while the velocity was kept at U_∞ = 35 m/s for the small-diameter cylinders. This decision kept the freestream Reynolds number the same at Re = 6.5×10^4 for both cylinders. The temperature in the wind tunnel begins at T_∞ = 22°C, but generally increases as the fan is run, so the Reynolds number is subject to a reduction of 5×10^3 throughout the tests as a result of small changes in air density and viscosity. Because the freestream properties are constantly measured and the Reynolds number is within the stable subcritical region (Coutanceau and Defaye 1991), the temperature variation is not expected to have an impact on the results. Force measurements were also taken over a wide range of Re to verify this.

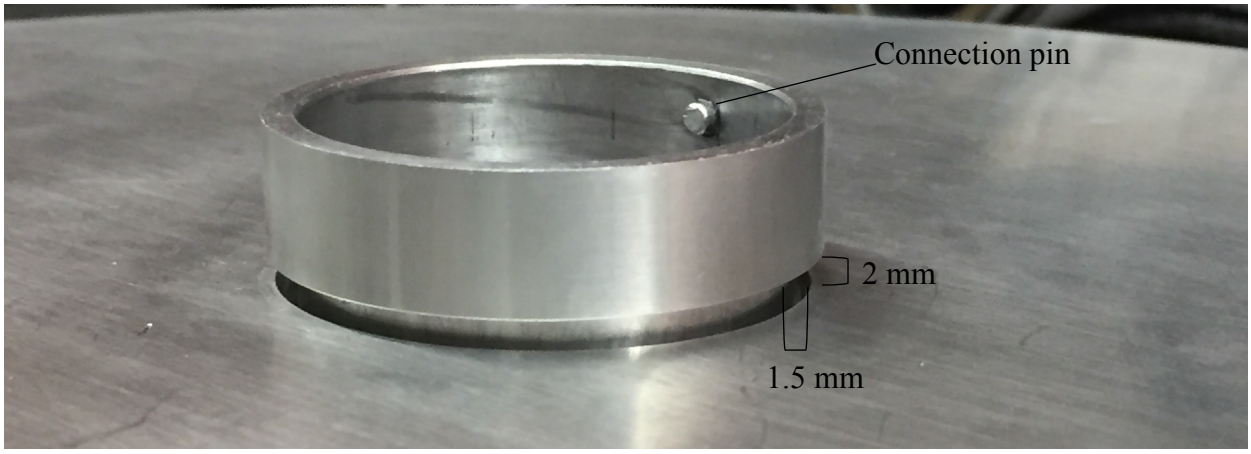

Figure 3.4: Large-diameter cylinder mounting collar connection near the ground plane. The gap between the narrower cylinder of the mounting collar and the hole in the ground plane is 1.5 mm, and the gap between the ground plane and the bottom edge of the cylinder is 2 mm. The connection pin slides into a slot on the mating piece and locks into place with a ¼ rotation of the mating piece.

3.7 Characteristics of the Ground Plane Boundary Layer

The two cylinders were each tested within two boundary layers, one tripped and the other untripped, resulting in four relative boundary layer thicknesses. The boundary layer thickness, δ, was set as the vertical location where the velocity first reached a value of $0.99U_\infty$. The untripped boundary layer had a thickness of $\delta = 29$ mm at the location of the cylinder at $U_\infty = 20$ m/s. A thick boundary layer was created by installing a 15-mm vertical plate on the ground plane at a distance 795 mm upstream of the cylinder center. This boundary layer had a less typical shape, but had a thickness of $\delta = 90$ mm at the location of the cylinder at $U_\infty = 20$ m/s. Although the two boundary layer shapes were not similar, they offered a reasonable approximation of the effect of changing the boundary layer thickness. The mean boundary layer velocity, U, is calculated to be $U = \frac{1}{\delta}\int_0^\delta U(z)dz$. The boundary layers and their respective turbulence intensities (TI = u'/U_∞, where u' is the root-mean-square value of the streamwise velocity fluctuations) are shown in Figures 3.5 and 3.6. The thin boundary layer closely follows the $1/7^{th}$ power law approximation, meaning it can be considered a typical turbulent boundary layer for a flat plate. Table 3.1 shows the calculated boundary layer characteristics. The boundary layer characteristics were calculated for a typical turbulent boundary layer outlined in White (2003), where the displacement thickness, $\delta^* = \int_0^\delta \left(1 - \frac{u}{U_\infty}\right) dz$, $\theta = \int_0^\delta \frac{u}{U_\infty}\left(1 - \frac{u}{U_\infty}\right) dz$, the shape factor, $H_\delta = \delta^*/\theta$, $\mathrm{Re}_x = U_\infty(0.895 - x)/\nu_\infty$, and $\mathrm{Re}_\theta = U_\infty\theta/\nu_\infty$.

Table 3.1: Characteristics of the turbulent flat plate (thin) and tripped (thick) boundary layers. The x-axis location of the probe is indicated relative to the large diameter cylinder. U_∞ = 20 m/s. δ is the boundary layer thickness, δ^* is the displacement thickness, θ is the momentum thickness, and H_δ is the shape factor.

Thin Boundary Layer						
Probe Location	**δ (mm)**	**δ^* (mm)**	**θ (mm)**	**H_δ**	**Re_x x 10^{-6}**	**Re_θ x 10^{-6}**
- 5 *D*	25	3	2	1.24	0.8	3.0
0 *D*	31	4	3	1.25	1.1	3.7
+ 5 *D*	34	4	3	1.25	1.4	4.1
Thick Boundary Layer						
	δ (mm)	**δ^* (mm)**	**θ (mm)**	**H_δ**	**Re_x x 10^{-6}**	**Re_θ x 10^{-6}**
- 5 *D*	84	17	12	1.45	0.8	14.3
0 *D*	90	14	11	1.28	1.1	13.2
+ 5 *D*	103	13	11	1.24	1.4	12.7

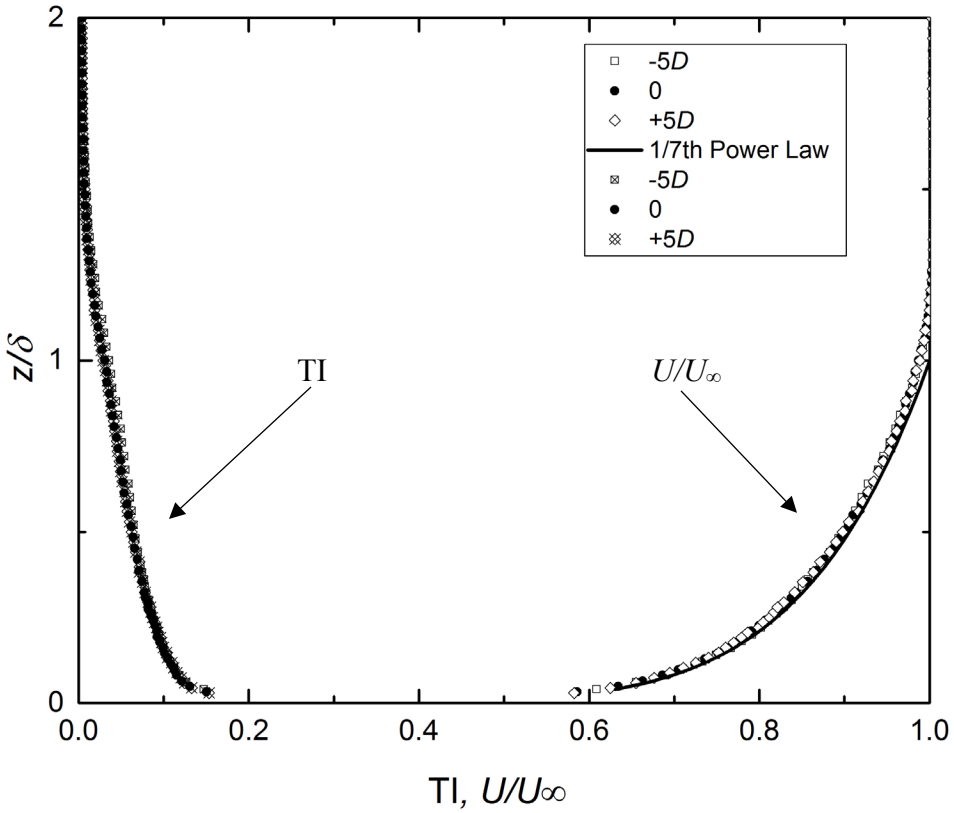

Figure 3.5: Turbulence intensity (TI = u'/U_∞) and normalized boundary layer profiles for the thin boundary layer (δ = 29 mm) for U_∞ = 20 m/s. Measurements occurred at the locations on the x-axis, based on the diameter of the large diameter cylinder.

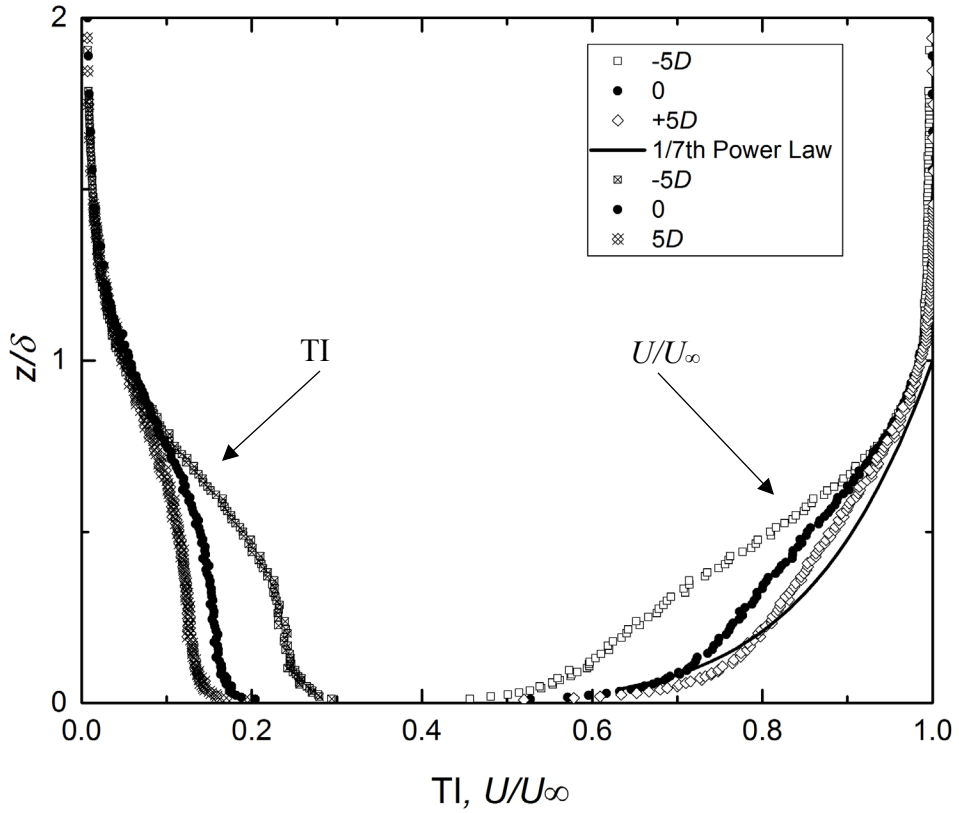

Figure 3.6: Turbulence intensity (TI = u'/U_∞) and normalized boundary layer profiles for the thick boundary layer (δ = 90 mm) for U_∞ = 20 m/s. Measurements occurred at the locations on the x-axis, based on the diameter of the large diameter cylinder.

For the thin boundary layer, the mean velocity profiles and turbulence intensity profiles collapse onto the same curve for all three values of x, meaning the boundary layer is fully developed at the cylinder location. For the thick boundary layer, the profiles do not collapse, meaning the boundary layer is still developing. The freestream turbulence intensity is very small in the thin boundary layer. The maximum turbulence intensity in the thick boundary layer at the location of the cylinder is TI = 0.2.

The integral length scales, L_u, are representative of the average size of the largest eddies in the flow. They are calculated as $L_u = U \int_0^\infty \frac{\overline{u(t)\,u(t+\tau)}}{u'u'} d\tau$, where $u(t)$ is the instantaneous velocity measurement, and $\tau = n/f_s$ is the time separation, where n is the number of samples, and

f_s is the sampling frequency. The turbulent integral length scales are $L_u = 0.5D$ for the thin boundary layer and $L_u = 1D$ for the thick boundary layer. These values are representative of what is found in the middle portion of the boundary layer. The integral length scales are larger for the thick boundary layer, which is indicative of the increased turbulence for this boundary layer.

Because the thick boundary layer is significantly more turbulent, there is some concern that it may not accurately represent the effects of simply changing the boundary layer thickness. While it would be preferable to have a large boundary layer with a similar shape to the thin boundary layer, this is among the few times, along with the work of Wang et al. (2006), that the effects of a change in boundary layer height have been directly studied in this context, and it will offer an idea of the type of changes that should be expected. While the shape is unusual, it is not unlike boundary layers that have been used in earlier studies, including those by Wang et al. (2006) and Bourgeois, Sattari, and Martinuzzi (2011).

3.8 Force Balance Calibration

The six component force balance, shown in Figure 3.7, has a prior calibration, but the existing response equations did not allow for a normal force (F_N) to be measured. In order to measure the normal force, it was necessary to recalibrate the force balance. A calibration rig was created (shown in Figure 3.8) for the specific purpose of calibrating the balance to measure the drag force (F_D), normal force (F_N), and yawing moment (M_y). Only load cells 1, 4 and 6 were used for this purpose. The calibration rig allowed the production of a positive normal force at the center, and positive or negative forces at two points offset from the center by 66 mm. Because these offset points were opposite the center and in line with each other, the application of a positive force on one and an equal magnitude negative force on the other allowed for the creation of a pure couple moment. The calibration was done first over a range from 0-4 kg (0 - 39.2 N), individually applied to each pulley, then with combined loadings, reaching a mass of 3 kg, making a total combined mass for the moment of 6 kg (corresponding to 3.88 N·m). Two more sets of calibrations took place the following day, confirming the results up to an 8 kg (5.18 N·m) moment. A matrix of coefficients was generated from the calibration data to be applied to the mean load cell voltages in LabVIEW, as per equation 3.2,

$$\begin{pmatrix} F_D \\ F_N \\ M_y \end{pmatrix} = \begin{pmatrix} C_{11} & C_{12} & C_{13} \\ C_{21} & C_{22} & C_{23} \\ C_{31} & C_{32} & C_{33} \end{pmatrix} \begin{pmatrix} E_1 \\ E_4 \\ E_6 \end{pmatrix}. \tag{3.2}$$

The coefficient matrix was generated through the use of a generalized inverse from the force and voltage data obtained during the calibration. By this method, the forces F_D, F_N, and M_y can be calculated from the mean load cell voltages, E_1, E_4, and E_6, which are averages of 10,000 samples taken at a sampling rate of 1 kHz. The uncertainty in this method is discussed in Section 3.10.

Figure 3.7: Wind tunnel force balance underneath the ground plane. Flow in the wind tunnel is from left to right.

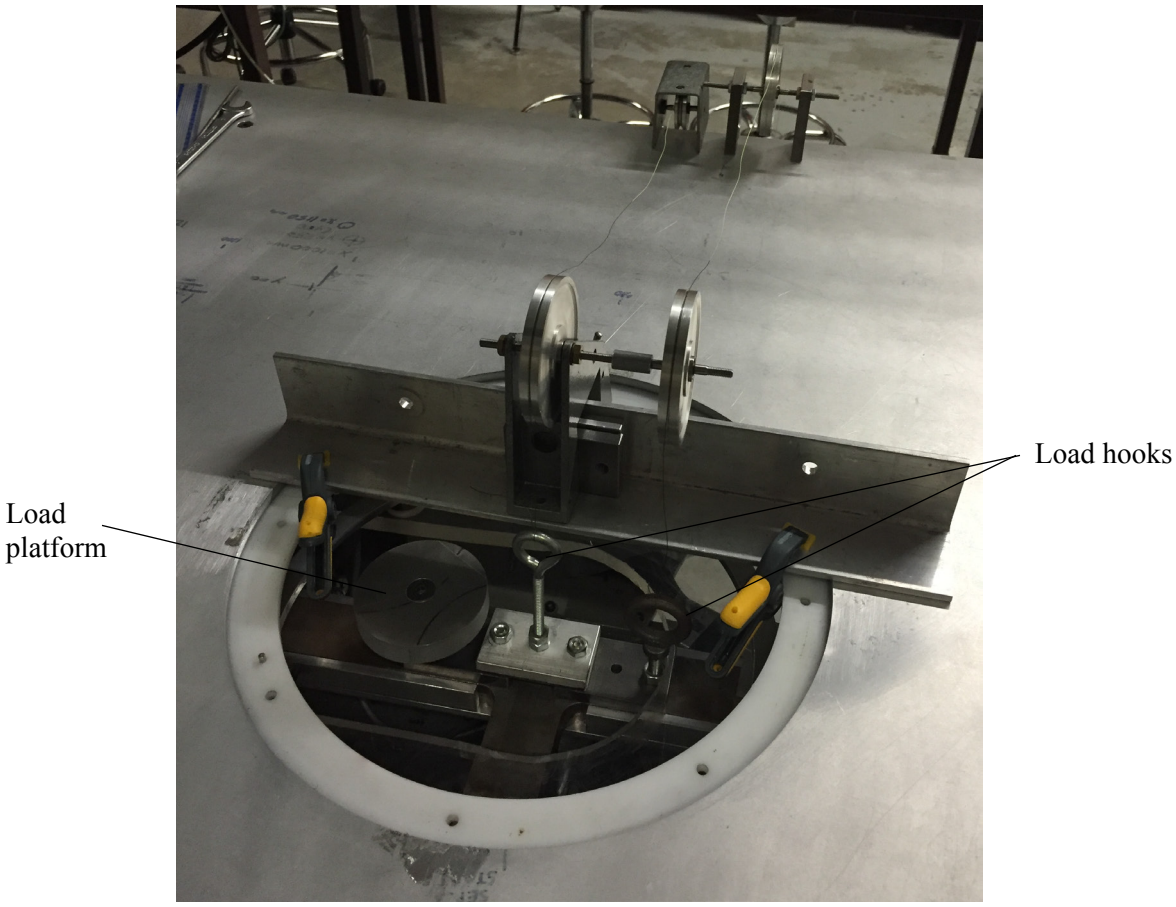

Figure 3.8: Force balance calibration rig, enabling a vertical force to be applied to the center post, and a pure couple moment to be applied using the outer hook and platform.

3.9 Experimental Method

The cylinders were mounted by bolts to the force balance turntable while it was disconnected from the yaw rotational motor and clamped in place. The small diameter cylinders were tested first, ensuring the forces were large enough to be measured accurately. The Reynolds number was selected because it could be achieved for both sets of cylinders within an acceptable range of U_∞. All AR for the large-diameter cylinders were measured under the same flow conditions. The pressure lines and connector were rested upon the center of the force balance during the large-diameter-cylinder tests, so that they would be accounted for in the load cell offsets. The hot-wire anemometer was then installed and vortex shedding measurements were completed, while the force tests were checked for repeatability. Upon completion of the force tests, the yaw motor was reconnected, and the pressure lines of the full cylinder were connected

to the circular pneumatic connector. The cylinder was rotated 180° clockwise in increments of 1°, then was removed, turned 180° and reinstalled, and the same measurements were repeated. This method allowed a full 360° locus of points to be collected for each individual pressure tap, totaling 5400 points on the cylinder surface. Upon the conclusion of both force and pressure measurements, a thin, 15-mm plate was installed upstream to create the thick boundary layer, and this new boundary layer was measured with the hot-wire probe to ensure a noticeable difference from the original boundary layer. When this was confirmed, the force, hot-wire, and pressure tests were repeated under the same flow and measurement conditions for both sets of cylinders. The combined methods led to results for the drag force, normal force, bending moment, vortex shedding frequency and pressure distributions for 22 different aspect ratios spanning from $0.5 < AR < 11$, within four different values of δ/D.

3.10 Uncertainty Analysis

The measurement system for the experiments was capable of generating accurate sets of data for several flow parameters. There is, however, an amount of uncertainty inherent within each component. These uncertainties will be described in this section.

Errors in the cylinder components are mostly negligible, as they do not significantly factor into the force and pressure coefficients, but will be mentioned here for completeness. The cylinder model itself has a diameter of $D = 48 \pm 0.05$ mm, which was verified with a caliper measurement. The angular position, Θ, has an associated uncertainty of $\pm 0.25°$, but the positioning was corrected after the pressure distributions were obtained.

The upstream flow conditions were measured constantly to monitor any changes and verify the consistency of the tests. A conservative estimate for the error in U_∞, based on the fluctuations during the tests, is $U_\infty = 22.5 \pm 0.5$ m/s. The error associated with the pressure transducer and the fluctuations is smaller, so this value was used as a conservative estimate in the calculation of the uncertainty in the Strouhal number. Within the range of z where the boundary layer thickness (δ) was achieved, the probe was moved in increments of 1 mm, so the boundary layer thickness has an associated uncertainty of ±1mm.

The reported uncertainty in the ZOC17 pressure scanners is given in the manual to be ± 0.20% F.S. for 10 inH_2O, including linearity, hysteresis and repeatability. This corresponds to 0.2% of 2448 Pa, or an uncertainty of 5 Pa in the differential pressure, $P - P_\infty$. The freestream static pressure is approximately P_∞ = 100 kPa, and the freestream dynamic pressure will be q_∞ = 278 Pa for a freestream velocity of U_∞ = 22.5 m/s. For an ideal flow around a cylinder, the circumferential pressure coefficient can reach as high as 1 and as low as -3. Real pressures, especially those on the free end, will not reach these limits. This means that the maximum possible uncertainty in measurements will be 0.005%. The full scale output for this sensor is reported to be 120 mV. The ZOCs are directed into an SCXI 1303 terminal block for data acquisition. This terminal block is designed to handle low voltages with minimal error.

The pressure regulator for the calibration pressure has an uncertainty listed as 0.03% of the regulated pressure. This corresponds to an uncertainty of 0.37 Pa for this case. This calibration pressure is measured also with the Datametrics Barocel Type 590 differential pressure transducer, and so is subject to its uncertainty as well, but this method greatly increases the accuracy with which the regulator can be set. Because the regulator pressure is measured, the error of the regulator itself should not be a factor, but it will still be considered as a precaution to account for any drift during the experiments.

The pressure taps have a hole diameter of 0.7 mm. This creates an uncertainty in the static pressure $P- P_\infty$ corresponding to 0.9% of q_∞ (Chue 1975). Following Bernoulli's equation, the error in the velocity will yield an equivalent error in the pressure. However, this error is applied to every pressure measurement and acts as an offset, so that the general trend of the pressure will not be affected. Because the taps are all the same type, the exact magnitudes of the pressures are not expected to have much influence on the pressure distribution, considering they are all measured relative to the static pressure. This uncertainty is understood, but is not accounted for, as it is not expected to factor significantly into the results.

The uncertainty in the Barocel Type 600 absolute pressure transducer is reported as 0.15% FS, with a resolution of 0.01% FS. Given a full scale of P_∞ = 100 kPa, the potential error in this measurement is 150 Pa. The ZOC and Datametrics units are differential pressure sensors, meaning they produce a reading of the difference between the measured pressure and the static pressure. The reading of static pressure is not used for this value, as the differential pressure is

the parameter of interest, so this uncertainty does not factor into the measurements. The uncertainty from the absolute pressure transducer exclusively affects the air density.

The differential pressure transducer, which is a Datametrics Barocel Type 590, has a reported uncertainty of 0.05% for linearity, repeatability of 0.01% of reading + 0.005% maximum applied pressure, and hysteresis uncertainty of 0.015%. The root-mean-square (RMS) value of these uncertainties can be calculated to find the total uncertainty for the dynamic pressure, which is 0.053%. Assuming it is oriented parallel to the flow, the United Sensor Pitot-static probe is expected to have negligible uncertainty due to the low Mach number and freestream turbulence intensity. The final uncertainty in the dynamic pressure is then 0.053%, or approximately 0.14 Pa.

Considering the uncertainties in both the ZOC17 and the calibration pressure, the total uncertainty in the differential pressure measured by the ZOC units is 5.1 Pa. The total uncertainty in the pressure coefficient, φC_p, can be calculated in the following way, from the differential method,

$$\varphi C_p = \sqrt{\left(\frac{\varphi(P - P_\infty)}{q_\infty}\right)^2 + \left((P - P_\infty)\frac{\varphi(q_\infty)}{{q_\infty}^2}\right)^2}, \tag{3.3}$$

where *φ(x)* refers to the uncertainty in the representative variable, *x*.

Accounting for all relevant uncertainties, and assuming a dynamic pressure of q_∞ = 278 Pa, the maximum total uncertainty in the calculated pressure coefficient is C_P = 0.046, an error of 1.54%.

The digital readout of the pressure coefficient has a resolution error of 5×10^{-9}, so it will not play any significant role in the uncertainty of the system as a whole. Therefore, the total uncertainty is the same as the design stage uncertainty.

The integration of the pressure coefficient was done in Origin software using the 2D Integrate gadget. This gadget uses the following numeric integral method,

$$\iint_{(\sigma)} f(x,y)dxdy = \lim_{\Delta x \to 0}\lim_{\Delta y \to 0}\sum_{i=0}^{m-1}\sum_{j=0}^{n-1} f(x_i,y_j)\Delta x \Delta y \approx \sum_{i=0}^{m-1}\sum_{j=0}^{n-1} f(x_i,y_j)\Delta x \Delta y, \tag{3.4}$$

where m and n are the rows and columns, respectively, of the given matrix. Within the matrix of points, $f(x_i, y_j)$ is calculated within Origin by $(f(x_i, y_j) + f(x_i, y_{j+1}) + f(x_{i+1}, y_j) + f(x_{i+1}, y_{j+1}))/4$. Origin applies an area around each point, so that each point is weighted according to the area over which it affects. The calculation method was tested with a series of known integrations with 5400 points, the same amount that is used for the real pressure distributions. These tests included both distributions covering halves of the cylinder and different annular distributions. In all tests, the results matched the theoretical values closely, with the maximum errors being attributed to the area interpolated between the boundaries of large jumps in pressure value. This is not a concern for the experimental results, as the pressures change smoothly between points, as opposed to sudden jumps. Where close values of C_P were used between calculation points, there was a maximum error of 1%. The integrated results are reported with less precision than the error, and as such it is negligible. Assuming negligible error in Δx and Δy, which are calculated and applied in Origin, the final error in C_N will be the error in C_P multiplied by the total area. This corresponds to an error of 0.0024% for the value of C_N based on the errors in C_P. This serves to represent the accuracy of both the measurement and integration methods. However, it is crucial to note that the pressure taps do not extend to the edge of the free end. This means there is uncertainty from the unaccounted pressures on the outermost rim of the free end. This uncertainty cannot be estimated, as there is no existing knowledge for the pressures at the edge of the free end. Though existing data could be extrapolated, the accuracy of this method could not be guaranteed, and the trend of the normal force is not expected to be significantly affected by the missing data.

The uncertainties in the force balance measurements are more easily quantified. As a vertical force had not yet been measured on the force balance, a new calibration was completed. The results of this calibration led to standard errors (based on standard deviation over the combined load calibration) for F_D, F_N, and M_y of 0.18 N, 0.15 N and 0.02 N·m, respectively. The uncertainties appear very large, and certainly are significant for the values being measured in these experiments. However, due to the small magnitude of the forces being measured, the high uncertainty is unavoidable. While these uncertainties are large, previous calibrations gave identical readings with lower standard error than that found in this calibration. It appears then, that this standard error is not an accurate method of estimating the uncertainty in these values,

particularly C_N, as the force itself is so small. Instead, the frequent fluctuations in measurements were doubled for use as the maximum uncertainty in C_N. This leads to a maximum uncertainty of 0.1 in either direction for C_N. Very little fluctuation was seen in the values for the drag and moment coefficients, so the standard error was used for these values. It would be beneficial for these tests to be repeated with a smaller scale force balance that will measure the small forces with greater accuracy. As this is one of the first times that some of these forces have been investigated, the accuracy is sufficient to give a relative magnitude and an idea of the general data trends that exist.

To estimate the uncertainty in the measured vortex shedding frequency, multiple measurements of the power spectrum were taken for one aspect ratio and the results were compared. The results did not reveal much variance in the dominant frequency, with the frequency changing by only 1-2 Hz between tests. This corresponds to an uncertainty in the Strouhal number of 0.006, or 4% of the smallest measured St. All relevant uncertainties are summarized in Table 3.2.

Table 3.2: Experimental uncertainty associated with main thesis parameters.

	Representative Measure	**Associated Uncertainty (±)**
Diameter, D	48.00 mm	0.05 mm
Angular Position, Θ	5.0°	0.5°
Boundary Layer Thickness, δ	29 mm	1 mm
Differential Pressure, $P - P_\infty$	2448 Pa	5 Pa
Absolute Pressure, P_∞	100.00 kPa	0.15 kPa
Dynamic Pressure, q_∞	278.0 Pa	0.1 Pa
Pressure Coefficient, C_P	0.80	0.05
Drag Coefficient, C_D	0.80	0.04
Normal Coefficient, C_N	0.60	0.1
Bending Coefficient, C_{My}	1.50	0.02

4 Results

4.1 Introduction

The results of the experiments reveal the effects of the aspect ratio and boundary layer thickness on several important parameters of the flow. The results indicate the existence of two critical aspect ratios, where the characteristics of the flow are expected to change. The measured forces, vortex shedding frequencies, and pressure distributions all have critical points at or near these aspect ratios. Section 4.2 discusses the published data for pressure distributions, and what the integration of these pressures revealed about the size and behaviour of C_N. Section 4.3 outlines the effects on the vortex shedding and Strouhal number. Section 4.4 expands upon prior studies and develops the knowledge of how the aspect ratio affects the drag coefficient. In Section 4.5, the normal force coefficient, C_N, is introduced and its behaviour is described. In Section 4.6, the bending moment coefficient, C_{My}, and its behaviour are described. Section 4.7 contains the detailed pressure distributions for the free end surface, while Section 4.8 focuses on the associated fluctuations of the free-end pressures.

4.2 Integration of Existing Pressures

The pressure distributions of $C_P(r,\Theta)$ found in the literature (see Appendix A), which are typically shown as isopressure contour lines, are generally inconclusive in terms of the effects of Re, AR, and δ/D, but do give a strong representation of the overall appearance of the free-end pressure distribution. The most evident observation is that the pressures on the face of the free end are all negative. This means that the integrated pressure produces a value for a force which pulls normal to the free end. This force has not received much attention in the literature, but may be a significant factor for cylinder supports or roof structures. The published pressure contours, once digitized, were supplied to the 2D Integrate gadget in Origin, which graphically integrates the given pressures. Through this method, normal force coefficient data were obtained, as shown in Figure 4.1. The pressure coefficient is negative, meaning that the atmospheric pressure inside the cylinder is larger than the pressure on the cylinder free end, so the resultant normal force tends to pull away from the free end.

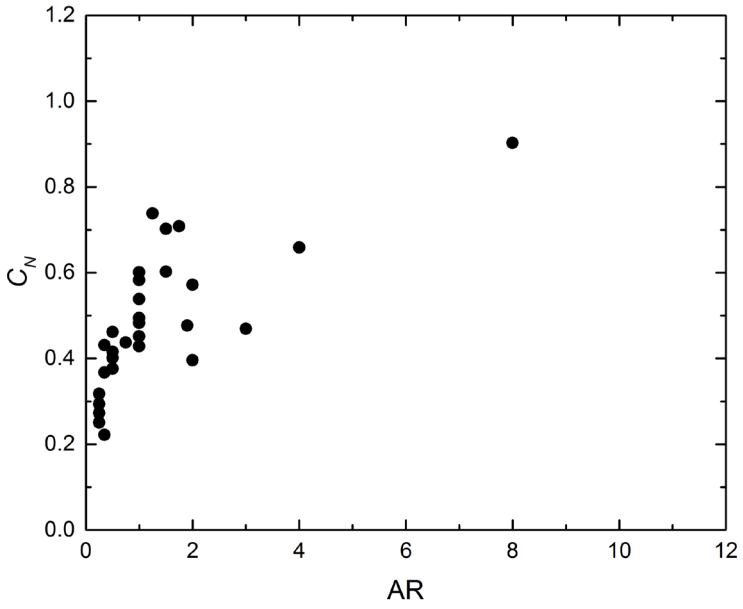

Figure 4.1: Normal force coefficient data obtained by integrating published free-end C_P data (listed in Appendix A).

The overall trend in Figure 4.1 appears to be an increase in C_N with aspect ratio. There is a significant amount of scatter in the data, owing to the many different flow conditions (Re, δ/D) among a small range of aspect ratios. The shape of the trendline may appear to be a logarithmic function, but the scatter makes this trend difficult to confirm. The scatter in the data is strongly illustrated at AR = 1, where seven different measurements yield values ranging from $C_N = 0.4$ to 0.6. In the thesis research, the new experiments used consistent flow conditions to check the repeatability of the measurements, and determine the effect of a few particular flow parameters, including Reynolds number and boundary layer thickness.

4.3 Vortex Shedding

The vortex shedding frequencies for the thick cylinders were measured in both thin and thick boundary layers to determine if the Strouhal number was affected by the aspect ratio. The power spectra of the velocity fluctuations are shown for each aspect ratio in Figure 4.2. The Strouhal number results are shown, similar to what was seen in published data, in Figure 4.3. The power spectra in Figure 4.2 show no peak for AR $\leq$ 1 in the thin boundary layer (Figure 4.1 (a) and (b)). Within the thick boundary layer, no peaks are seen for AR $\leq$ 3 (Figure 4.1 (c) and (d)), as antisymmetric vortex shedding is suppressed at these low values. The peaks that are seen are generally sharp peaks, though not particularly strong. Near AR = 5 in the thin boundary layer, the peaks become less pronounced. From Figure 4.3, two critical AR are somewhat evident, though they appear to be strongly affected by the boundary layer thickness. The critical aspect ratios of AR = 2 and AR = 6.5 are seen in the thin boundary layer, whereas the slope transition appears to be delayed to larger AR, and is less drastic, for the thicker boundary layer. The lower critical aspect ratio for the thick boundary layer case appears to be AR = 4, while the higher critical AR is difficult to discern, but may be close to AR = 8. The expected value of St = 0.20 for a 2-D cylinder can be extrapolated from the data, and appears to be reached near AR = 12. Vortex shedding is suppressed below the lower critical AR of AR = 2 for the thin boundary layer and AR = 4.5 for the thick boundary layer. The lower critical AR corresponds to the familiar critical AR identified by many researchers for finite cylinders, where the wake changes from antisymmetric Karman vortex shedding above this critical AR to a symmetric arch vortex below. These results are similar to Sumner, Heseltine, and Dansereau (2004), who used the same cylinders in a boundary layer of δ/D = 2.6, and found St = 0.16 for AR = 3, 5, 7, and 9.

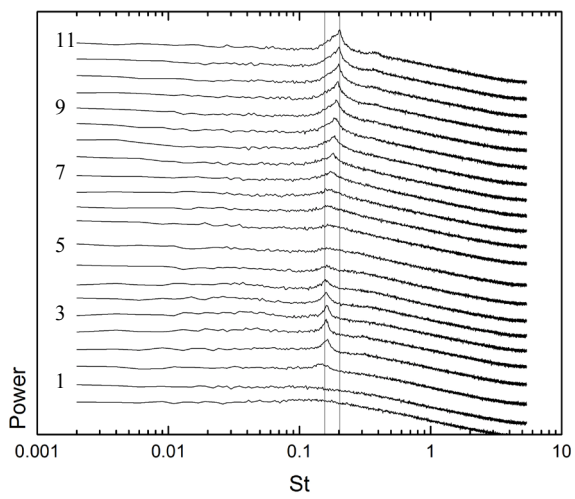

a) δ/D = 0.60, St = 0.156 and 0.203

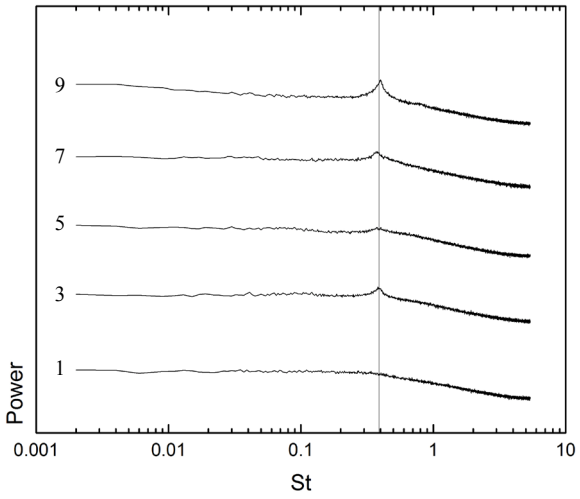

b) δ/D = 0.92, St = 0.389

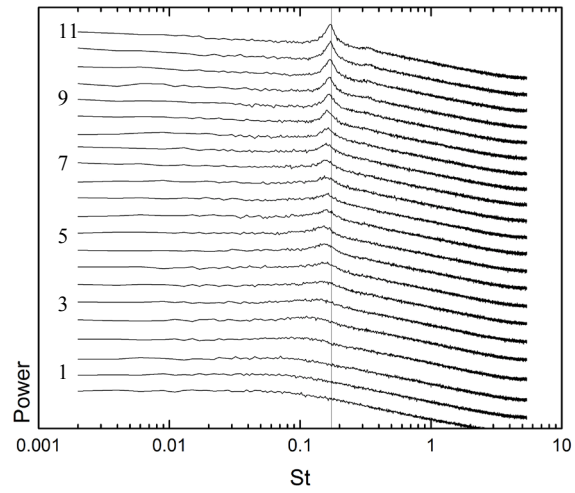

c) δ/D = 1.86, St = 0.173

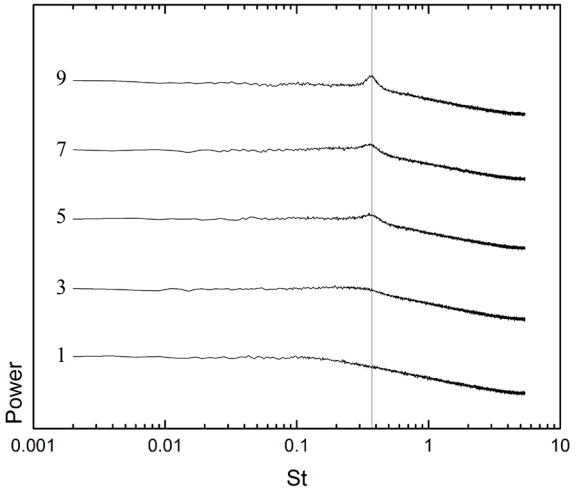

d) δ/D = 2.88, St = 0.372

Figure 4.2: Power spectra in the wake of the finite cylinders. Spectra are displaced vertically to be shown in order of increasing aspect ratio. The dominant frequency is shown by a vertical line for each cylinder case. The peak is seen to disappear for AR $\leq$ 1 for the thin boundary layer, and for AR $\leq$ 3 for the thick boundary layer. For the thin boundary layer, the peak disappears near AR = 5, and is reestablished at a smaller value of St for smaller AR.

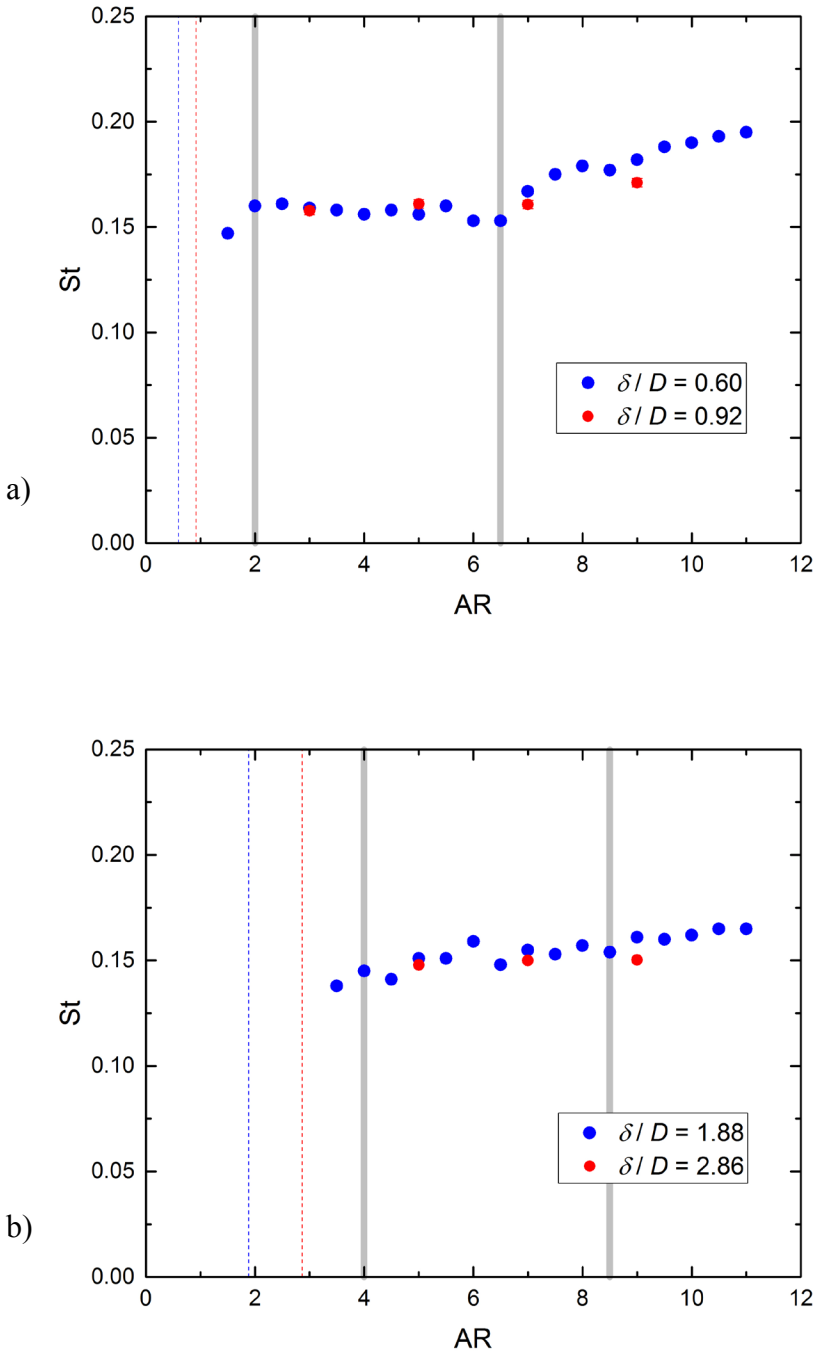

Figure 4.3: Strouhal number at mid-height for a finite cylinder immersed in a) a thin boundary layer and b) a thick boundary layer. The respective boundary layer thicknesses are shown as vertical dashed lines of the corresponding colours. The upper and lower critical aspect ratios for the thin boundary layer are shown as thick gray lines.

4.4 Mean Drag Force Measurements

As evidenced by Figure 2.17, the drag coefficient data from the literature also exhibited a degree of scatter, making it difficult to define a definite trend with aspect ratio. Few studies, aside from Sakamoto and Oiwake (1984), have investigated the AR between whole values, meaning a definite trend has been difficult to identify. The current experiments allowed a smooth curve to be generated that shows the behaviour clearly (Figure 4.4). The curve suggests that the slope changes twice within the AR range tested. Within the thin boundary layer, C_D (where $C_D = 2F_D/(\rho_\infty U_\infty^2 HD)$) increases rapidly at low AR as AR is raised, but plateaus near the lower critical aspect ratio of AR = 2.5. The drag coefficient stays nearly constant until the upper critical aspect ratio of AR = 5.5, where it begins to increase linearly up to the expected value for an infinite cylinder, $C_D = 1.25$ (Fox and West 1993). These critical aspect ratios were chosen as the ends of the nearly-constant region, before the curve behaviour changes.

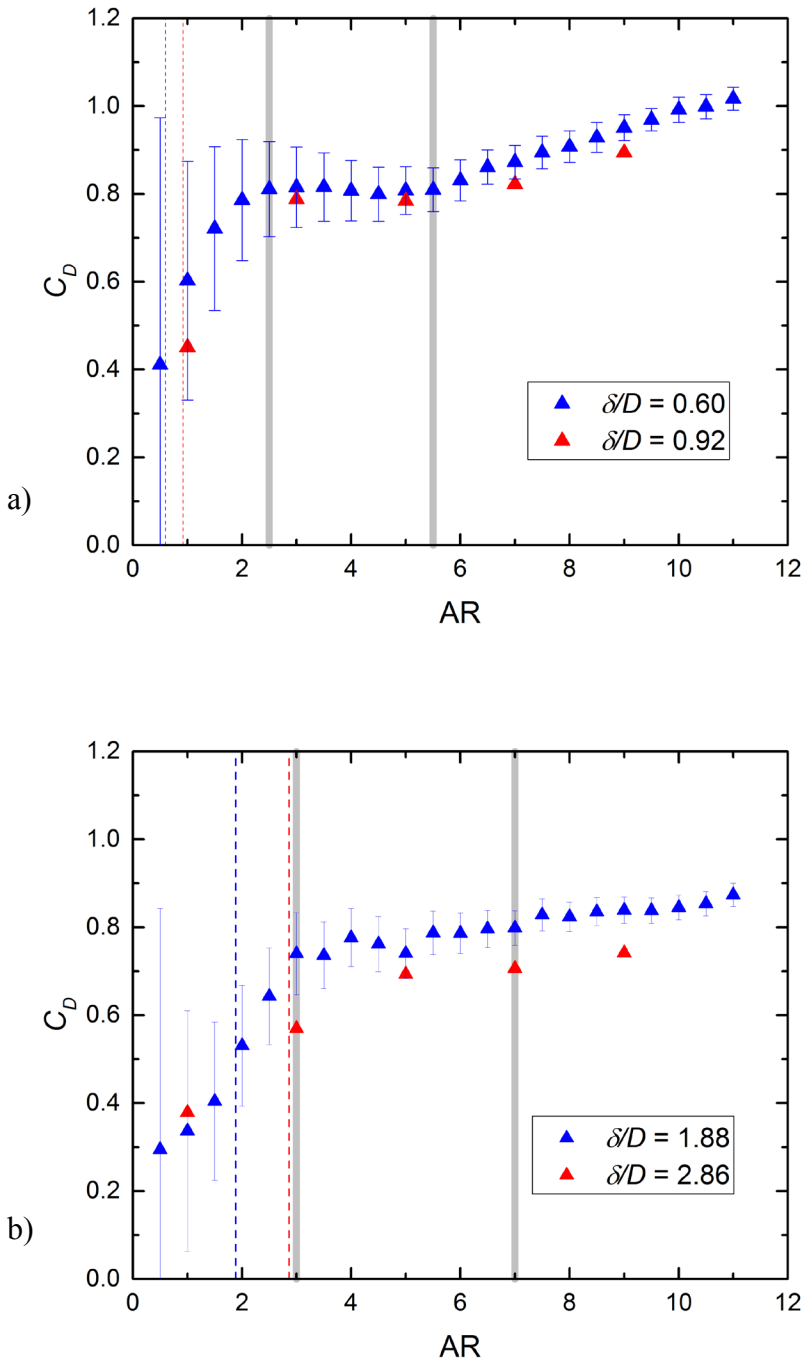

Figure 4.4: Variation of mean drag coefficient with aspect ratio for a cylinder immersed in a) a thin boundary layer and b) a thick boundary layer. The respective boundary layer thicknesses are shown as vertical dashed lines of the corresponding colours. The upper and lower critical aspect ratios for the thin boundary layer are shown as thick gray lines.

The curves indicate three distinct flow regimes. Below AR = 2.5 for the thin boundary layer, the boundary layer flow is dominant. Because the flow velocity in the boundary layer is reduced, the corresponding drag is reduced from the case in which there would be freestream velocity, resulting in a lower drag coefficient. It appears that AR = 2.5 is the point where the boundary layer becomes insignificant, regardless of the size of the boundary layer itself. This may be true only within a range of boundary layer sizes, as the boundary layers tested in this experiment were smaller than $\delta/D = 3$, and the largest relative boundary layer did not generate enough data to verify the location of the lower critical AR. Between AR = 2.5 and AR = 5.5, the drag coefficient is nearly independent of AR. It is expected that this is because the boundary layer effects have become small, while the free end effects are still significant, but not changing with AR. It is likely that the change in the wake from symmetric to antisymmetric vortex shedding may occur at the lower critical AR as well. In this region (between the lower and upper critical aspect ratios), the drag coefficient is not affected by the AR, meaning the flow conditions are likely consistent for these AR. Above this AR, the drag coefficient begins a linear increase to the value for an infinite cylinder ($C_D \approx 1.2$). In this region, the free end effects are reduced as the size of the unaffected wake region behind the cylinder grows with the AR. The downwash and upwash flow regions are less significant in the context of the full cylinder, and the drag in the center portion of the cylinder is equivalent to that for a finite cylinder. As this equivalent region increases, the drag coefficient will approach the value for an infinite cylinder.

The results with a thicker boundary layer are not as consistent as the thin boundary layer results. The thick boundary layer had increased turbulence and a different shape when compared to the thin boundary layer, and it is likely that this played a factor in the results. The break at AR = 2.5 is moved to AR = 3, which is different from the lower critical AR obtained from the Strouhal number in the thick boundary layer (Figure 4.2 (b)), and the second break at the upper critical AR is less pronounced. Though less easily identified, the second critical AR may still be seen, as the slope changes slightly near AR = 7. The difficulty in determining the critical point is likely a result of the increased turbulence in the flow, a result of the simple boundary layer trip that was used. As expected, the drag coefficient is lower for both cases of the thicker boundary layer because of the larger region of reduced flow velocity. Overall, the value of the drag coefficient reduces with an increased δ/D.

This new work serves to confirm published C_D data and enhance the understanding of the effects of certain flow parameters. Within the Reynolds numbers tested (10^4 - 10^5), there was no significant change in the value of the drag coefficient. The trend of the data is quite similar to that seen previously, especially by Okamoto and Yagita (1973), Sarode, Gai and Ramesh (1981), and Sakamoto and Oiwake (1984). These groups used a small AR increment and saw similar trends in their data, with a critical AR seen, where the drag coefficient is fairly constant above AR = 2. Sakamoto and Oiwake's (1984) data cut off at AR = 6, so the upper critical AR cannot be found in their results. The data of Okamoto and Yagita (1973) carry on to AR = 7, and there is a clear and sudden increase in the value of the drag coefficient at AR = 6, which is in close agreement with the upper critical AR found in the present study. Compared to the results of the present study, the rate of increase in C_D with AR is much more sudden in their data, which may be attributed to the very small boundary layer, $\delta/D = 0.15$, that was used in their tests. Sarode, Gai and Ramesh (1981) hypothesized a curve that appears similar to the one seen in the current data. Their curve was constructed from only five aspect ratios, meaning the critical points could not be clearly identified, and the curve itself was an approximation. The present study enhances and refines the understanding of the shape of this curve. Extrapolating the drag results from the present experiments to higher AR suggests that the 2-D cylinder drag value used by Fox and West (1993), $C_D = 1.25$, is reached at AR = 17 for the thin boundary layer, and AR = 36 for the thick boundary layer. AR = 17 is similar to the aspect ratio at which they determined the infinite cylinder region begins, AR = 20. Although Fox and West (1993) do not report their relative boundary layer thickness, it is expected to be negligible due to their use of an end plate, which is comparable to the thin boundary layer in the present experiment. The thicker boundary layer delays the 2-D cylinder behaviour to AR = 36. Results seem to be consistent for similar boundary layers, and the present results can be used to help determine how boundary layer thickness influences previous experiments.

An effort to resolve the effects of different flow conditions was made by creating contoured scatter plots to illustrate the effect of Re and δ on the existing and new data. These results are shown in Figures 4.5, 4.6, and 4.7.

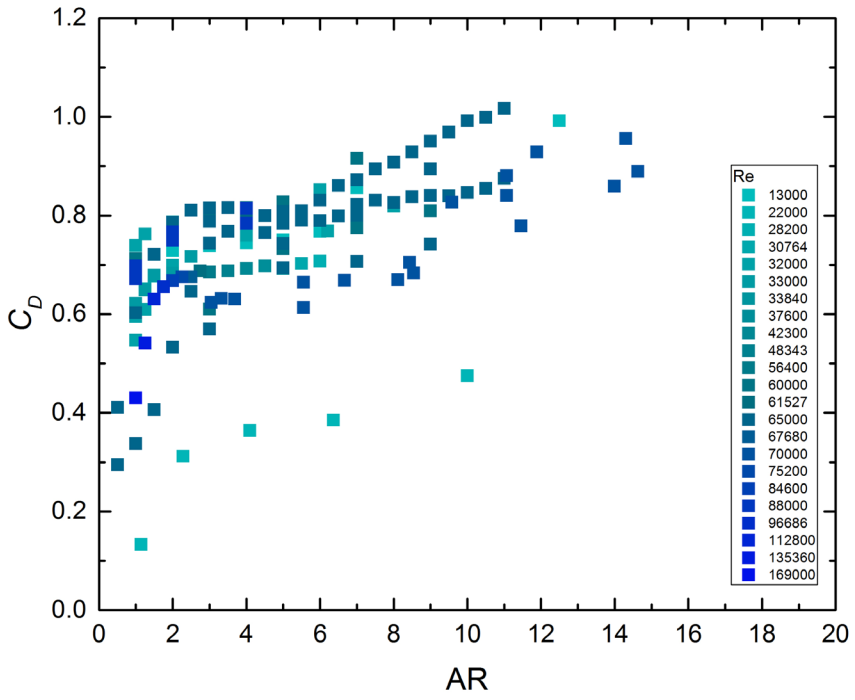

Figure 4.5: Effect of Reynolds number (Re) on direct measurement of the mean drag coefficient.

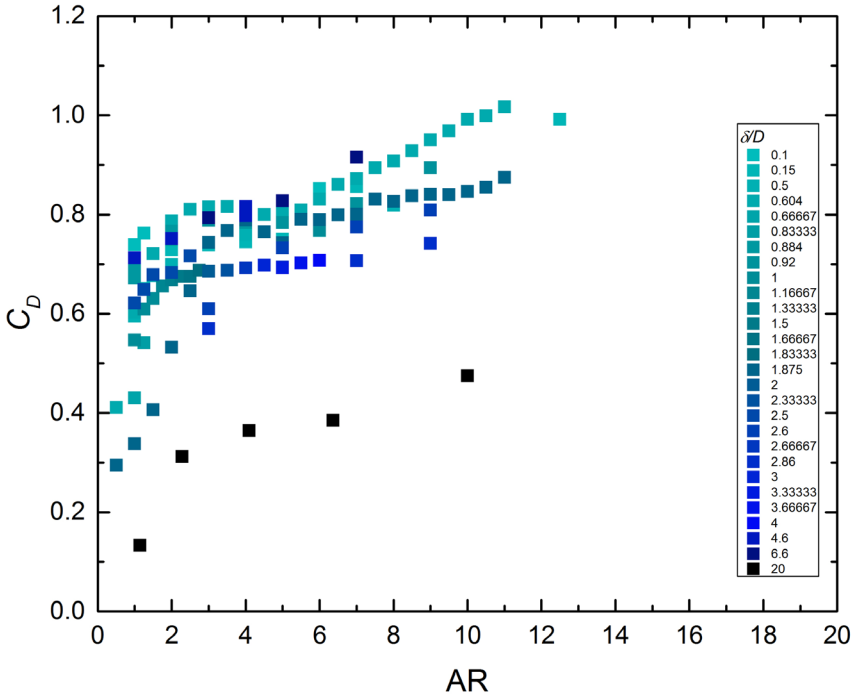

Figure 4.6: Effect of relative boundary layer thickness (δ/D) on direct measurement of the mean drag coefficient.

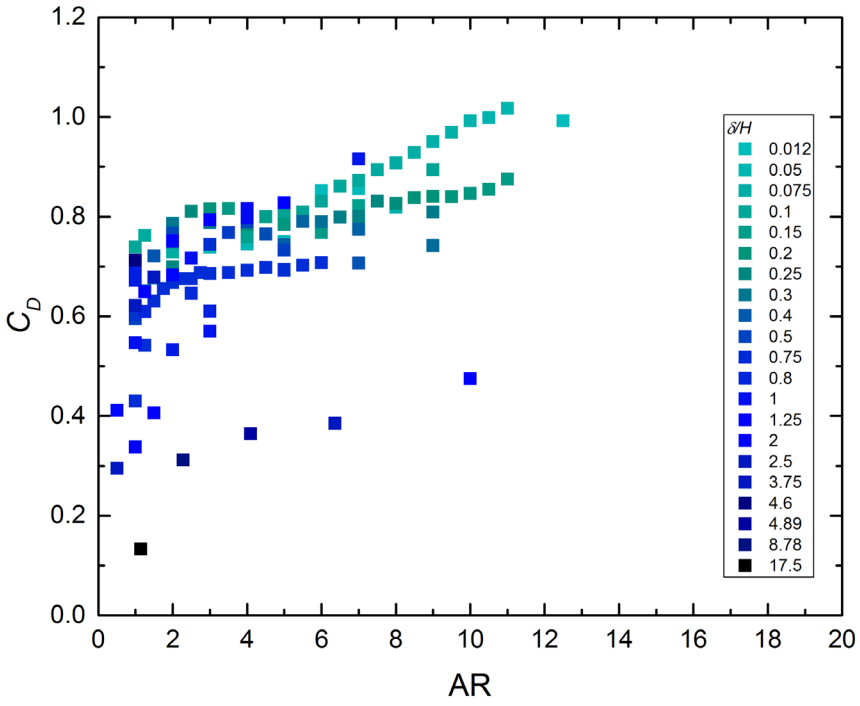

Figure 4.7: Effect of relative boundary layer height (δ/H) on direct measurement of the mean drag coefficient.

Figure 4.5 offers no real conclusions about Re effects. The range of Re is scattered throughout the results, and no clear pattern is evident. The boundary layer thickness plots, Figures 4.6 and 4.7, do reveal evidence of a dependence. The colour gradient clearly illustrates the drag coefficient being reduced as the boundary layer size is increased, which corresponds with the lower approach velocities in the boundary layer. The lowest values of drag are seen when the cylinder is strongly immersed in the boundary layer, as in the case of Sarode, Gai and Ramesh (1981), as this case corresponds to the largest percentage of the cylinder being exposed to a reduced flow velocity.

4.5 Mean Normal Force Measurements

The drag force and normal force, as with any force or moment, will have contributions from both the surface static pressure and the skin friction (wall shear stress). In the same way that the pressure-related component of the drag force can be obtained from the integration of the

circumferential pressures, the pressure-related component of the normal force can be obtained from the integration of the free end surface pressures. The pressure coefficients are negative, which means the pressures are smaller than the atmospheric pressure inside the cylinder. This difference in pressure is the cause of the vertical suction force on the free end. This force has received little attention in the literature. The normal force developed on the surface of a cylinder especially has been ignored. Only one study (ESDU 1978) attempted integration of the free-end surface pressures on a surface-mounted finite-height square prism. For both a square prism and a cylinder, a direct measurement of the total normal force has not been reported in literature.

The normal force for the finite cylinder was measured directly for the large-diameter and small-diameter cylinders and the thick and thin boundary layers. The large-diameter cylinder with pressure taps on the free end was used to measure the surface pressures so that the integrated normal force results (due to pressure only) could be compared with the total force results obtained from the force balance. Figure 4.8 shows the compilation of these results, and shows a significant difference between the direct measurements and integration results.

The normal force results indicate two critical aspect ratios, similar to the drag force results in Figure 4.4. The normal force coefficient ($C_N = 2F_N/(\rho_\infty U_\infty^2 \pi D^2/4)$) is small for both low and high aspect ratios. Below AR = 2.5 (the lower critical aspect ratio), the normal force coefficient increases rapidly with AR. For $2.5 \leq AR \leq 6.5$, the normal force coefficient attains a near constant value, and is insensitive to aspect ratio. For AR > 6.5 (the upper critical aspect ratio), the normal force coefficient decreases with increasing AR. This reduction is less rapid than the increase at low AR. Within the thicker boundary layer, the behaviour of C_N is similar at low AR, but the magnitude is reduced. For the thick boundary layer, both critical AR are reduced by 0.5, in contrast to the St and C_D data. However, at the upper critical AR, AR = 6, there is a slight peak in the normal force coefficient. Above AR = 6, the normal force coefficient follows the downward trend seen in the thin boundary layer. It is expected that C_N may tend towards a very small, constant value that is independent of AR as the cylinder height increases and approaches the behaviour of a 2-D cylinder. As the cylinder AR increases substantially, the flow around the free-end will be increasingly less affected by the flow at the ground plane, meaning C_N should eventually reach a constant value. This value will be small, but contributions to the normal force

will remain from the separation at the leading edge of the free end and vertical wall shear stresses.

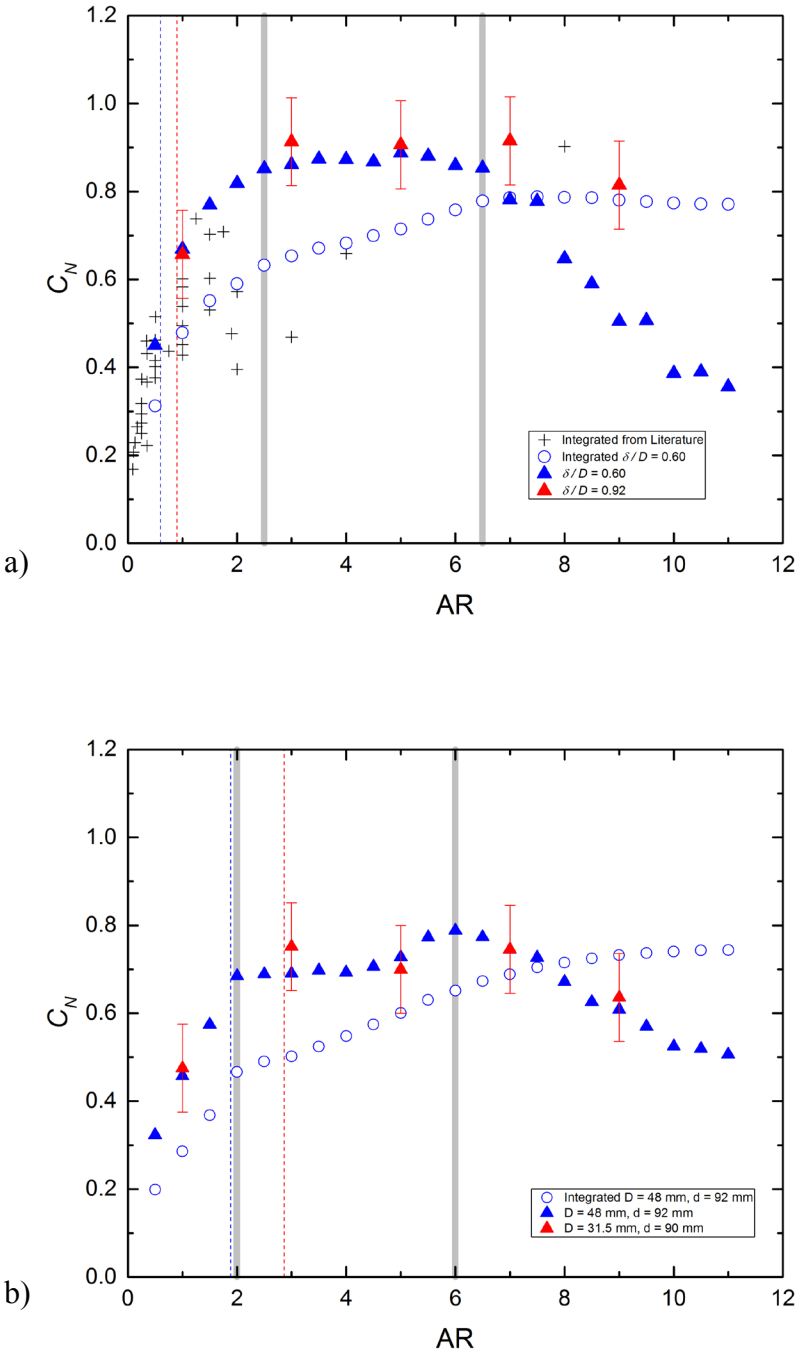

Figure 4.8: Variation of the mean normal force coefficient with aspect ratio for a finite cylinder immersed in a) a thin boundary layer and b) a thick boundary layer. The respective boundary layer thicknesses are shown as vertical dashed lines of the corresponding colours. The upper and lower critical aspect ratios for the thin boundary layer are shown as thick gray lines.

The C_N results from the integrated pressures on the free end of the cylinder (from the literature) disagree somewhat with the direct measurements of C_N. At low AR, the behaviour of the force is similar, but the integrated results do not reduce for AR > 6.5, and instead stay roughly constant. Vertical wall shear forces on the sides of the cylinder are expected to be acting to counter the normal force produced by these pressures at high aspect ratios.

4.6 Mean Bending Moment Measurements

The drag force acts to pull a cylinder along the wind direction, and as a result of the cantilevered mounting of the cylinder, a bending moment is caused at the cylinder-ground plane junction. This moment tends to tip the cylinder over in the wind direction, and is defined positive in that manner, i.e. positive about the *y*-axis, as shown in Figure 1.1. This moment, despite being a significant concern in the design of any constructed cylinder, has received very little attention in the literature. For most cases, applying the distributed drag force load as a point force at the midpoint of the cylinder will offer a conservative case for the bending moment, as the reduced flow velocity in the boundary layer should serve to reduce the moment magnitude. However, if a more accurate value is required, especially for small aspect ratios (like most buildings), this estimate is insufficient, and a mean bending moment coefficient similar to the mean drag coefficient should be used.

The force balance was able to measure vertical forces in both the positive and negative directions. Because two load cells were used to measure the vertical forces, a moment could also be determined from the difference between the outputs of the two load cells, which were aligned with the flow direction. The mean bending moment coefficient ($C_{My} = 2M_y/(\rho_\infty U_\infty^2 H^2 D)$) data that were obtained are shown in Figure 4.9.

a)

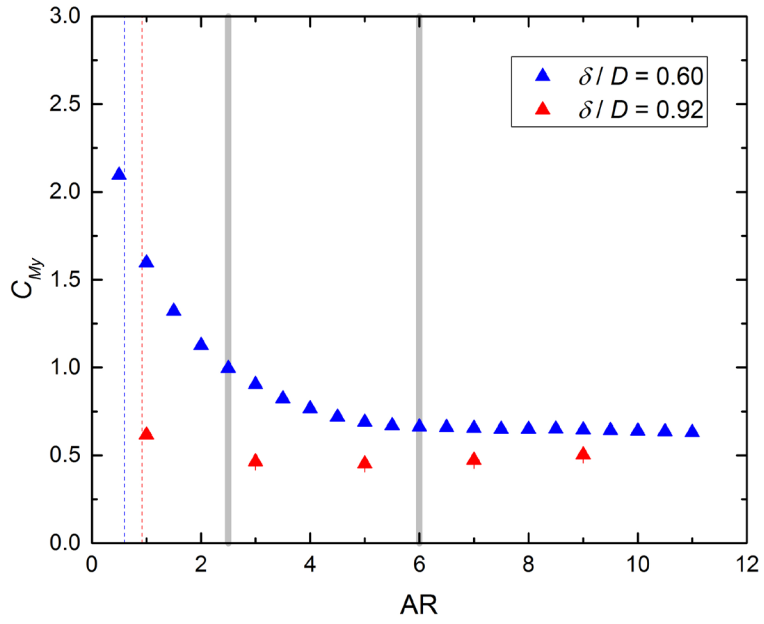

b)

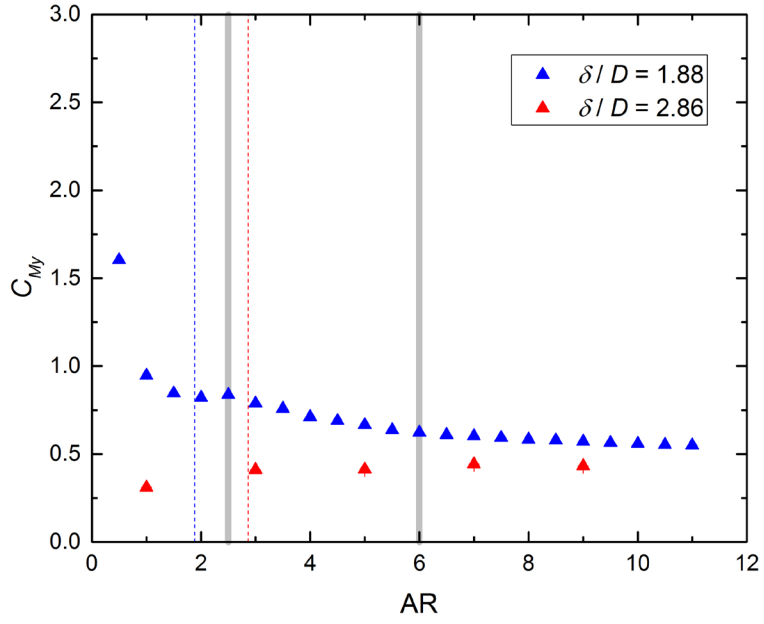

Figure 4.9: Variation of the mean bending moment coefficient with aspect ratio for a surface-mounted finite-height cylinder immersed in a) a thin boundary layer and b) a thick boundary layer. The respective boundary layer thicknesses are shown as vertical dashed lines of the corresponding colours. The upper and lower critical aspect ratios for the thin boundary layer are shown as thick gray lines.

The results from Figure 4.9 indicate only one critical aspect ratio, contrary to the results seen for St (Figure 4.3), C_D (Figure 4.4), and C_N (Figure 4.8). The moment coefficient is insensitive to AR approximately for AR $\geq$ 6. This value was chosen as the representative value for the upper critical AR, though it is seen to vary between AR = 5.5 and AR = 6.5 for different variables. In this range of AR, the boundary layer flow is less influential, and the moment coefficient is approximately constant. Between AR = 2.5 and AR = 6, the moment coefficient rises slowly as AR is reduced, and then rises rapidly below AR = 3. This may be evidence of the lower critical AR, which is represented in Figure 4.9 where the two boundary layers show significant difference, at AR = 2.5, as in the previous results. With a thicker boundary layer, the sudden rise is at AR = 1, which may be evidence of a different lower critical AR. The thicker boundary layer means that both the mean drag force, and the corresponding mean bending moment, will be lessened for a particular aspect ratio compared to the case of the thin boundary layer. The effect of the boundary layer is seen most clearly for AR $\leq$ 2.5. Below this value, the mean bending moment values clearly begin to diverge for the two boundary layers. The small-diameter cylinder results indicate that this behaviour is consistent for different relative boundary layer thicknesses. However, the C_{My} data for the small-diameter cylinder lie below the data for the large-diameter cylinder. The δ/D values for this cylinder are much higher, and so it is possible, if δ/D is sufficiently high, the boundary layer affects C_{My} more significantly over the entire range of AR, as opposed to only below the lower critical AR.

The present results show that the mean bending moment coefficient is increased for low aspect ratios. This is counter to the C_{My} results of Taniguchi, Sakamoto, and Arie (1981), but it is possible that their method of integrating the sectional drag force, as opposed to directly measuring the bending moment, contributed to this difference. The reduced drag values that result from the reduced flow velocity in the boundary layer would be expected to reduce the bending moment magnitude as well. However, the shape of the boundary layer means that there is a gradient in the flow force along the cylinder. Much of the force will be concentrated on the top half of the cylinder, close to the top edge for the smallest aspect ratios. This can be seen in the point of action (z_{cps}) for the drag force (called the center of pressure when generated using only integrated drag force values), seen in Figure 4.10, which was determined from the measured

mean drag force and mean bending moment. The point of action settles, above the upper critical AR, to a value just above $z/H = 0.5$. This is a result of the boundary layer, where reduced velocities contribute to a smaller force than areas outside of the boundary layer. This reduced force region lies at the base of the cylinder, meaning the point at which the total drag force acts will be slightly above the half-height of the cylinder. This is consistent with the results of ESDU (1981), in that the point of action is shifted closer to the half-height for larger cylinders, however the current results indicate a stronger shift at lower aspect ratios for thin boundary layers. The assumption of the mean drag force acting at $z/H = 0.5$ is reasonable, but not exact, especially for small AR.

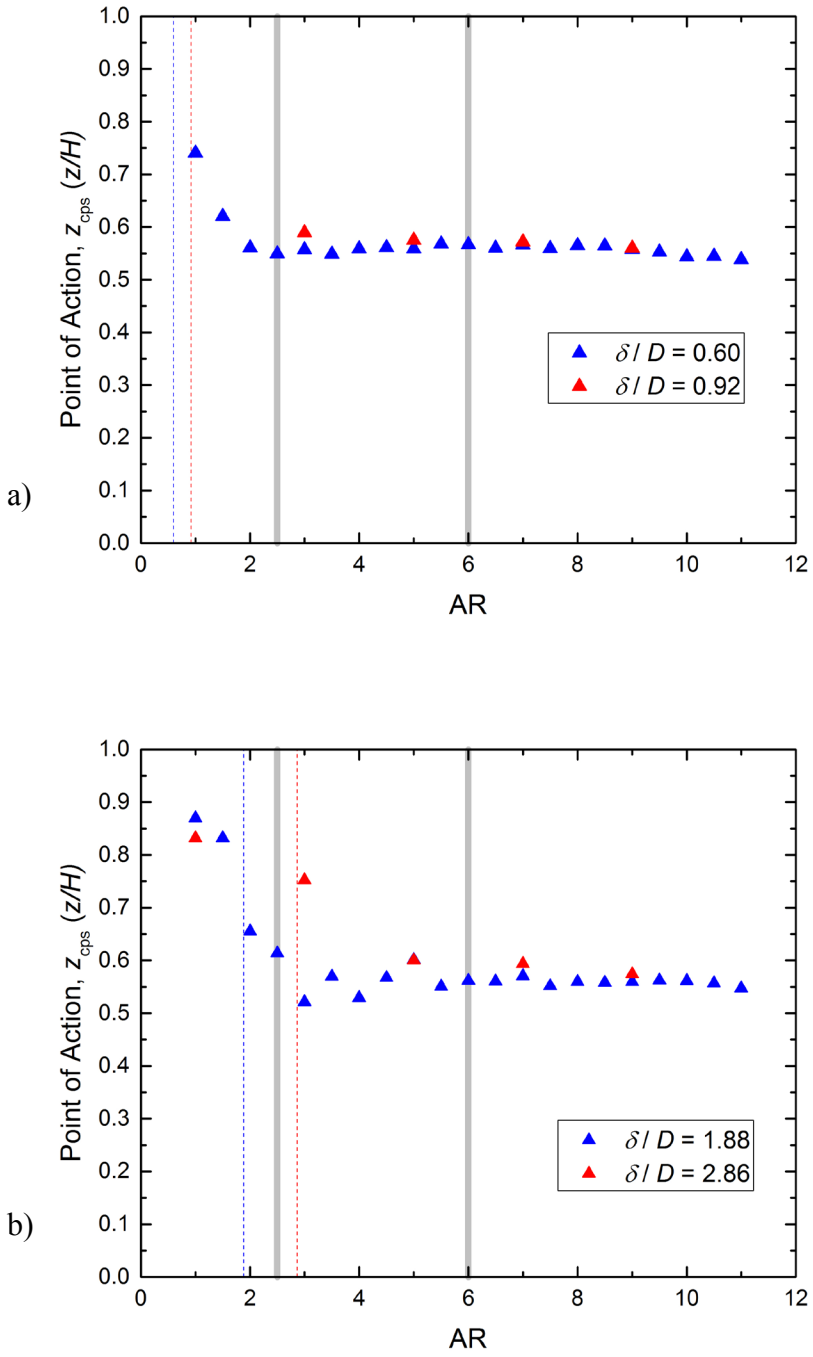

Figure 4.10: Variation of the point of action with aspect ratio for a surface-mounted finite-height cylinder immersed in a) a thin boundary layer and b) a thick boundary layer. The respective boundary layer thicknesses are shown as vertical dashed lines of the corresponding colours. The upper and lower critical aspect ratios for the thin boundary layer are shown as thick gray lines.

4.7 Free End Pressures

The mean pressure distribution on the free end of the cylinder has been investigated in the past, but a lack of consistency in the distribution of aspect ratio has made it difficult to draw conclusions about the effects of AR and δ/D. These published C_P distributions can be seen in Appendix A (a sample of which is shown in Figure 2.16) and serve to illustrate the main features of the free-end surface pressures. The region of minimum pressure on the upstream half of the free end, and the maximum pressure region on the downstream half are clearly evident. However, the existence of two eye-like spots, the movement of the pressure regions, and the effect on various flow structures, are not easily identifiable as a result of the different experimental conditions. Changes in boundary layer thickness, flow turbulence, and Reynolds number between published studies also make it difficult to conclude which parameter has the dominant influence on $C_P(r,\Theta)$.

The present experiments attempt to clarify the main influencing parameter by focusing on the aspect ratio. A surface pressure distribution for the free end was generated for 22 equally spaced aspect ratios, and for two different boundary layers. The cylinder diameter was kept constant as AR was changed (the large-diameter cylinders were used), so the freestream Reynolds number was maintained (at $Re = 6.5x10^4$) constant for all tests. Both parameters have the potential to have strong effects. The relative boundary layer height is indicative of how strong the effects of the boundary layer should be, while the aspect ratio is somewhat more indicative of the effects of the ground plane itself.

The full results for the C_P distributions are shown in Appendix B, and a sample set for the three ranges of AR is shown in Figure 4.11. The differences between the thin and thick boundary layers are clearly evident in these figures. Though the same features are seen, they occur at different aspect ratios for the two boundary layers. For the most part, the appearance of the various features in the C_P distributions is delayed to higher aspect ratios within the thicker boundary layer.

For the lowest aspect ratio, AR = 0.5, there are large enclosed regions of low pressure on both the upstream and downstream halves of the free end. The upstream enclosed region represents the minimum measured pressure on the surface, while the downstream region

encapsulates the maximum surface pressure. For AR ≥ 1, which may coincide with the lower critical aspect ratio, the upstream region splits into two identical "eye-like" sites of minimum pressure, and the region on the downstream half shifts towards the trailing edge, eventually opening up and being interrupted by the trailing edge. The maximum pressure region becomes closed once again for AR ≥ 3. This appearance of the mean surface pressure distributions is maintained up to AR ≥ 5, where the eye-like spots increase in size and coalesce into a single band of minimum pressure for AR ≥ 6. Above this value, the magnitudes and distributions of the pressures are relatively unchanged, indicating no change in the flow conditions. This appears to align with the upper critical aspect ratio from the direct force measurements. Within the thicker boundary layer, the formation of the "eye-like" spots is delayed to AR = 3.5, and they persist up to AR = 9, indicating a shift in the range of the critical AR. The eye-like spots are expected to be the terminal ends of the mushroom vortex that forms from the recirculation region, but this explanation does not account for the disappearance of the spots for higher AR when the vortex appears to persist (according to oil film results from Kawamura et al. (1984)).

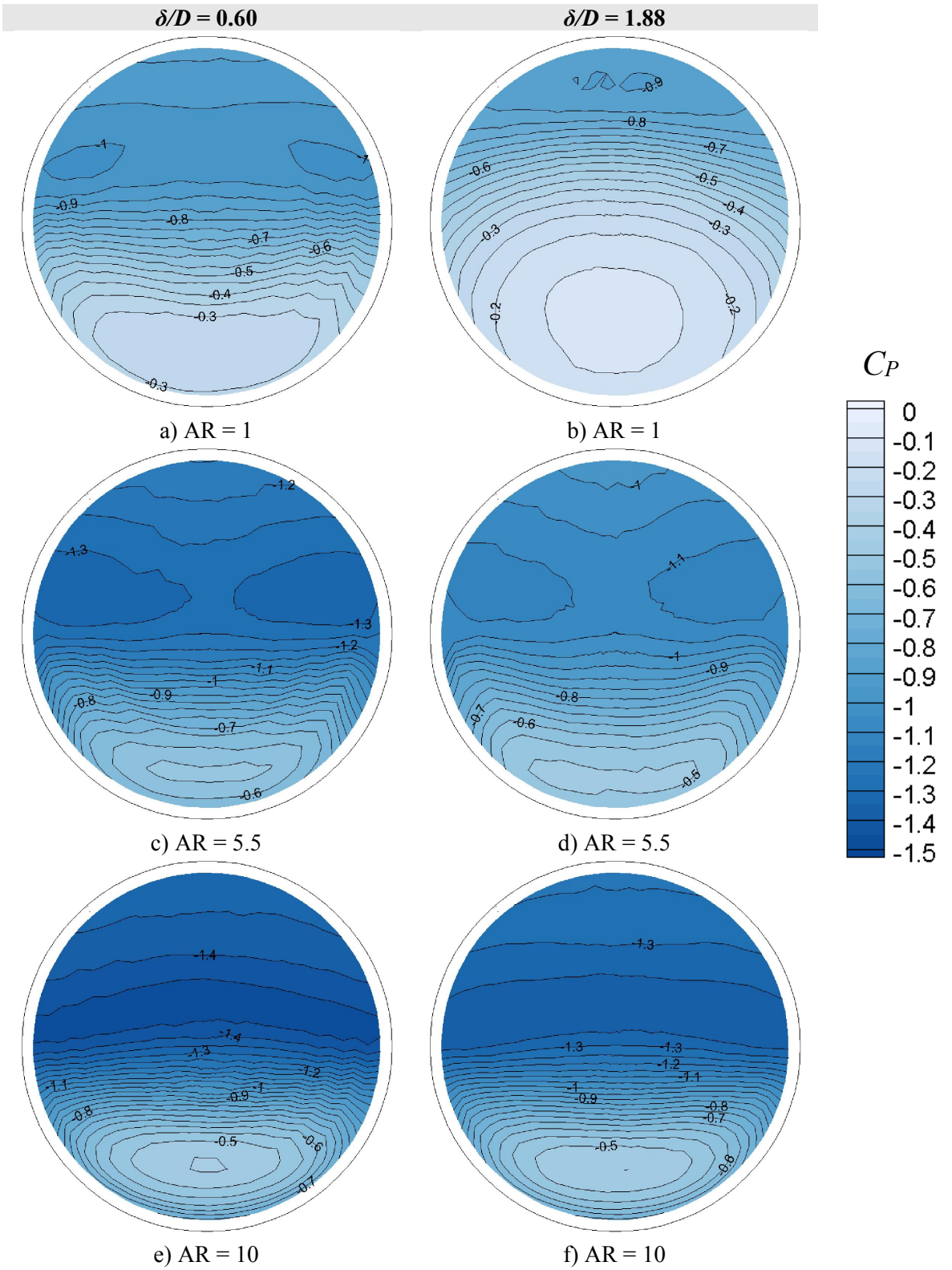

Figure 4.11: Sample free end pressure distributions for a cylinder immersed in a thin and thick boundary layer. One distribution is shown for each range of AR: a) and b) below the lower critical AR, c) and d) between the critical AR, e) and f) above the upper critical AR. Flow is from top to bottom.

The appearance of the enclosed regions can also be seen as peaks and valleys in the profiles for the C_P along the centerline of the free end. The full data set is shown in Appendix C, a sample set of which is shown in Figure 4.12. The profiles show a smooth increase in C_P along the centerline, moving towards the trailing edge of the cylinder. The minimum pressure coefficient is typically reached at x/D = -0.1, while the maximum (least negative) pressure coefficient is generally reached at x/D = 0.4. The strong positive pressure gradient immediately follows the minimum C_P, and continues up to the maximum C_P.

δ/D = 0.60	δ/D = 1.88

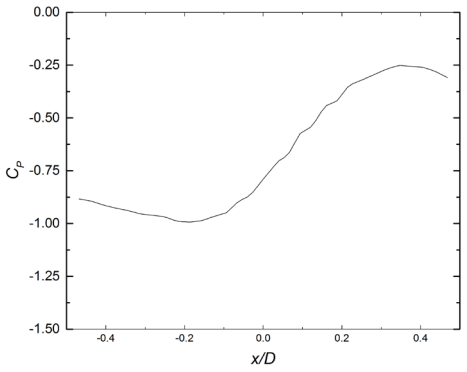

a) AR = 1

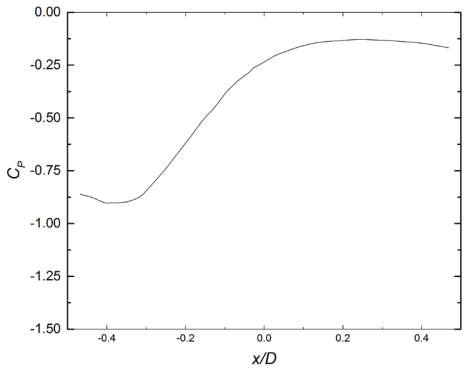

b) AR = 1

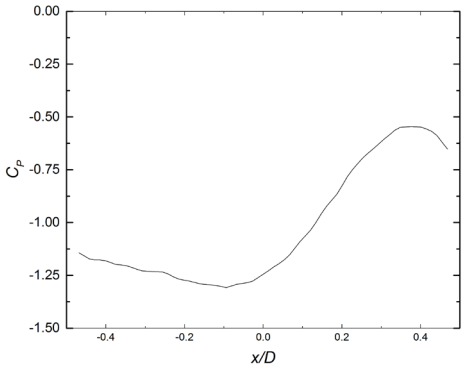

c) AR = 5.5

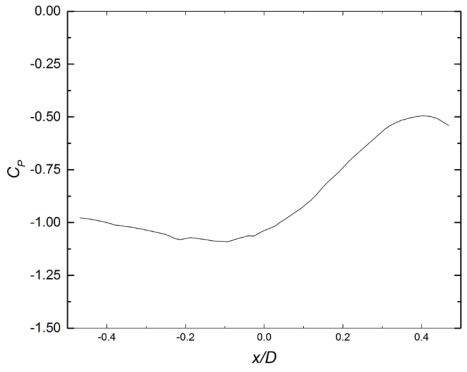

d) AR = 5.5

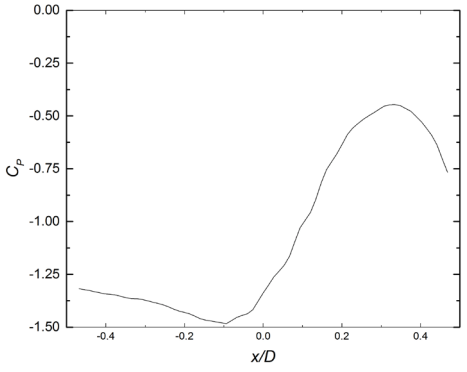

e) AR = 10

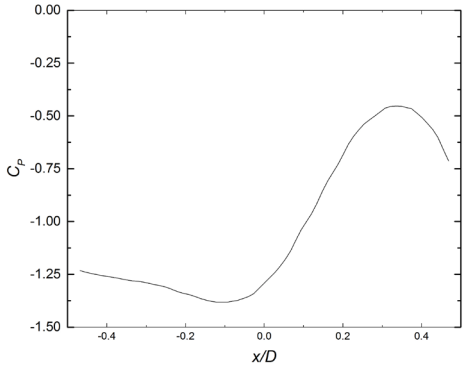

f) AR = 10

Figure 4.12: Sample free end C_P profiles for the streamwise centerline on a cylinder immersed in a thin and thick boundary layer. One profile is shown for each range of AR: a) and b) below the lower critical AR, c) and d) between the critical AR, e) and f) above the upper critical AR. Flow is from left to right.

The minimum pressure coefficient is C_P = -1.4, reached at all values for AR ≥ 6, though the true largest value is reached at AR = 11, but the increase is marginal. The mean pressure coefficient is negative at all points, and is closest to zero within the maximum pressure region seen at low aspect ratios. Figure 4.13 shows a comparison of the largest and smallest pressure coefficients. The maximum pressure coefficient attains a nearly constant value for AR > 6 in both boundary layers, while the minimum pressure coefficient becomes constant for AR > 6 (the upper critical AR) in the thin boundary layer, but is likely delayed slightly above AR = 11 for the thicker boundary layer. This behaviour is consistent with the upper critical aspect ratio, and corresponds with the reduced value of the integrated (based on pressure) normal force coefficient for the cylinder immersed in the thick boundary layer. Near the lower critical aspect ratio, AR = 2.5, there appears to be a change in the C_P slopes, excluding the minimum pressure in the thin boundary layer. The reattachment point of the mean recirculation zone above the free end is sometimes associated with the site of minimum pressure (Tsutsui 2012). The locations of the maximum C_P along the centerline were collected in the current experiments, and were used to determine whether this value corresponds to the reattachment point seen in particle image velocimetry (PIV) measurements used for Sumner et al. (2015). These results will be detailed in future work, but initial results show that there is a correlation between the reattachment length and the location of maximum C_P.

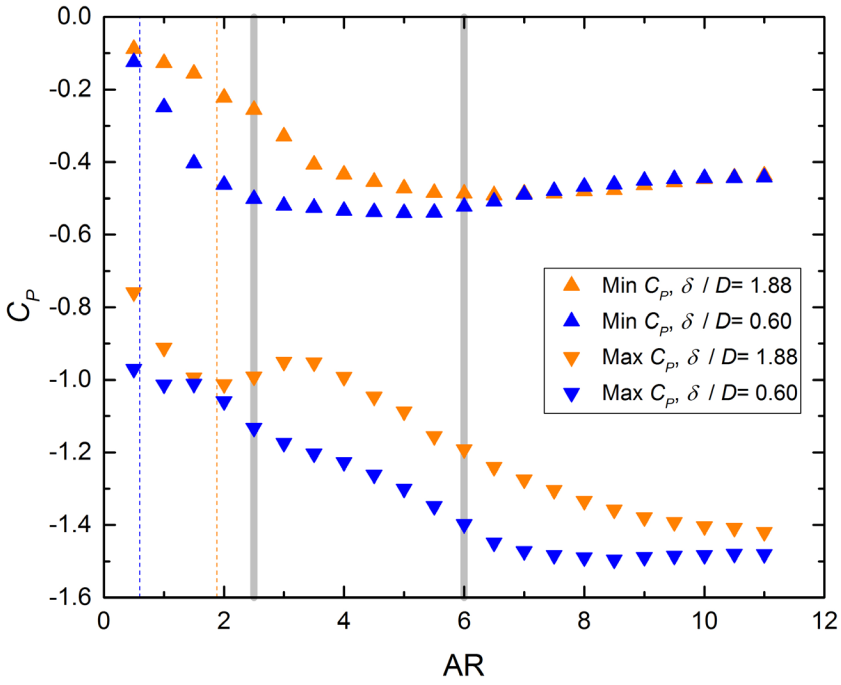

Figure 4.13: Comparison of maximum and minimum mean pressure coefficient on the free end. The respective boundary layer thicknesses are shown as vertical dashed lines of the corresponding colours. The upper and lower critical aspect ratios for the thin boundary layer are shown as thick gray lines at AR = 6 and AR = 2.5, respectively.

Within the thick boundary layer, the same flow features and regions are seen, but changes occur at higher aspect ratios compared to the thin boundary layer. The scenario with enclosed maximum and minimum pressure regions subsists from AR = 0.5 to AR = 2. A band of minimum pressure follows, with the enclosure at the trailing edge opening up to the edge at the same time. The enclosure of maximum pressure is interrupted by the trailing edge for $3 < AR \leq 5$, and is enclosed outside of these AR. The eye-like spots are developed at AR = 3, and subsist until AR = 9. The minimum pressure band returns for AR > 9, and continues until the end of the tested range (AR = 11). At AR = 10.5, the eye-like spots re-appear, but they are small and pushed to the edges. The spots may exist throughout the entire AR range where the band of minimum pressure is seen, but do not vary as strongly from the surrounding pressures.

The differences between the two boundary layer conditions serve to illustrate how the mean static pressure distribution on the free end, and its magnitude, are affected by both the boundary layer thickness and aspect ratio. The force and moment coefficient data indicated the existence of two critical aspect ratios, AR = 2.5, and AR = 6. The pressure results for the thin boundary layer cannot be used to confirm the existence of the lower critical aspect ratio, though some changes are evident. The upper critical aspect ratio, AR = 6, appears to be where the eye-like spots disappear in favor of the band of minimum pressure. However, for the thick boundary layer case, this critical AR would be located at AR = 9, which is not consistent with the force results. This suggests that the normal force coefficient is more sensitive to changes in the flow conditions than solely changes in the free-end surface pressure. The difference between the integrated and measured normal force (Figure 4.1) leads to the conclusion that the wall shear stress also influences the total normal force.

4.8 Free End Pressure Fluctuations

The RMS fluctuations of the surface pressure, $C_P'(r,\Theta)$, were also measured, as the fluctuations may indicate the location of certain flow structures. The pressure fluctuations have not received much attention in the literature, partially due to the difficulty in measuring them accurately when long tubing must be used for the pressure lines in tall cylinders. The pressure fluctuation distributions are shown in Appendix D, and a sample set is shown for the three ranges of AR in Figure 4.14.

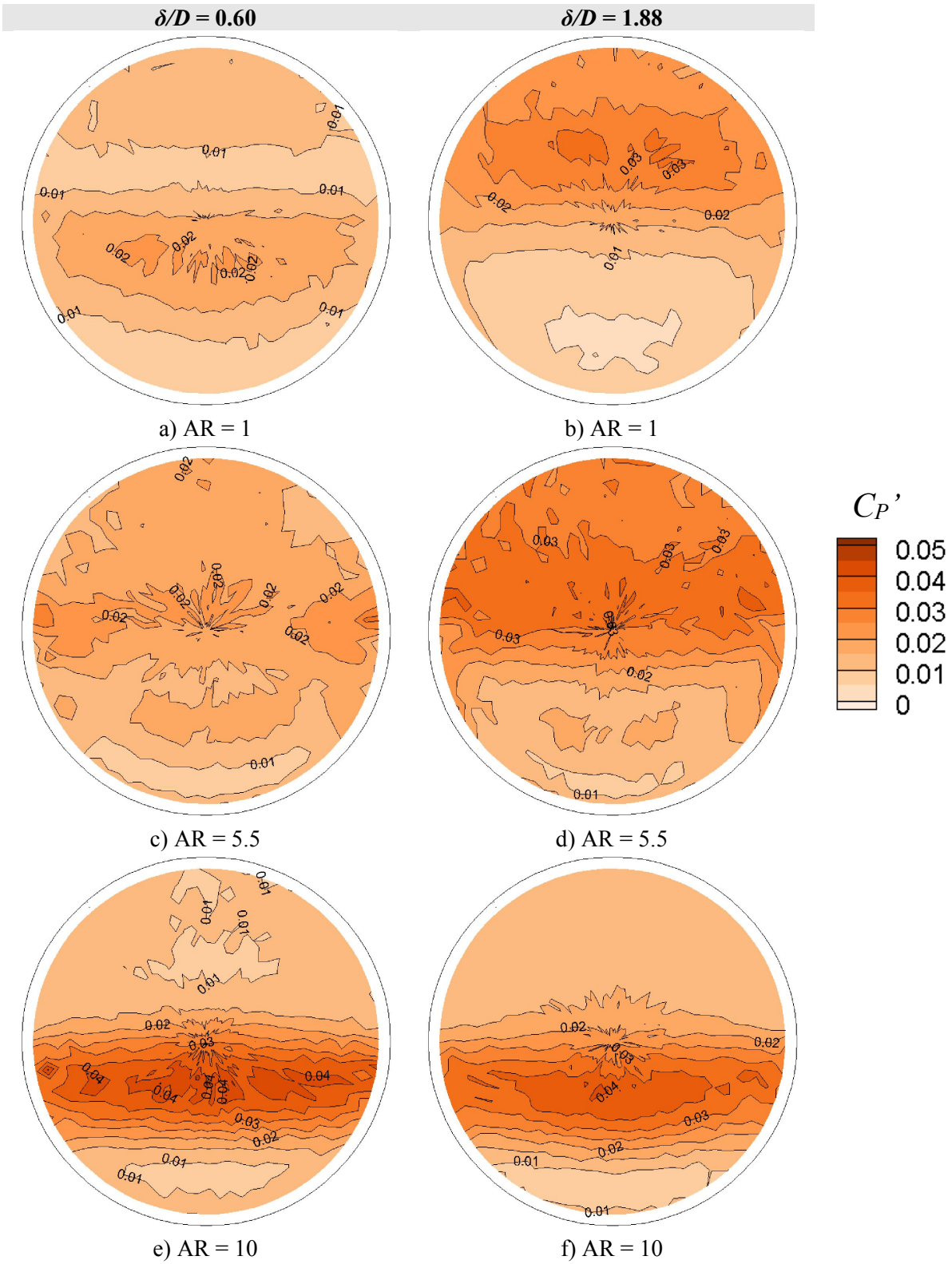

Figure 4.14: Sample free end pressure fluctuation distributions for a cylinder immersed in a thin and thick boundary layer. One distribution is shown for each range of AR: a) and b) below the lower critical AR, c) and d) between the critical AR, e) and f) above the upper critical AR. Flow is from top to bottom.

The most interesting result is the similarity in pressure fluctuations between the two boundary layers. In both conditions, the fluctuations grow large over the entire upstream half of the cylinder between AR = 2.5 and AR = 3, which is consistent with the critical AR found in the force results. For AR < 1, the fluctuations are small and have an enclosed region of minimum fluctuation on the downstream half of the cylinder. The fluctuation magnitude increases and covers the entire upstream half of the free end for the next aspect ratios. Beyond AR = 5 for the thin boundary layer, and AR = 7 for the thick boundary layer, a band of maximum fluctuations develops directly behind the midway point of the cylinder. As this is the region of fairly consistent flow patterns, it is possible that this corresponds to the location of the reattachment line. However, investigation of the location of maximum fluctuations on the centerline did not yield results similar to the reattachment line expected based on PIV measurements by Sumner et al. (2015). The maximum fluctuation line tends to lie upstream of the expected reattachment line, sometimes occurring in the upstream half of the free end, while the reattachment line is typically in the downstream half.

5 Conclusions, Contributions, and Recommendations

5.1 Conclusions

The effects of aspect ratio and boundary layer thickness on the aerodynamic forces and moments for a surface-mounted finite-height cylinder were studied experimentally using a low-speed wind tunnel with a cylinder that could be constructed with incremental increases in height. The mean drag force, mean normal force, and mean bending moment were measured with a force balance, and the free-end surface pressure distribution was measured with a set of pressure taps. The boundary layer velocity profiles and the vortex shedding frequencies were measured using a hot-wire probe. The combination of techniques allowed the mean drag force, and the mean bending moment caused by the drag force, to be obtained through a direct force measurement. The mean normal force is also obtained both through a direct force measurement and by the integration of the free-end surface pressures. The use of an additional small-diameter cylinder and both thin and thick boundary layers allowed the majority of tests to be completed for four relative boundary layer thicknesses.

The results lead to some valuable conclusions, the most significant of which is the existence and location of two critical aspect ratios. The Strouhal number, mean drag coefficient, and mean normal coefficient results showed significant changes occurring near AR = 2.5 and AR = 6, which are called the lower critical aspect ratio and the upper critical aspect ratio, respectively. There was a variance in the critical AR of ± 0.5 between the parameters. The mean drag coefficient increases rapidly with AR for low AR up to AR = 2.5, then maintains a nearly constant value, and then increases linearly for AR ≥ 6. The mean normal coefficient increases for low AR up to a nearly constant value between the two critical aspect ratios, and slowly decreases with AR towards a small constant value for AR > 6. The mean bending moment coefficient and the point of action were seen to change significantly at only the lower critical AR, showing a fairly sudden increase for AR ≤ 2.5. Changes in the appearance of the C_P and C_P' distributions showed the possible existence of two critical AR as well, at values of AR = 1 and AR = 6.

Evidence for the lower critical aspect ratio has been seen in wake measurements of finite square prisms as well (e.g. Sumner et al. (2017)), but the upper critical aspect ratio has not been clearly evident in prior research. The reason for the existence of the two critical aspect ratios is

not confirmed, though it is expected that the lower critical AR is associated with the transition from symmetric to antisymmetric vortex shedding. The upper critical AR has not received much attention in the literature, and requires further work to verify its existence and the associated mechanism behind it.

The critical aspect ratios, along with the flow above the free end, are both affected by changes in δ/D, even for high aspect ratios (AR $\geq$ 7). The critical aspect ratios are generally shifted to higher values within a thicker boundary layer. For the Strouhal number, the lower critical AR is shifted from AR = 2 to AR = 5, while the upper critical AR is shifted from AR = 6 up to AR = 8.5. Similarly, the lower critical AR from the mean drag coefficient is increased from AR = 2.5 to AR = 4, and the upper critical AR is increased from AR = 5.5 to AR = 7. The critical AR for the normal force coefficient is less affected; the lower critical AR remains at AR = 2.5, while the upper critical AR is actually reduced, from AR = 6.5 to AR = 6. The mean bending moment coefficient does not show the upper critical AR clearly, but does show the critical AR being reduced within the thicker boundary layer, from approximately AR = 2.5 to AR = 1. The lower critical AR is again shifted upward for the point of action, from AR = 2.5 to AR = 3.5 with the thicker boundary layer.

The normal force on the cylinder is a small value, reaching a maximum of approximately 20% of the drag force for a given AR. The normal force coefficient approaches, but never reaches, a value of $C_N = 1.0$. The small magnitude of this force may explain why it has not been detected in prior studies. For a large building, however, the normal force, which is produced mainly on the free end, may have a noticeable impact on roof structures. For this reason, it may be negligible in the design of support structures for the entire cylinder (due to the relative magnitude of the mean bending moment), but should not be overlooked in the design and placement of roof structures. The normal force results obtained from integration of the free-end C_P distributions differed from the measured normal force results. The integrated mean normal force coefficient was smaller than the total mean normal force coefficient, but did not reduce for AR > 6, which suggests that a vertical wall shear force has a significant contribution for high AR, where the skin friction acts over a larger surface area. Further tests are required to verify which flow structures are affecting these force measurements.

The mean bending moment coefficient showed that the mean bending moment itself is influenced by factors besides the mean drag force. As the drag is the largest force on a cylinder in cross-flow, it was expected to be the sole influencing parameter on the bending moment at the base of the cylinder. This appears to be true at high AR, but the bending moment coefficient rises for low AR, where the drag is significantly reduced. The reason for this discrepancy may be related to the high point of action that is a result of the velocity profile in the boundary layer, where the cylinder is immersed for these low AR. Because of the boundary layer influence, estimates of the bending moment from the freestream velocity will offer a conservative estimate in most cases, but more attention should be paid to this value for cylinders of small AR, especially short cylindrical buildings.

Changes in the mean pressure distributions and their fluctuations appear to align with the critical aspect ratios seen in the force measurements, while also showing evidence for some flow structures. The new pressure distributions consistently show the "eye-like" structures that were seen in some earlier published studies. While these structures were previously seen for only higher AR, they are seen as low as AR = 1 in the present thesis research. These structures are the sites of minimum surface pressure, and may represent the terminal ends of the mushroom vortex on the free end. Above the upper critical AR, the two sites combine into a single band of minimum pressure, perhaps indicating a change in the structure of the mushroom vortex. As with the force measurements, the critical aspect ratio where this change occurs is pushed to higher AR within the thicker boundary layer. The fluctuations tend to be larger in the upstream half of the cylinder below the upper critical AR, but form a band of maximum fluctuations behind the midpoint of the free end face.

5.2 Contributions of this Work

The major contribution of this work is the confirmation of the existence and location of two critical aspect ratios where the flow conditions are changed as a result of the aspect ratio or boundary layer thickness. The results of this project also include an in-depth view of the effect of aspect ratio on the mean drag force. Existing free end pressure distributions are combined with a set of 44 new pressure distributions over a large AR range with consistent formatting to give the most complete picture of the free-end surface pressures in the literature. It also

produces some of the first known figures introducing values and coefficients for the mean normal force that results from the free-end surface pressure and the mean bending moment that results from the drag force.

5.3 Recommendations

These current tests serve to fill in a significant gap in the knowledge of finite cylinder flow, but in doing so, also inspire more questions that will require further research in future studies. First and foremost is the existence of the normal force. As this is one of the first times this normal force has been extensively studied, further expansion of the concept is necessary in the future. More tests will serve to validate the accuracy and repeatability of the current measurements. The small magnitude of the forces measured in this experiment means that the error is appreciable. A small-scale force balance that measures force in only one direction with great accuracy would strongly aid in the validation of these experiments. The change of C_N with cylinder height should be investigated with a varying boundary layer thickness and a constant AR. This will help determine whether the peaks seen in the data are consistent with only a change in δ/H or whether they are more sensitive to AR. Higher sensitivity to δ/H is indicative of a strong boundary layer influence, while a stronger dependence on AR would indicate that the effect of the ground plane itself is the dominant parameter on finite cylinder flows.

The new results point to two cases where the flow conditions around the cylinder may shift, as evidenced by the changes in force and pressures. PIV or another high resolution flow visualization method should be attempted for cylinders with a similarly small increment in height, to aid in the determination of the flow factors that contribute to changes in the fluid forces. Multiple PIV angles of the flow field on the free-end surface, similar to Sumner et al. (2015) but over a greater AR range, or concentrated at the critical AR, would help to clarify the flow structures that influence the pressure distribution, and verify the existence of the arch vortex and its terminal ends. More research, especially numerical simulations, on the near-wake region would also help to confirm the hypothesis that the downwash flow seen in Krajnović (2011) and Sumner et al. (2015) is responsible for the skin friction that contributes to the total mean normal force.

Practical applications of this information should also be investigated, with tests that would involve measuring the forces on the free end of a large cylinder or a building. Analysis of wind speeds and forces at particular points on the building roof may indicate optimal locations for the placement of air handling units and heat exchangers. To further this understanding, similar tests could be carried out with structures (or roughness) on the free end. There have been comparisons of the effects of parapets and conical or rounded ends, but these studies have not looked at changes in aspect ratio. An interesting continuation of this research would be to complete similar measurements on a stack (a hollow cylinder) and see how the pressure distribution inside the stack is affected by the AR, which may affect the dispersion of particles from the stack. These concepts may have use elsewhere as well, as the pressure is strongly indicative of the heat and mass transfer. The correlation of heat transfer and pressures means that there is motivation to use these data in the design of heat exchangers as well, being that an optimal heat exchanger design could offer maximum heat transfer opportunity in regions of maximum flow, increasing the effectiveness of these components.

6 References

Adaramola, M.S., D. Sumner, and D.J. Bergstrom. 2010. "Effect of velocity ratio on the streamwise vortex structures in the wake of a stack." *Journal of Fluids and Structures* 26: 1-18.

Adaramola, M.S., O.G. Akinlade, D. Sumner, D.J. Bergstrom, and A.J. Schenstead. 2006. "Turbulent wake of a finite circular cylinder of small aspect ratio." *Journal of Fluids and Structures* 22: 919-928.

Baker, C.J. 1979. "The laminar horseshoe vortex." *Journal of Fluid Mechanics* 95: 347-368.

Baker, C.J. 1980. "The turbulent horseshoe vortex." *Journal of Wind Engineering and Industrial Aerodynamics* 6: 9-23.

Blevins, R.D. 1990. *Flow Induced Vibration.* Malabar, Florida: Kreiger Publishing Company.

Bourgeois, J.A., P. Sattari, and R.J. Martinuzzi. 2011. "Alternating half-loop shedding in the turbulent wake of a finite surface-mounted square cylinder with a thin boundary layer." *Physics of Fluids* 23: 095101, 15 pp.

Chen, S.B., S. Sanitjai, K. Ghosh, and R.J. Goldstein. 2012. "Three-dimensional vortex flow near the endwall of a short cylinder in crossflow: Uniform diameter circular cylinder." *Applied Thermal Engineering* 49: 73-78.

Chue, S.H. 1975. "Pressure probes for fluid measurement." *Progress in Aerospace Sciences* 16 (2): 147-223.

Coutanceau, M., and J. Defaye. 1991. "Circular cylinder wake configurations: a flow visualization survey." *Applied Mechanics Reviews* 44: 255-305.

Dobriloff, C., and W. Nitsche. 2009. "Surface pressure and wall shear stress measurements on a wall mounted cylinder." *Imaging Measurement Methods* NNFM 106: 197-206.

Einian, M., D.J. Bergstrom, and D. Sumner. 2010. "Numerical simulation of the flow around a surface-mounted square cylinder." *Proceedings of the ASME 2010 3rd Joint US-European Fluids Engineering Summer Meeting and 8th International Conference on*

Nanochannels, Microchannels, and Minichannels (FEDSM2010-ICNMM2010). August 1-5, 2010. Montreal, QC, Canada. Paper No. FEDSM-ICNMM2010-30394. 8 pp.

ESDU. 1978. *ESDU 71016: Fluid forces, pressures and moments on rectangular blocks.*

ESDU. 1981. *ESDU 81017 Mean forces, pressures and moments for circular cylindrical structures: finite-length cylinders in uniform and shear flow.* ESDU International plc.

Farivar, D. 1981. "Turbulent uniform flow around cylinders of finite length." *AIAA Journal* 19: 275-281.

Fox, T.A., and G.S. West. 1993. "Fluid induced loading of cantilevered circular cylinders in a low-turbulence uniform flow. Part 1: mean loading with aspect ratios in the range 4 to 30." *Journal of Fluids and Structures* 7: 1-14.

Frederich, O., E. Wassen, F. Thiele, M. Jensch, M. Brede, F. Huttmann, and A. Leder. 2007. "Numerical Simulation of the flow around a finite cylinder with ground plate in comparison to experimental measurements." *Notes on Numerical Fluid Mechanics and Multidisciplinary Design* (Springer-Verlag) 96: 348-355.

Gottingen. 1923. "Ergebnisse der aerodynamischen Versuchsanstalt zu (in German)." *Gottingen* 28-34. As referenced in Goldstein, S., ed. 1965. *Modern Developments in Fluid Dynamics.* Vol. 2. New York: Dover Publications Inc.

Hain, R., C. Kähler, and D. Michaelis. 2008. "Tomographic and time resolved PIV measurements on a finite cylinder mounted on a flat plate." *Experiments in Fluids* 45: 715-724.

Hiwada, M., T. Kawamura, T. Hibino, I. Mabuchi, and M. Kumada. 1984. "Heat transfer from a finite circular cylinder on a flat plate: in the case of cylinder length larger than the turbulent boundary layer thickness." *Transactions of the JSME* 50: 733-742. (in Japanese).

Holman, J.P. 2001. *Experimental methods for engineers.* 7th. Singapore: McGraw-Hill.

Holmes, J.D. 2001. *Wind Loading of Structures.* New York: Taylor & Francis.

Holscher, N., and H.J. Niemann. 1996. "Turbulence and separation induced pressure fluctuations on a finite circular cylinder - application of a linear unsteady strip theory." *Journal of Wind Engineering* 65: 335-346.

Kawamura, T., M. Hiwada, T. Hibino, I. Mabuchi, and M. Kumada. 1984. "Flow around a finite circular cylinder on a flat plate. Cylinder height greater than turbulent boundary layer thickness." *Bulletin of the JSME* 27: 2142-2151.

Krajnović, S. 2011. "Flow around a tall finite cylinder explored by large eddy simulation." *Journal of Fluid Mechanics* 676: 294-317.

Majumdar, S., and W. Rodi. 1989. "Three-dimensional computation of flow past cylindrical structures and model cooling towers." *Building and Environment* 24: 3-22.

McClean, J.F., and D. Sumner. 2014. "An experimental investigation of aspect ratio and incidence angle effects for the flow around surface-mountes finite-height square prisms." *Transactions of the ASME: Journal of Fluids Engineering* 136 (081206): 10 pp.

Ogunremi, Ayodele, and David Sumner. 2015. "On the effects of incidence angle on the mean wake of a surface-mounted finite height square prism." *Proceedings of the ASME-JSME-KSME Joint Fluids Engineering Conference 2015.* Seoul, Korea: ASME. AJK2015-15011, 9 pp.

Okamoto, S. 1991. "Flow past circular cylinder of finite length placed on ground plane." *Transactions of the Japan Society for Aeronautical and Space Sciences* 33 (102): 234-246.

Okamoto, S., and Y. Sunabashiri. 1992. "Vortex shedding from a circular cylinder of finite length placed on a ground plane." *Transactions of the ASME: Journal of Fluids Engineering* 114: 512-521.

Okamoto, T., and M. Yagita. 1973. "The experimental investigation on the flow past a circular cylinder of finite length placed normal to the plane surface in a uniform stream." *Bulletin of the JSME* 16: 805-814.

Ozmen, Y. and Aksu, E. 2017. "Wind pressures on different roof shapes of a finite height circular cylinder." *Wind and Structures* 24 (1): 25-41.

Ozmen, Y. 2013. "Effect of parapets to pressure distribution on flat top of a finite cylinder." *Wind and Structures* 17 (5): 465-477.

Park, C.W., and S.J. Lee. 2004. "Effects of free end corner shape on flow structure around a finite cylinder." *Journal of Fluids and Structures* 19: 141-158.

Pattenden, R.J., N.W. Bressloff, S.R. Turnock, and X. Zhang. 2006. "Unsteady simulations of the flow around a short surface-mounted cylinder." *Numerical Methods in Fluids* 53: 895-914.

Pattenden, R.J., S.R. Turnock, and X. Zhang. 2005. "Measurements of the flow over a low-aspect-ratio cylinder mounted on a ground plane." *Experiments in Fluids* 39: 10-21.

Porteous, R., D.J. Moreau, and C.J. Doolan. 2014. "A review of flow induced noise from finite wall-mounted cylinders." *Journal of Fluids and Structures* 51: 240-254.

Purdy, D.M., F.J. Maher, and D. Frederick. 1967. "Model studies of wind loads on flat-top cylinders." *Proceedings of the American Society of Civil Engineers, Journal of the Structural Division* 93: 379-395.

Rinoshika, H., A. Rinoshika, and S. Fujimoto. 2017. "Passive control on flow structure around a wall-mounted low aspect ratio circular cylinder by using an inclined hole." *Bulletin of the JSME: Journal of Fluid Science and Technology* 12 (1): 1-13.

Rödiger, T., H. Knauss, U. Gaisbauer, and E. Krämer. 2007. *New Research in Numerical and Experimental Fluid Mechanics VI* NNFM 96: 121-128.

Roh, S.C., and S.O. Park. 2001. "Surface flow pattern and local mass transfer on the free-end surface of a finite circular cylinder." *Heat and Mass Transfer* 38: 1-5.

Roh, S.C., and S.O. Park. 2003. "Vortical Flow over the free end surface of a finite circular cylinder mounted on a flat plate." *Experiments in Fluids* 34: 63-67.

Rostamy, N., D. Sumner, D.J. Bergstrom, and J.D. Bugg. 2013. "Instantaneous flow field above the free end of finite-height cylinders and prisms." *International Journal of Heat and Fluid Flow* 43: 120-128.

Rostamy, N., D. Sumner, D.J. Bergstrom, and J.D. Bugg. 2012. "Local flow field of a surface-mounted finite circular cylinder." *Journal of Fluids and Structures* 34: 105-122.

Sakamoto, H., and S. Oiwake. 1984. "Fluctuating force on a rectangular prism and a circular cylinder placed vertically in a turbulent boundary layer." *Transactions of the ASME: Journal of Fluids Engineering* 106: 160-166.

Sarode, R.S., S.L. Gai, and C.K. Ramesh. 1981. "Flow around circular- and square-section models of finite height in a turbulent shear flow." *Journal of Wind Engineering and Industrial Aerodynamics* 8: 223-230.

Sparrow, E.M., and F. Samie. 1981. "Measured heat transfer coefficients at an adjacent to the tip of a wall-attached cylinder in crossflow- application to fins." *Transactions of the ASME: Journal of Heat Transfer* 103: 778-784.

Sumer, B.M., and J. Fredsoe. 1997. *Hydrodynamics Around Cylindrical Structures*. Advanced Series on Ocean Engineering. Vol. 12. Singapore: World Scientific.

Sumner, D. 2013. "Flow above the free end of a surface-mounted finite-height circular cylinder: A review." *Journal of Fluids and Structures* 43: 41-63.

Sumner, D., J.L. Heseltine, and O.J.P. Dansereau. 2004. "Wake Structure of a finite circular cylinder of small aspect ratio." *Experiments in Fluids* 37: 720-730.

Sumner, D., N. Rostamy, D.J. Bergstrom, and J.D. Bugg. 2015. "Influence of aspect ratio on the flow above the free end of a surface-mounted finite cylinder." *International Journal of Heat and Fluid Flow* 56: 290-304.

Sumner, D., N. Rostamy, D.J. Bergstrom, and J.D. Bugg. 2017. "Influence of aspect ratio on the mean flow field of a surface-mounted finite-height square prism." *International Journal of Heat and Fluid Flow* 65: 1-20.

Tanaka, S., and S. Murata. 1999. "An investigation of the wake structure and aerodynamic characteristics of a finite circular cylinder (Time-averaged wake structures behind circular cylinders with various aspect ratios)." *JSME International Journal, Series B* 42: 178-187.

Taniguchi, S., H. Sakamoto, and M. Arie. 1981. "Flow around circular cylinders of finite height placed vertically in turbulent boundary layers." *Bulletin of the JSME* 24: 37-44.

Tsutsui, T. 2012. "Flow around a cylindrical structure mounted in a plane turbulent boundary layer." *Journal of Wind Engineering and Industrial Aerodynamics* 104-106: 239-247.

Tsutsui, T., T. Igarashi, and H. Nakamura. 2000. "Fluid flow and heat transfer around a cylindrical protuberance mounted on a flat plate boundary layer." *JSME International Journal Series B* 43: 279-287.

Uematsu, Y., and C.M. Koo. 2008. "Wind-tunnel study of wind loads on circular cylindrical structures." *Journal of Wind Engineering* 33: 17-25. (in Japanese).

Uematsu, Y., and M. Yamada. 1995. "Effects of aspect ratio and surface roughness on the time-averaged aerodynamic forces on cantilevered circular cylinders at high Reynolds numbers." *Journal of Wind Engineering and Industrial Aerodynamics* 54/55: 301-312.

Uematsu, Y., M. Yamada, and K. Ishii. 1990. "Some effects of free-stream turbulence on the flow past a cantilevered circular cylinder." *Journal of Wind Engineering and Industrial Aerodynamics* 33: 43-52.

Uematsu, Y., T. Moteki, and T. Hongo. 2008. "Model of wind pressure field on circular flat roofs and its application to load estimation." *Journal of Wind Engineering and Industrial Aerodynamics* 96: 1003-1014.

Vandiver, J. Kim. 1983. "Drag coefficients of long flexible cylinders." *Proceedings of the 1983 Offshore Technology Conference.* May 2-5. Houston, TX, United States. Paper No. 4490. 405-410.

Vickery, B.J. 1968. "Load fluctuations in turbulent flow." *Proceedings of the American Society of Civil Engineers, Journal of the Engineering Mechanics Division* 94: 31-46.

Wang, H.F., and Y. Zhou. 2009. "The finite-length square cylinder near wake." *Journal of Fluid Mechanics* 638: 453-490.

Wang, H.F., Y. Zhou, and J. Mi. 2012. "Effects of aspect ratio on the drag of a wall mounted finite-length cylinder in subcritical and critical regimes." *Experiments in Fluids* 53: 523-436.

Wang, H.F., Y. Zhou, C.K. Chan, and K.S. Lam. 2006. "Effect of initial conditions on interaction between a boundary layer and a wall-mounted finite-length-cylinder wake." *Physics of Fluids* 18: 065106, 12pp.

White, F.M. 2003. *Fluid Mechanics.* 5th Edition. New York: McGraw-Hill.

Williamson, C.H.K. 1996. "Vortex dynamics in the cylinder wake." *Annual Review of Fluid Mechanics* 28: 477-539.

Yoshida, M., and T. Hongo. 1983. "Experimental study of wind forces on buildings, Part 3: Wind tunnel study of wind forces on flat roofs with long span." *Annual Report of Kajima Institute of Construction Technology* 31: 119-126. (in Japanese).

Zdravkovich, M.M. 1997. *Flow around Circular Cylinders. Vol. 1: Fundamentals*. Oxford: Oxford University Press.

Appendix A – Published Pressure Distributions

This Appendix contains the pressure distributions that were collected from published sources, then digitized and replotted with consistent formatting for comparison and use in integration. The distributions are arranged in order of increasing boundary layer thickness, δ/D.

Table A.1: Published surface pressure distributions for the free end of a surface-mounted finite-height cylinder. Flow is from top to bottom. The "volume" is the calculated value for C_N.

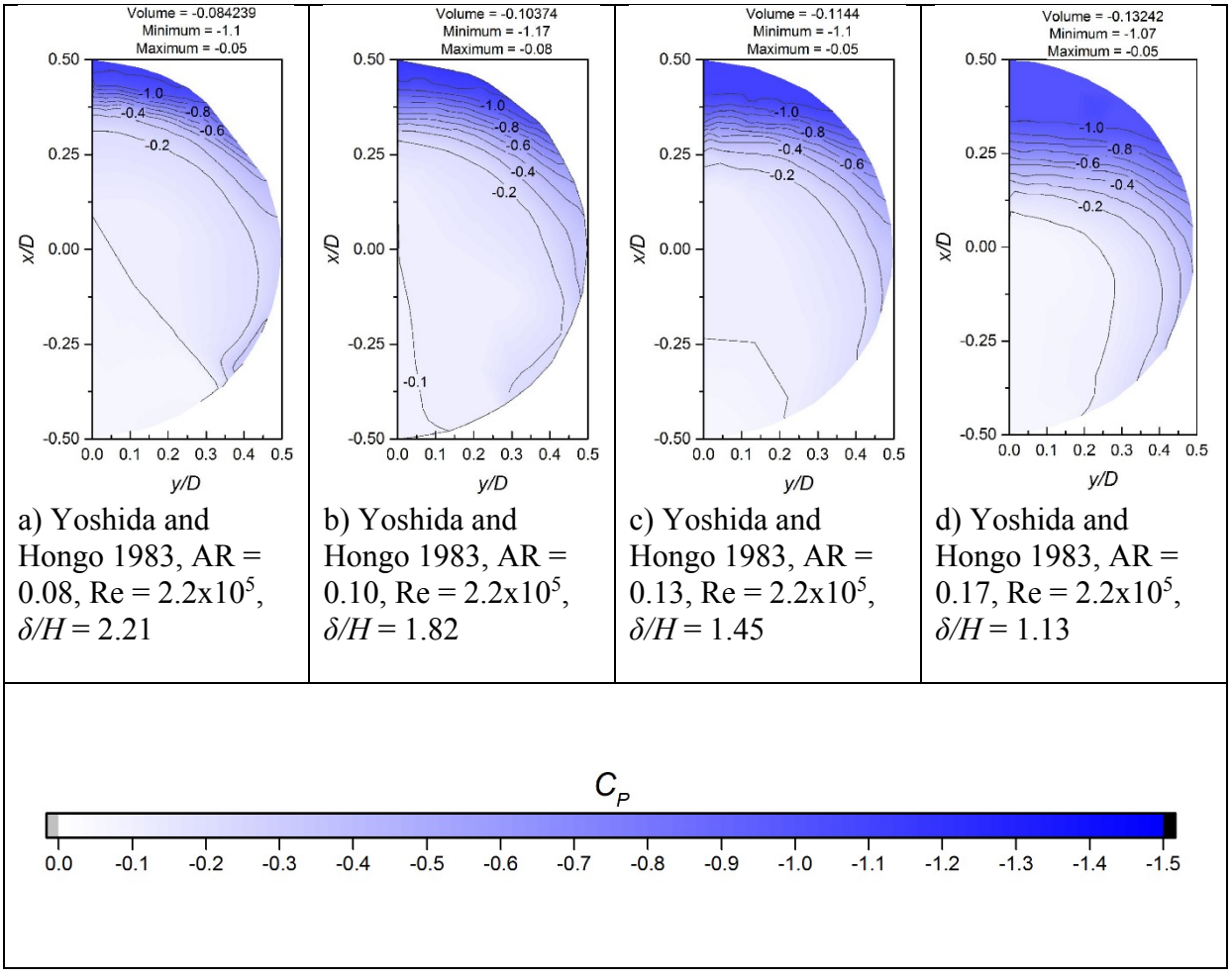

a) Yoshida and Hongo 1983, AR = 0.08, Re = 2.2×10^5, $\delta/H = 2.21$

b) Yoshida and Hongo 1983, AR = 0.10, Re = 2.2×10^5, $\delta/H = 1.82$

c) Yoshida and Hongo 1983, AR = 0.13, Re = 2.2×10^5, $\delta/H = 1.45$

d) Yoshida and Hongo 1983, AR = 0.17, Re = 2.2×10^5, $\delta/H = 1.13$

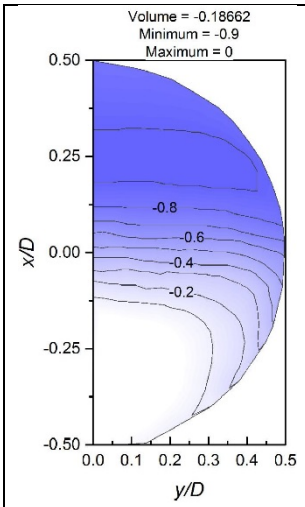

e) Yoshida and Hongo 1983, AR = 0.25, Re = 2.2×10^5, $\delta/H = 0.76$

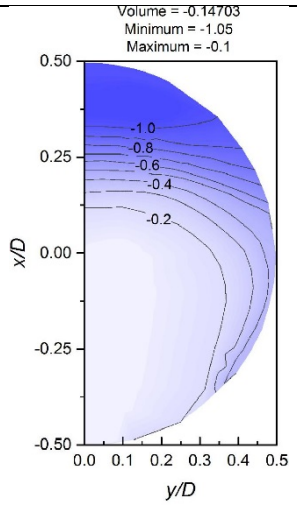

f) Purdy 1967, AR = 0.25 (Plywood), Re = 9.8×10^5, $\delta/H = 1$

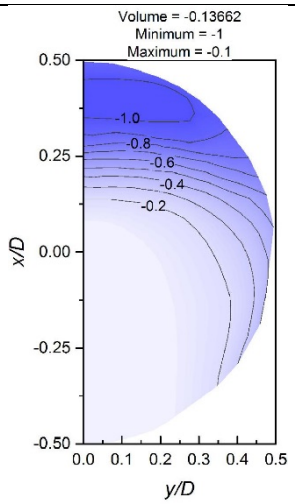

g) Purdy 1967, AR = 0.25 (Plexiglass), Re = 9.8×10^5, $\delta/H = 1$

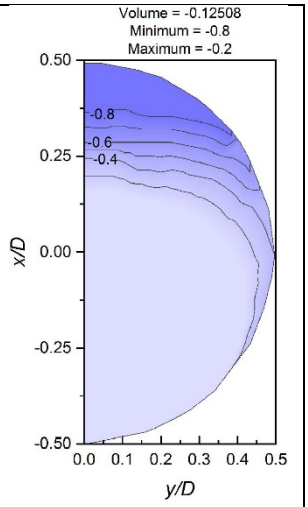

h) Tsutsui 2012, AR = 0.25, Re = 1×10^5, $\delta/H = 2.6$

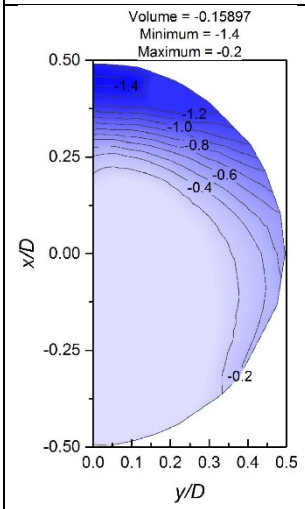

i) Uemastu, Moteki and Hongo 2008, AR = 0.25, Re = 1×10^5, δ/H not given

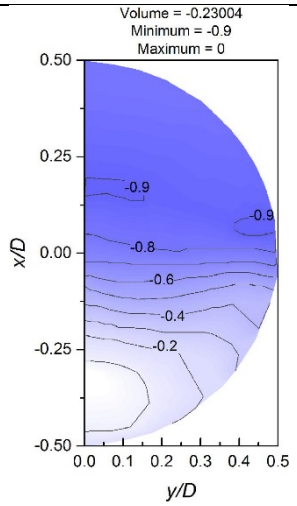

j) Yoshida and Hongo 1983, AR = 0.33, Re = 2.2×10^5, $\delta/H = 0.56$

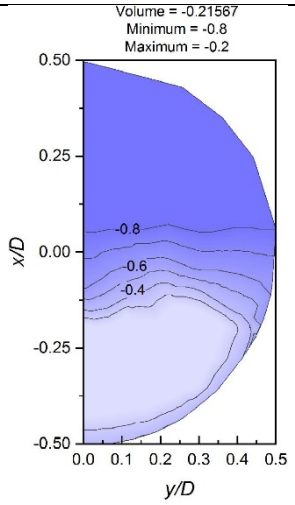

k) Tsutsui 2000, AR = 0.35 laminar, Re = 8.4×10^4, $\delta/H = 0.09$

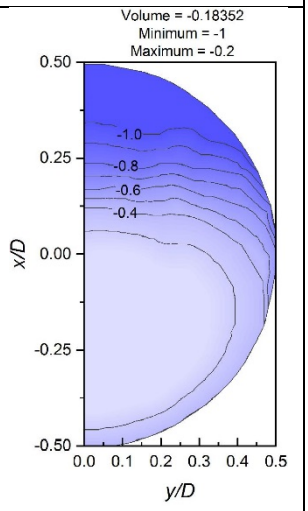

l) Tsutsui 2000, AR = 0.35 Turbulent, Re = 8.4×10^4, $\delta/H = 0.59$

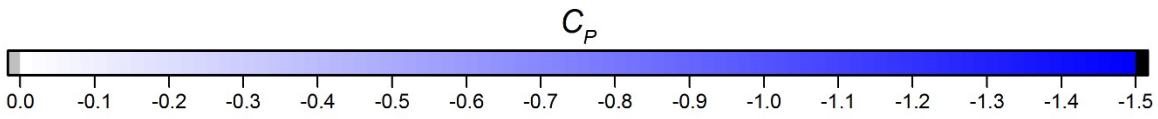

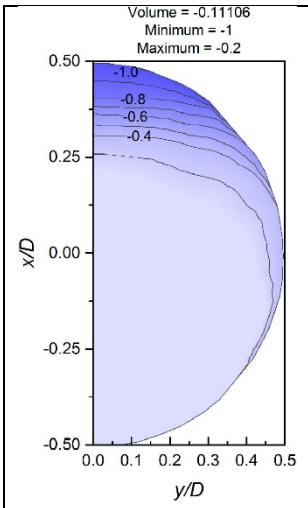

m) Tsutsui 2000, AR = 0.35 Turbulent 2, Re = 8.4×10^4, δ/H = 1.16

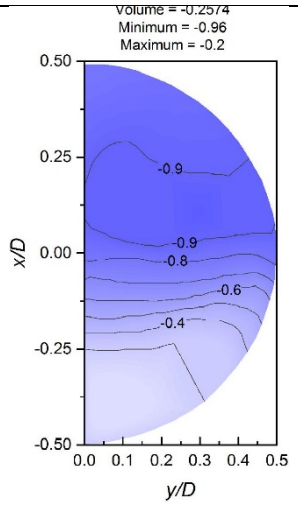

n) Yoshida and Hongo 1983, AR = 0.50, Re = 2.2×10^5, δ/H = 0.38

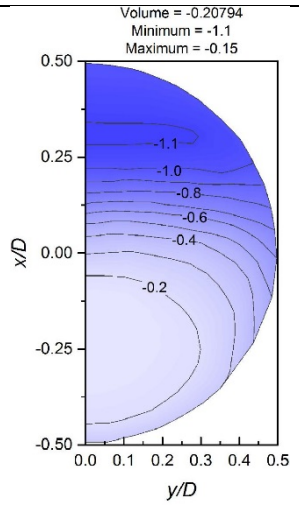

o) Purdy 1967, AR = 0.5, Re = 9.8×10^5, δ/H = 1

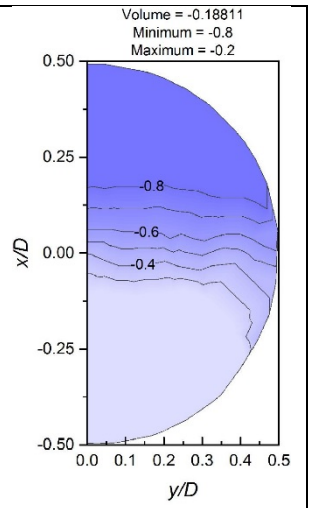

p) Tsutsui 2012, AR = 0.5, Re = 1×10^5, δ/H = 1.3

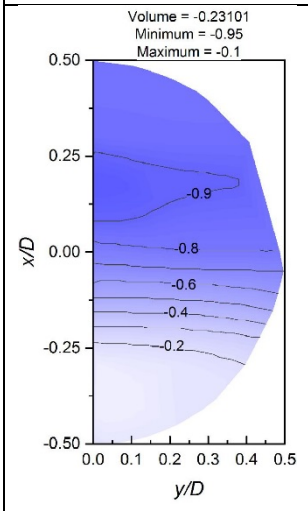

q) ESDU 1981, AR = 0.5, Re = 1×10^6, δ/H not given

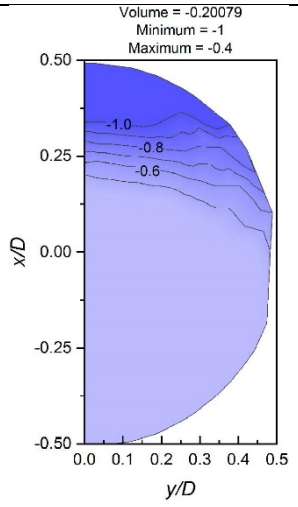

r) Uemastu and Koo 2008, AR = 0.5, Re = 1×10^5, δ/H not given

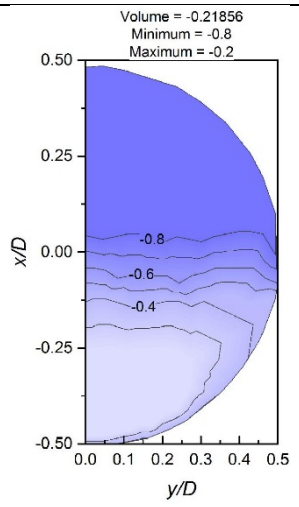

s) Tsutsui 2012, AR = 0.75, Re = 1.1×10^5, δ/H = 0.87

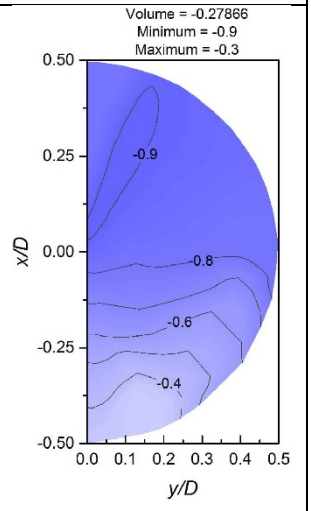

t) Yoshida and Hongo 1983, AR = 1, Re = 2.2×10^5, δ/H = 0.19

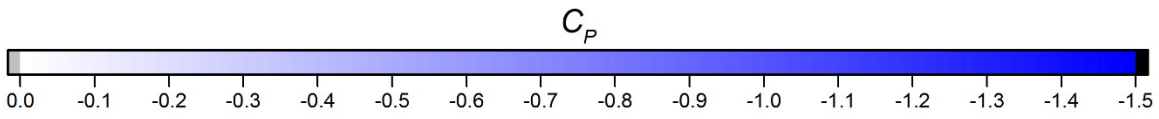

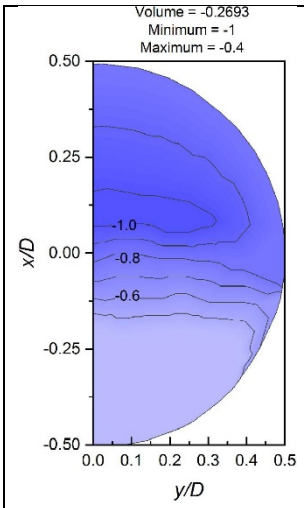

u) Tsutsui 2012, AR = 1, Re = $1x10^5$, δ/H = 0.325

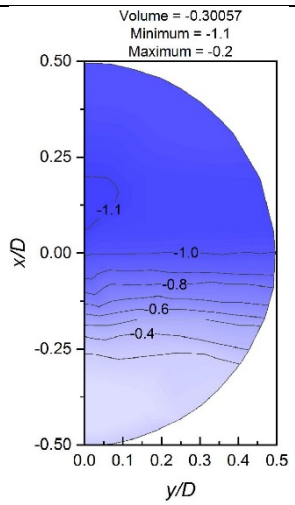

v) Purdy 1967, AR = 1, Re = $9.8x10^5$, δ/H = 0.5

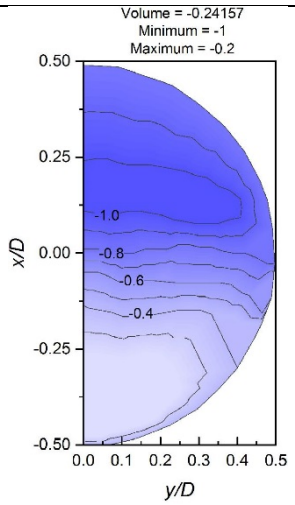

w) Tsutsui 2012, AR = 1, Re = $1x10^5$, δ/H = 0.65

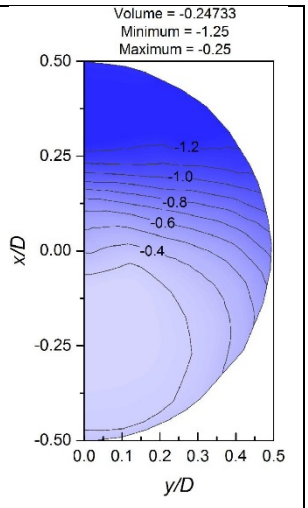

x) Ozmen 2013, AR = 1, Re = $1.50x10^5$, δ/H = 1

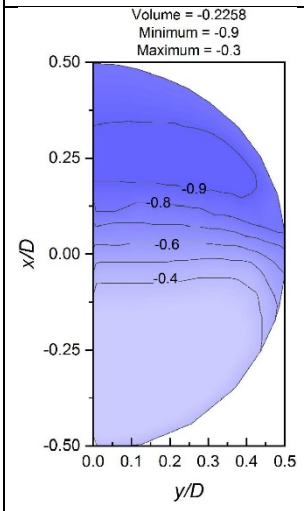

y) Hiwada et al. 1984, AR = 1, Re = $3.2x10^4$, δ/H = 1

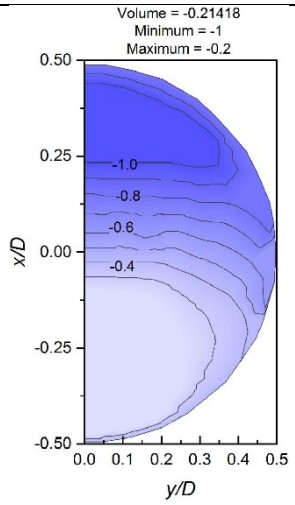

z) Tsutsui 2012, AR = 1, Re = $1x10^5$, δ/H = 1.5

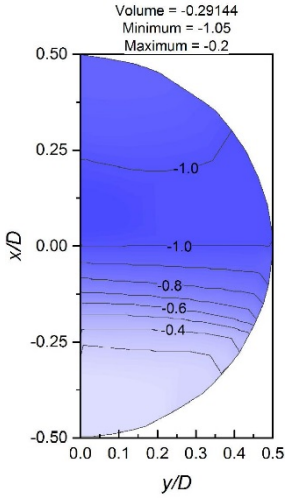

aa) ESDU 1981, AR = 1, Re = $1x10^6$, δ/H not given

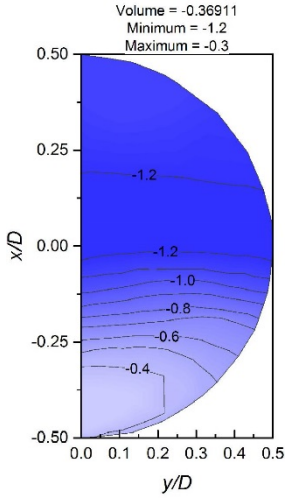

ab) Purdy 1967, AR = 1.25, Re = $9.8x10^5$, δ/H suppressed

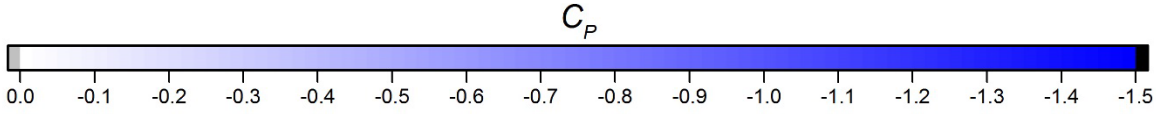

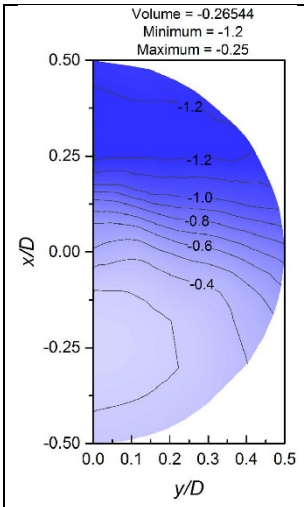

ac) Ozmen and Aksu 2017, AR = 1.5, Re = $1x10^5$, $\delta/H = 1$

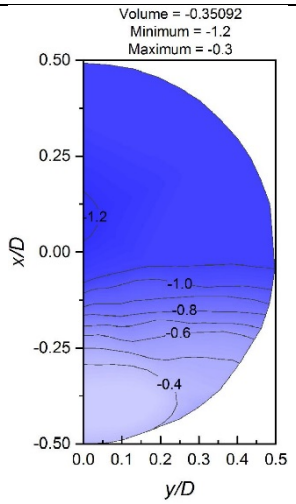

ad) Purdy 1967, AR = 1.5, Re = $9.8x10^5$, $\delta/H = 0.333$

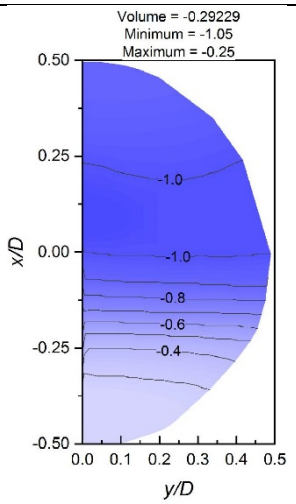

ae) ESDU 1981, AR = 1.5, Re = $1x10^6$, δ/H not given

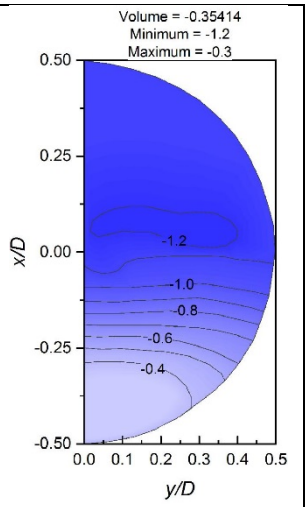

af) Purdy 1967, AR = 1.75, Re = $9.8x10^5$, $\delta/H = 0.286$

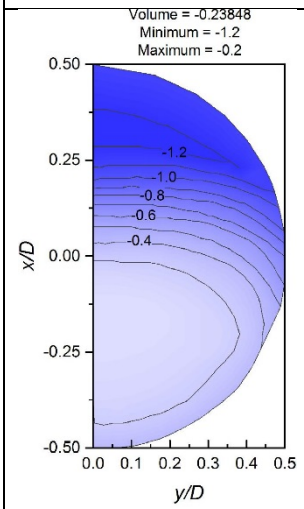

ag) Majumdar and Rodi 1989, AR = 1.9, Re = $5x10^5$, $\delta/H = 2$

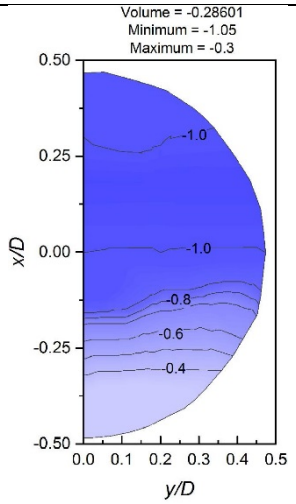

ah) Rodiger et al. 2007, AR = 2, Re = $2x10^5$, $\delta/H = 0.092$

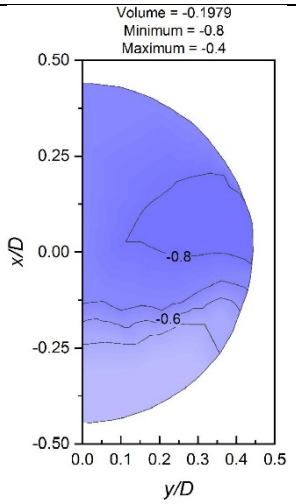

ai) Dobriloff and Nitsche 2009, AR = 2, Re = $2x10^5$, δ/H not given

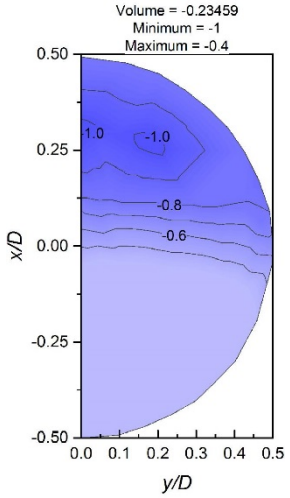

aj) Uemastu and Koo 2008, AR = 3, Re = $1x10^5$, δ/H not given

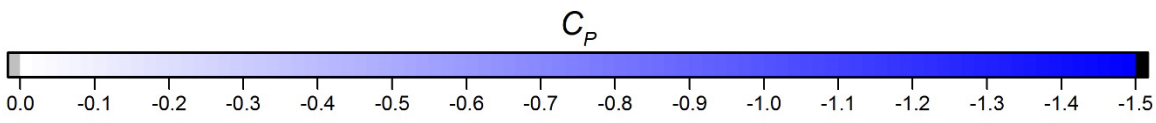

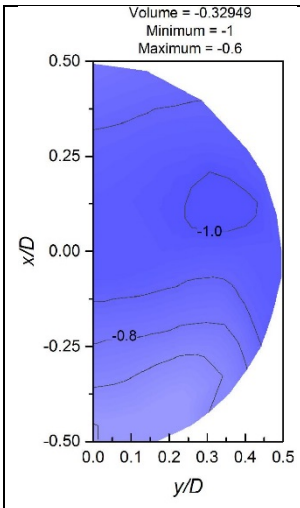

ak) Hiwada et al. 1984, AR = 4, Re = 3.2×10^4, $\delta/H = 0.25$

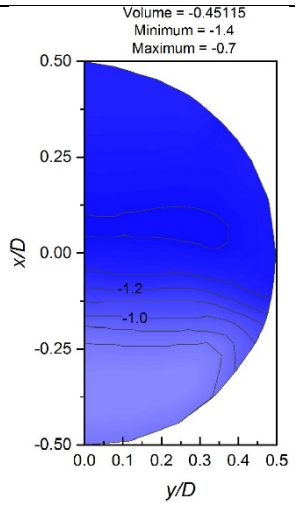

al) Kawamura et al. 1984, AR = 8, Re = 3.2×10^4, $\delta/H = 0.125$

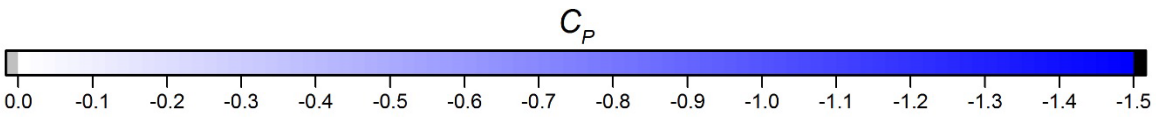

Appendix B – Free end Surface Pressure Distributions

This appendix contains the pressure distributions that were obtained for the free end of the thick cylinder. The pressure coefficient, C_P, is shown both with a color map and contours.

Table B.1: Surface Pressure Distributions for the free end of a surface-mounted finite-height cylinder of varying AR immersed in a thin and a thick boundary layer. Re = 6.5×10^4. Flow is from top to bottom.

***δ/D* = 0.60**	***δ/D* = 1.88**	
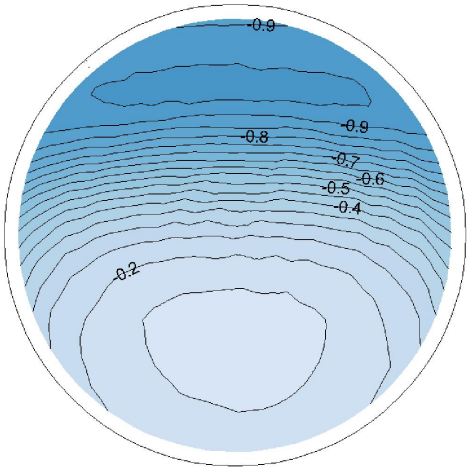 AR = 0.5	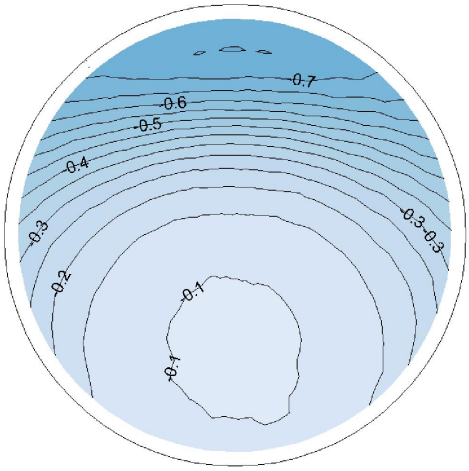 AR = 0.5	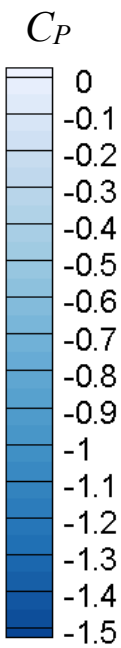
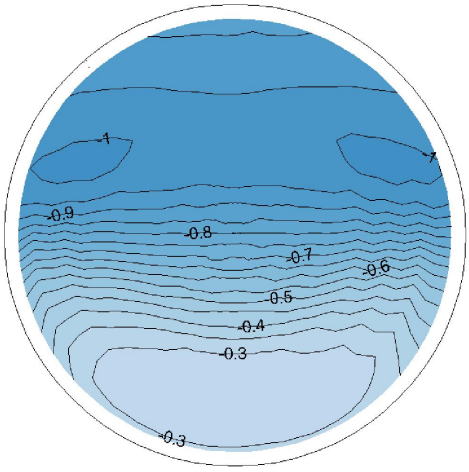 AR = 1	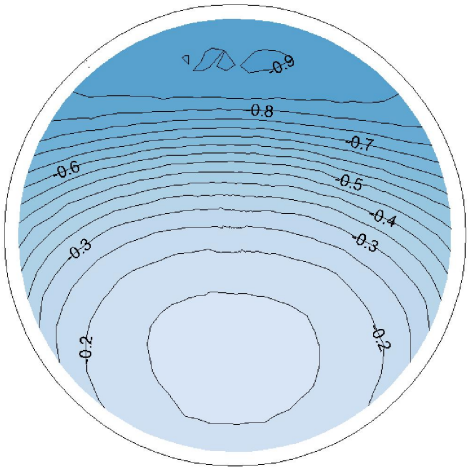 AR = 1	

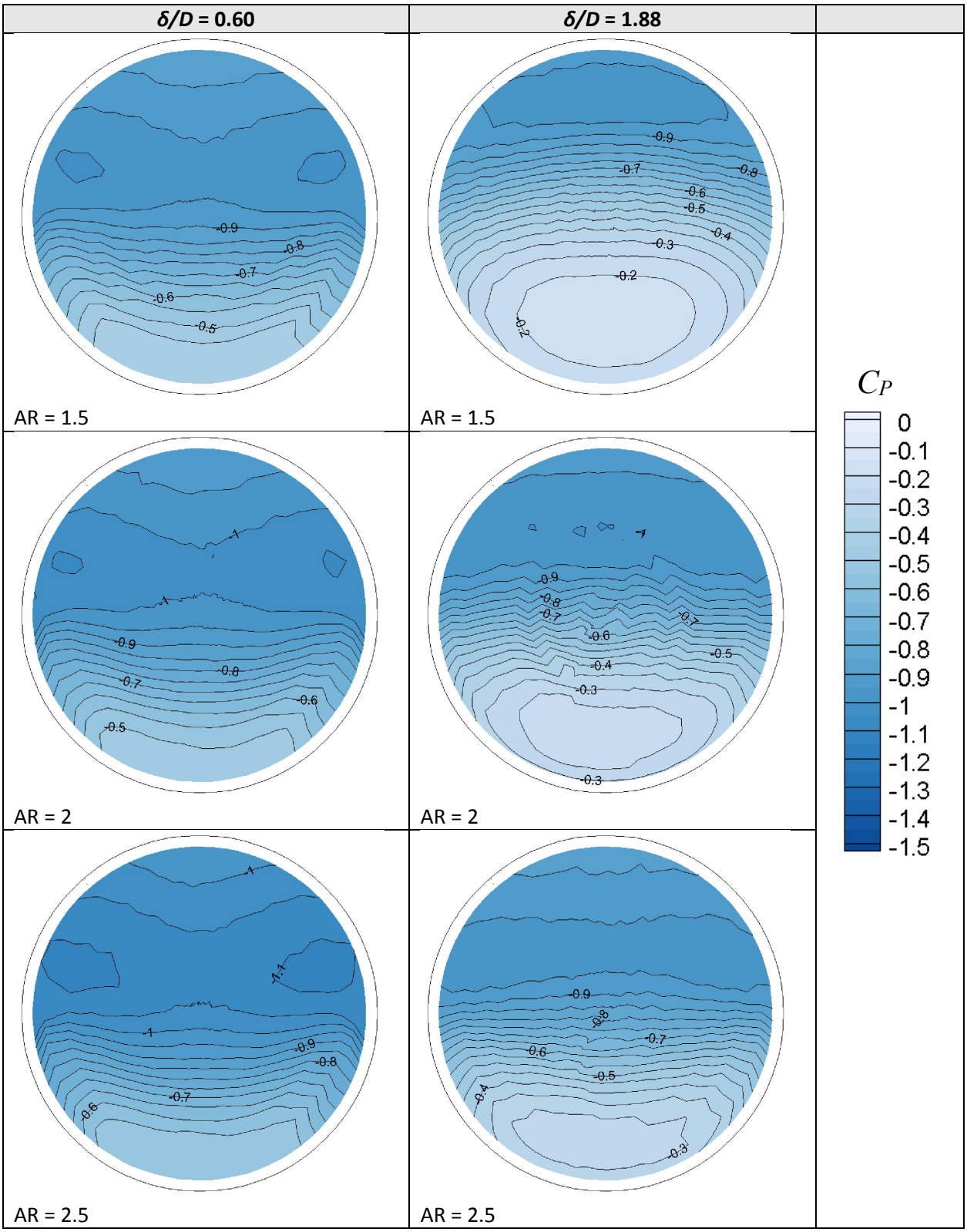
δ/D = 0.60
δ/D = 1.88
AR = 1.5
AR = 1.5
AR = 2
AR = 2
AR = 2.5
AR = 2.5
C_P
0
-0.1
-0.2
-0.3
-0.4
-0.5
-0.6
-0.7
-0.8
-0.9
-1
-1.1
-1.2
-1.3
-1.4
-1.5

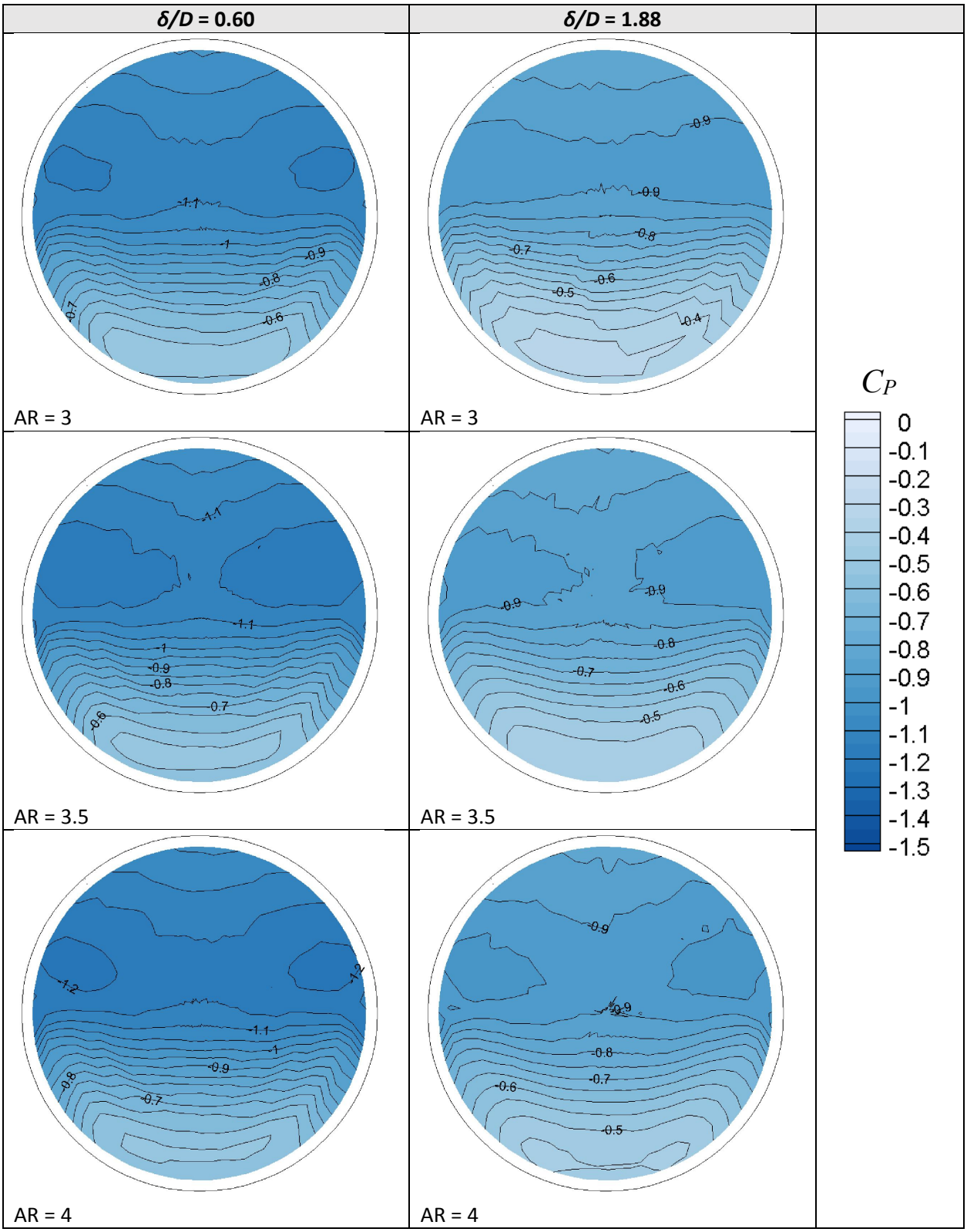
δ/D = 0.60
δ/D = 1.88
AR = 3
AR = 3
AR = 3.5
AR = 3.5
AR = 4
AR = 4
C_P
0
-0.1
-0.2
-0.3
-0.4
-0.5
-0.6
-0.7
-0.8
-0.9
-1
-1.1
-1.2
-1.3
-1.4
-1.5

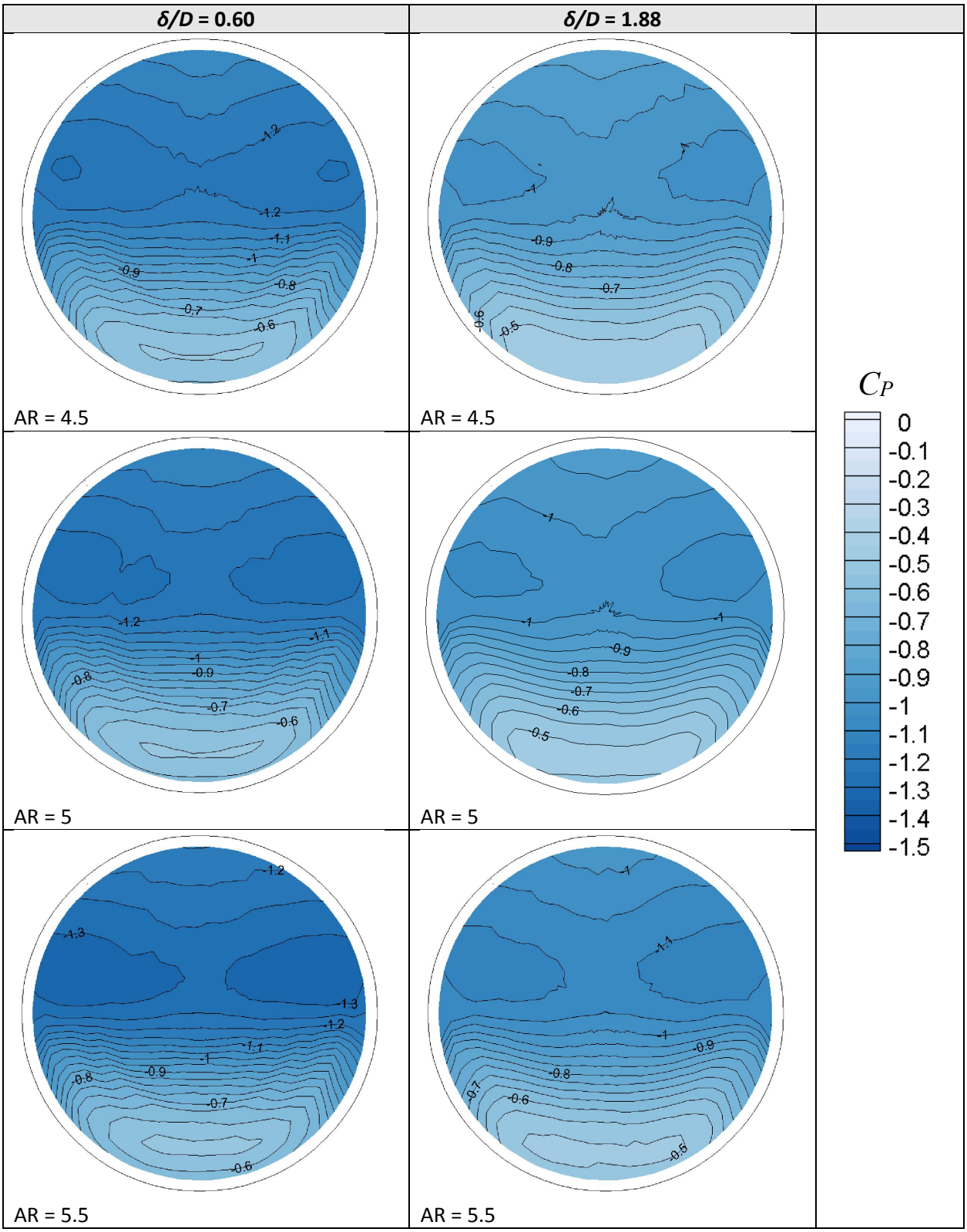
δ/D = 0.60
δ/D = 1.88
AR = 4.5
AR = 4.5
AR = 5
AR = 5
AR = 5.5
AR = 5.5
C_P
0
-0.1
-0.2
-0.3
-0.4
-0.5
-0.6
-0.7
-0.8
-0.9
-1
-1.1
-1.2
-1.3
-1.4
-1.5

δ/D = 0.60	δ/D = 1.88	
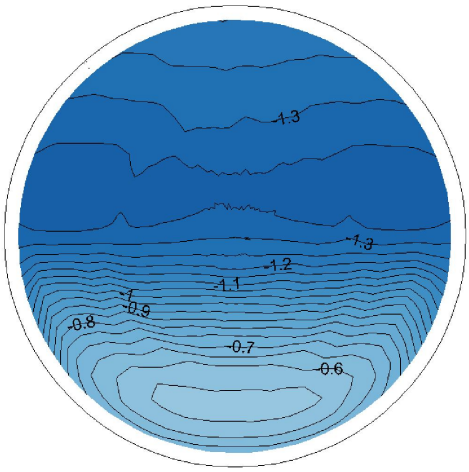 AR = 6	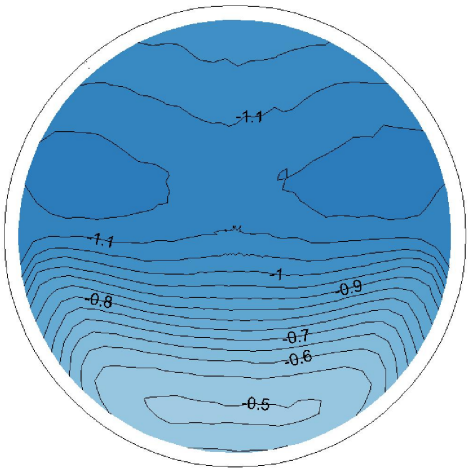 AR = 6	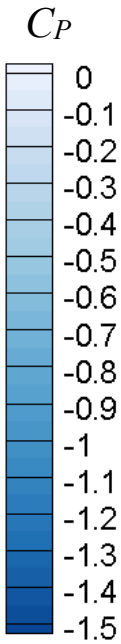
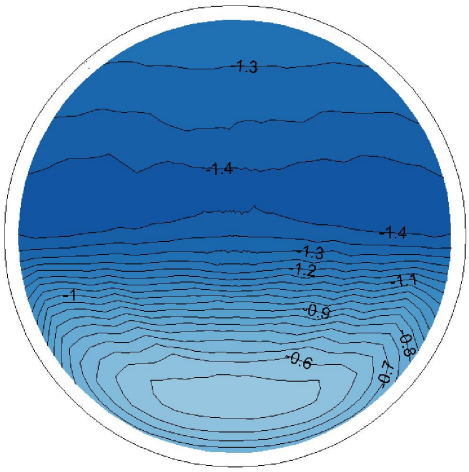 AR = 6.5	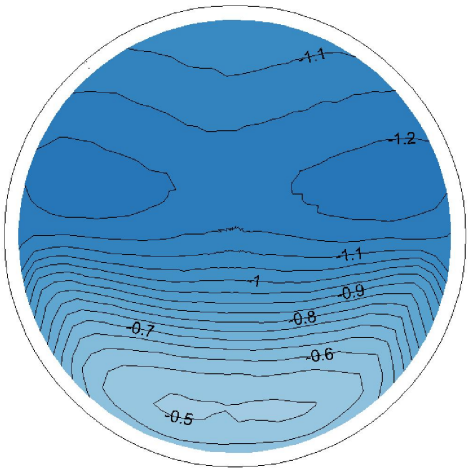 AR = 6.5	
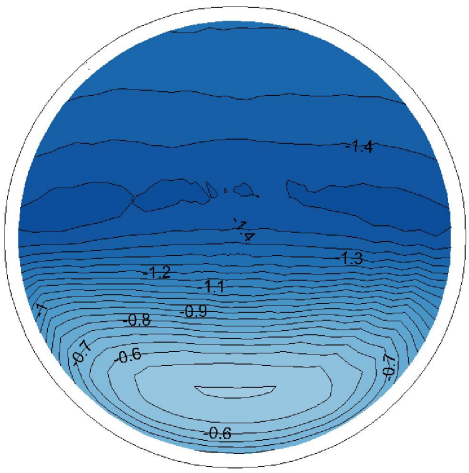 AR = 7	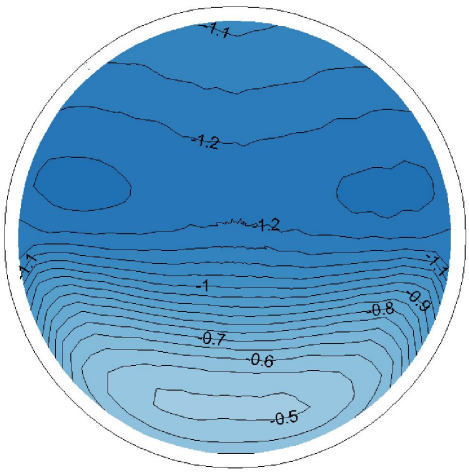 AR = 7	

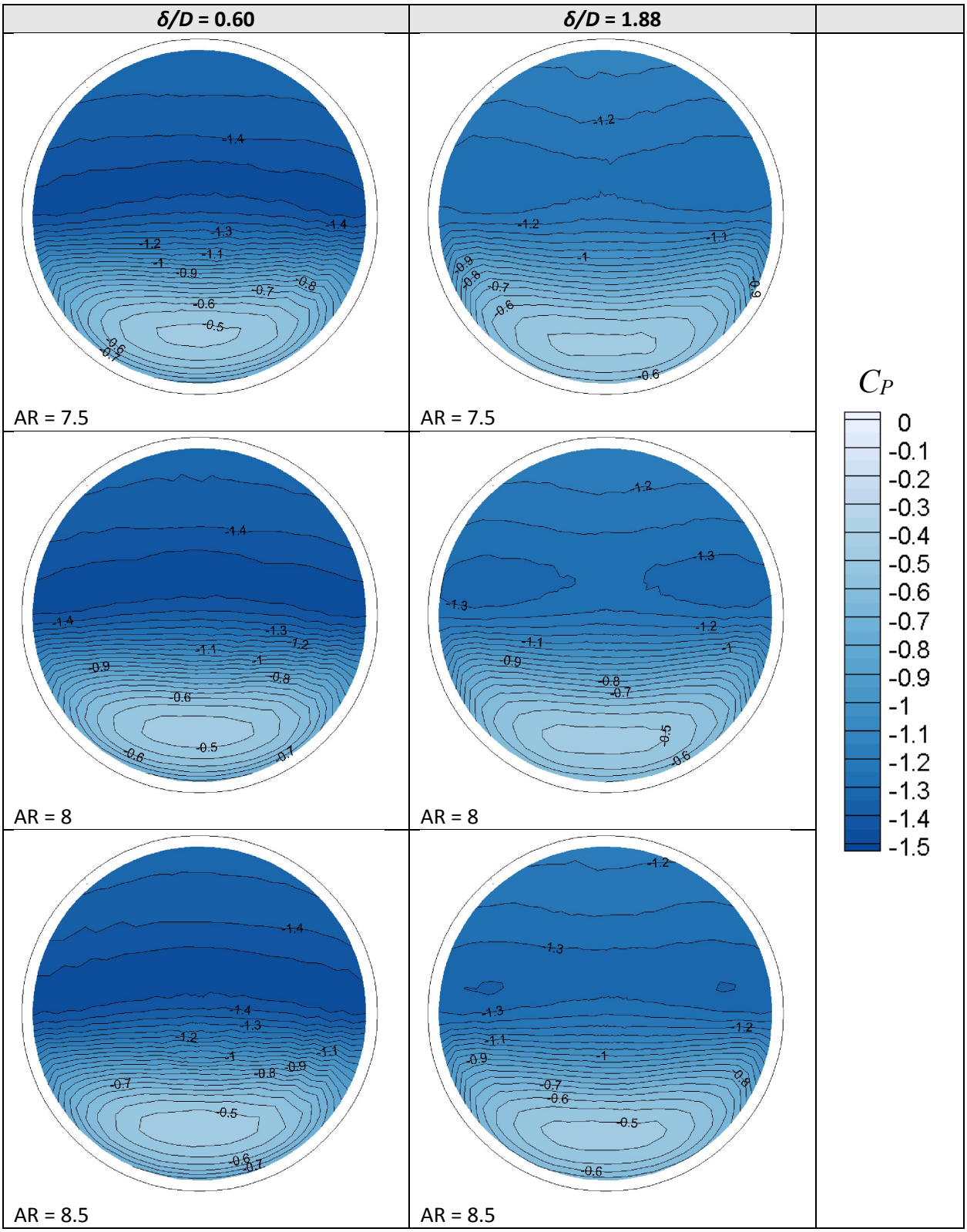
δ/D = 0.60
δ/D = 1.88
AR = 7.5
AR = 7.5
AR = 8
AR = 8
AR = 8.5
AR = 8.5
C_P
0
-0.1
-0.2
-0.3
-0.4
-0.5
-0.6
-0.7
-0.8
-0.9
-1
-1.1
-1.2
-1.3
-1.4
-1.5

δ/D = 0.60	δ/D = 1.88	
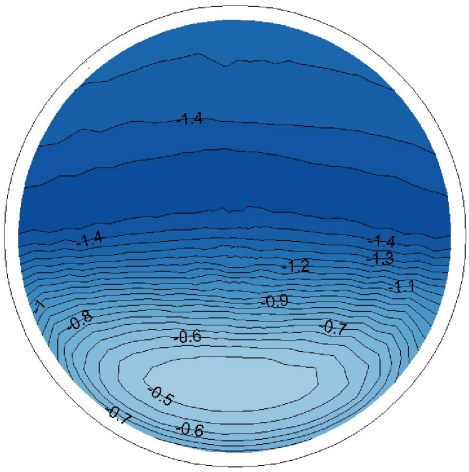 AR = 9	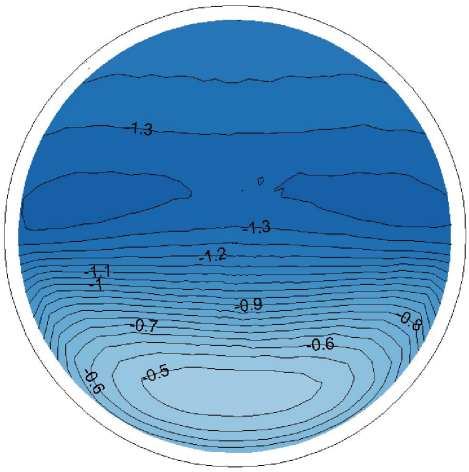 AR = 9	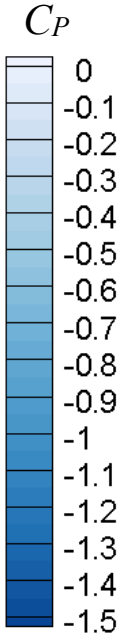
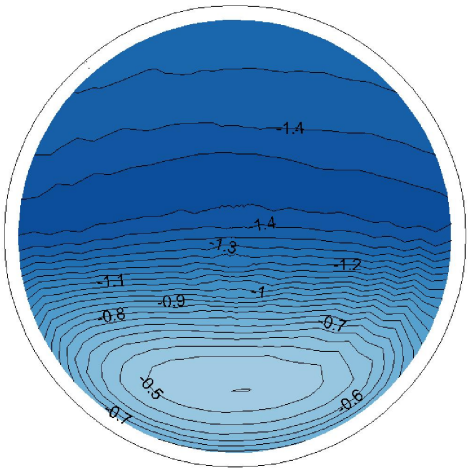 AR = 9.5	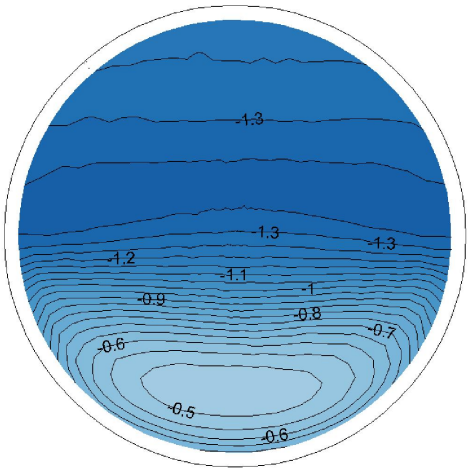 AR = 9.5	
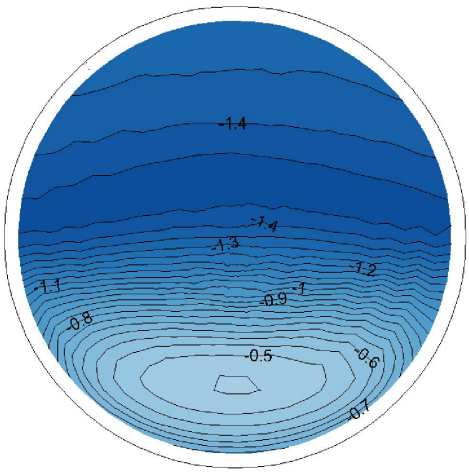 AR = 10	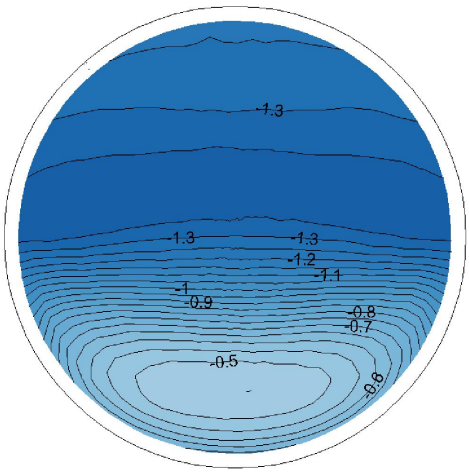 AR = 10	

δ/D = 0.60	δ/D = 1.88	
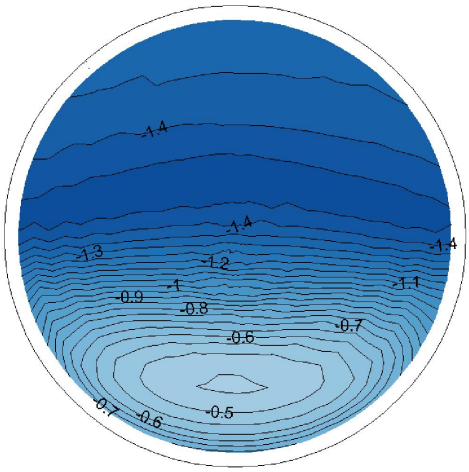 AR = 10.5	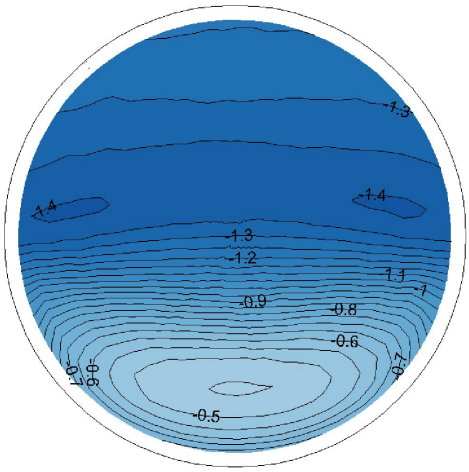 AR = 10.5	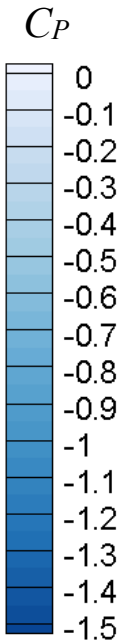
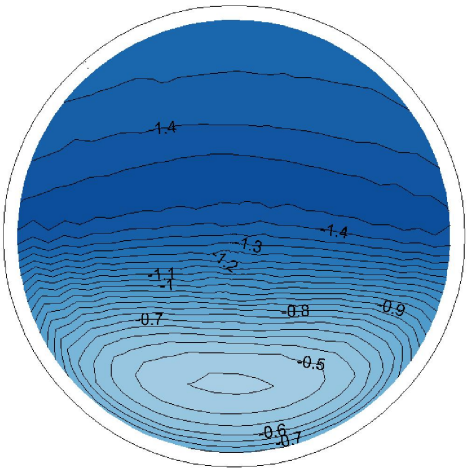 AR = 11	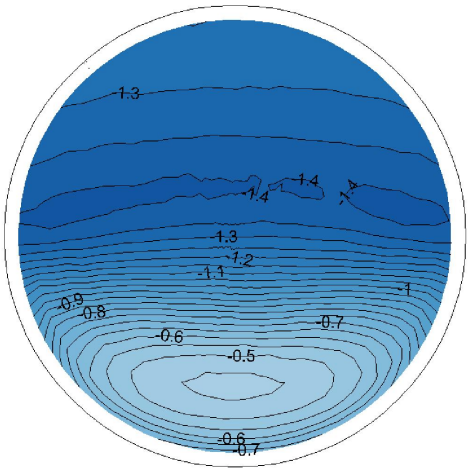 AR = 11	

Appendix C – Surface Pressure Centerline Profiles

This appendix contains the surface pressure centerline profiles generated from the free-end pressure distributions. The C_P were measured along the centerline of the free end parallel to the flow direction. All pressure coefficients are negative, and are represented in this way on the profiles.

Table C.1: Surface pressure profiles along the *x*-axis centerline of the free end of a surface-mounted finite-height cylinder of varying AR immersed in a thin and thick boundary layer. Re = 6.5×10^4. Flow is from left to right.

***δ/D* = 0.60**	***δ/D* = 1.88**
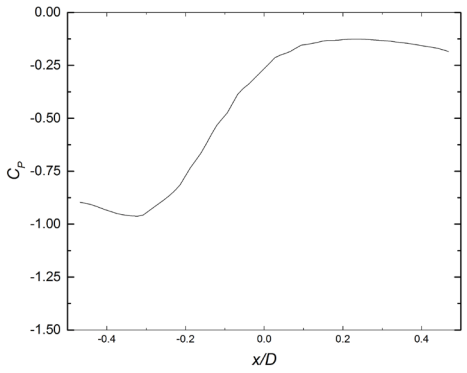 AR = 0.5	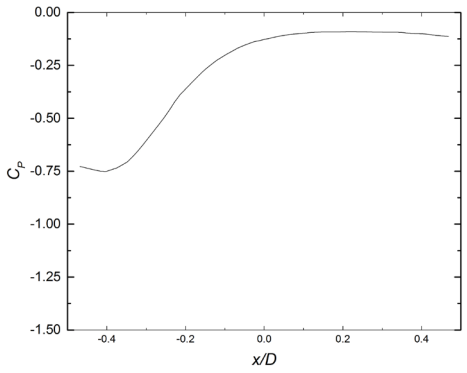 AR = 0.5
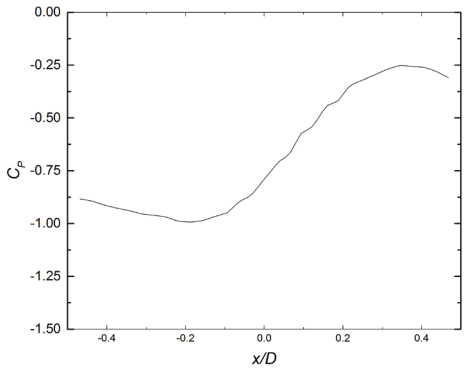 AR = 1	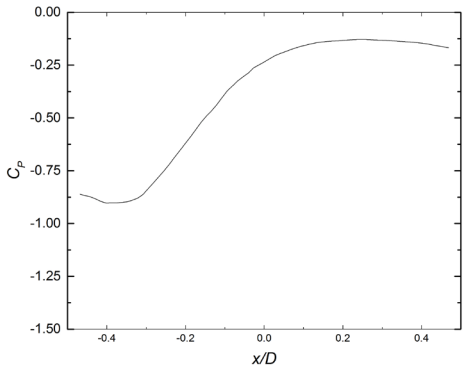 AR = 1

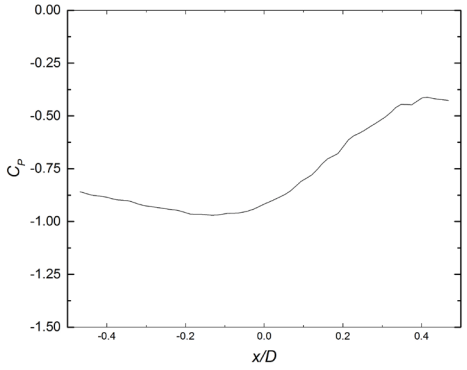

AR = 1.5

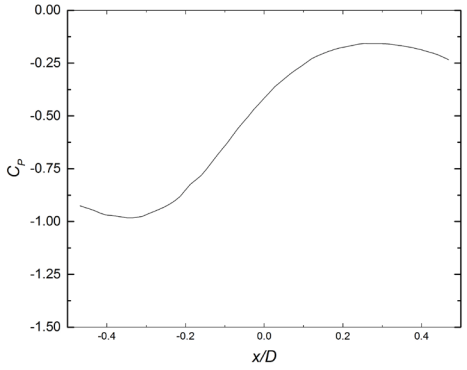

AR = 1.5

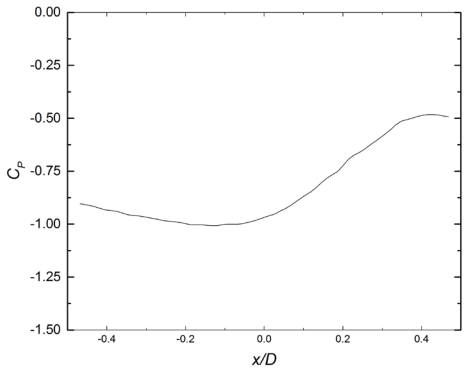

AR = 2

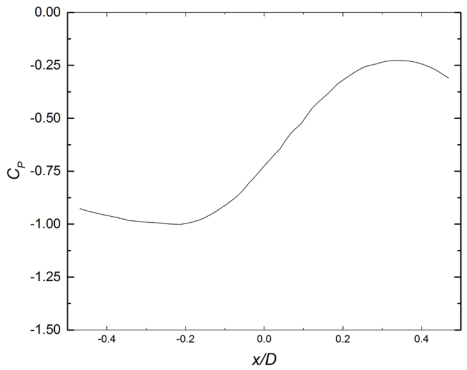

AR = 2

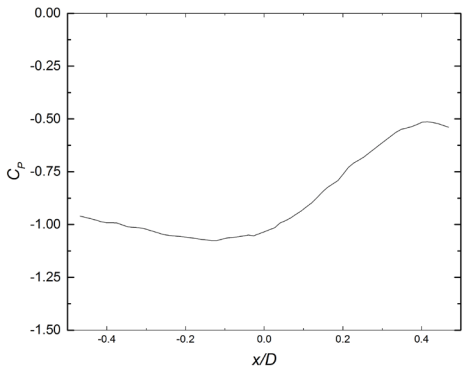

AR = 2.5

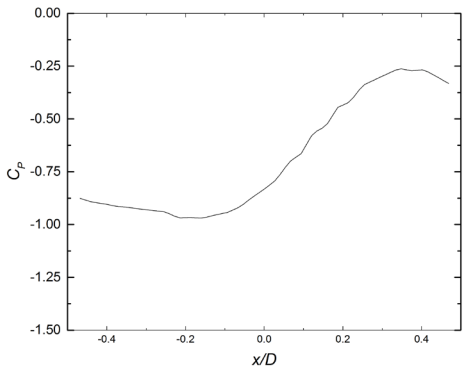

AR = 2.5

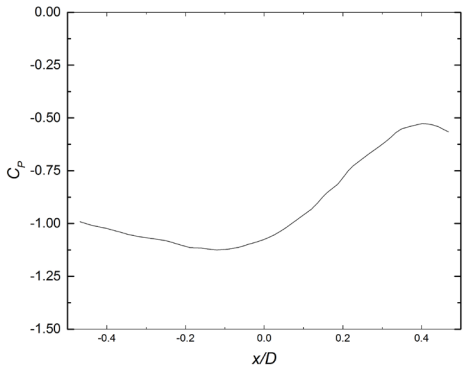

AR = 3

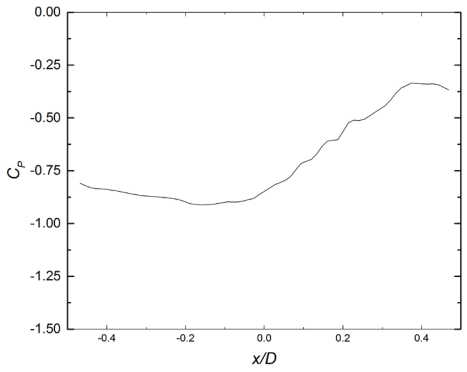

AR = 3

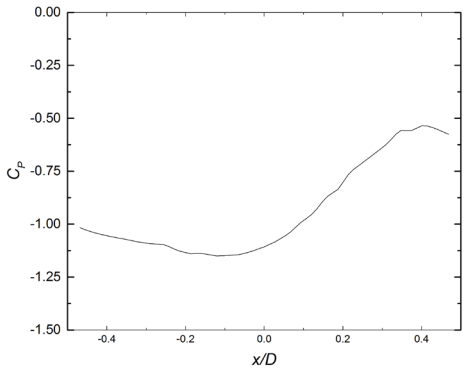

AR = 3.5

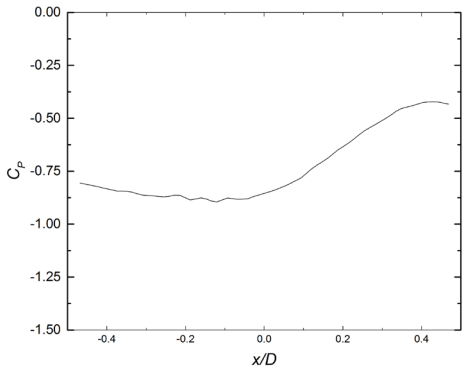

AR = 3.5

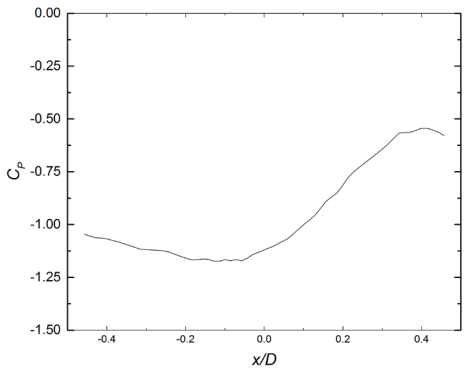

AR = 4

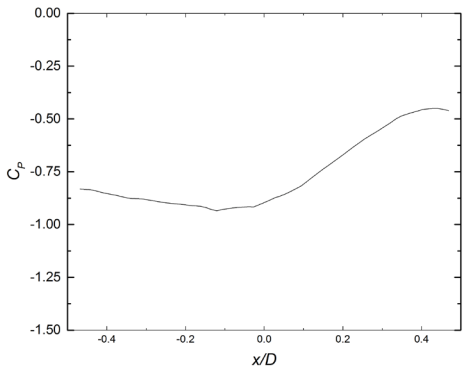

AR = 4

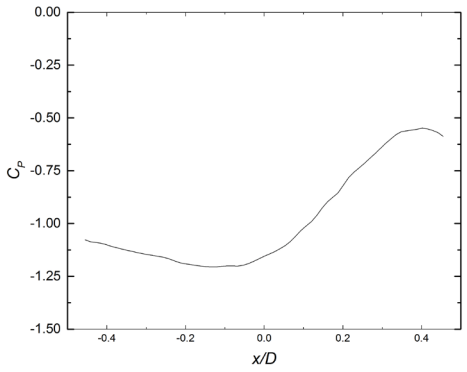

AR = 4.5

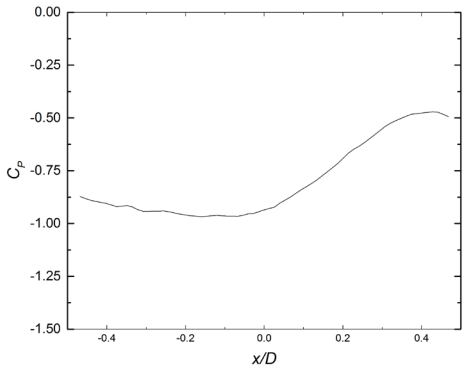

AR = 4.5

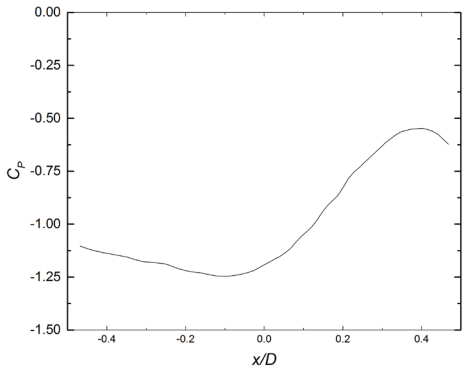

AR = 5

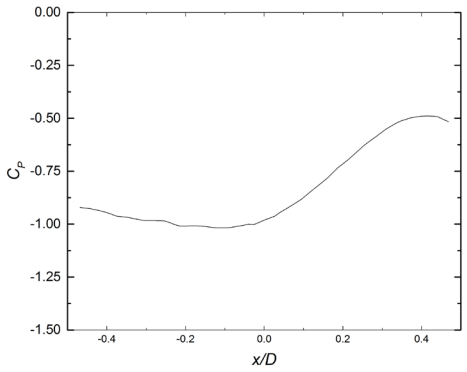

AR = 5

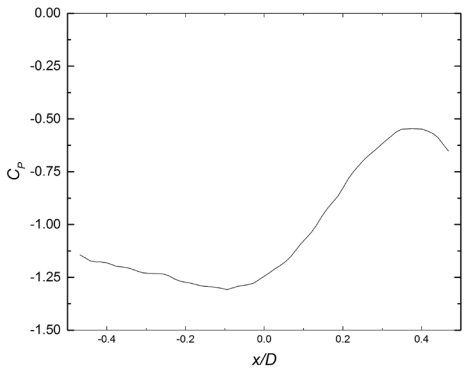

AR = 5.5

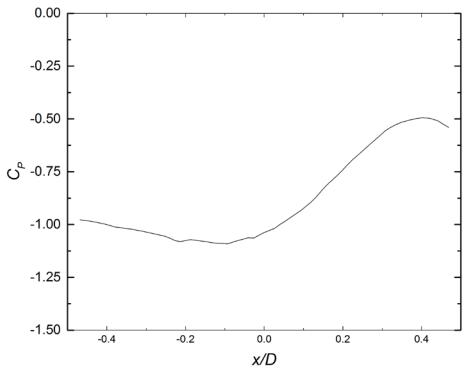

AR = 5.5

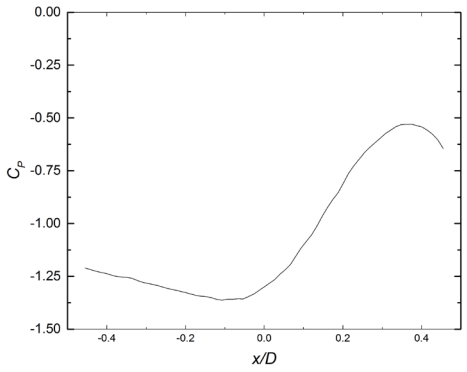

AR = 6

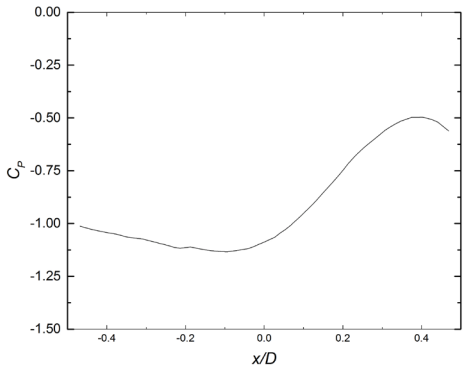

AR = 6

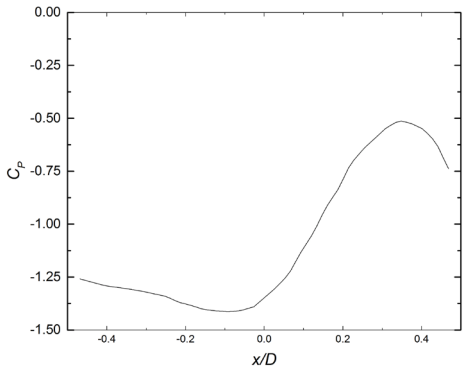

AR = 6.5

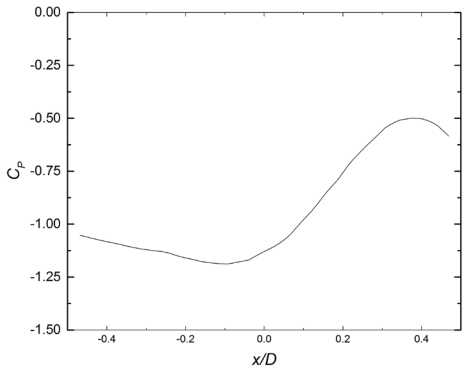

AR = 6.5

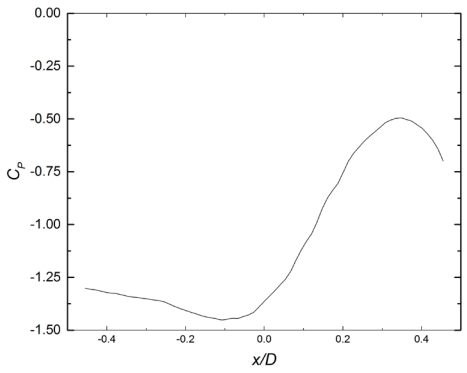

AR = 7

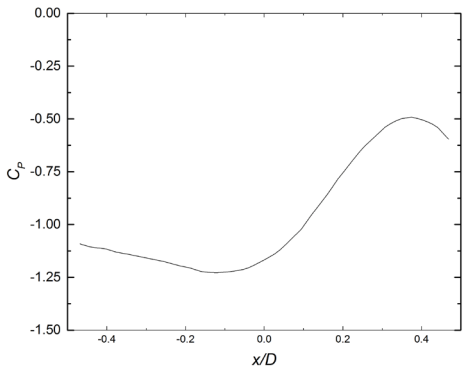

AR = 7

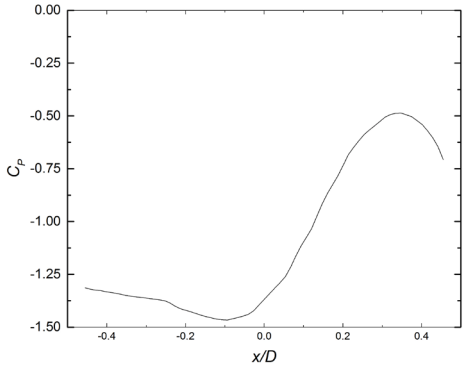

AR = 7.5

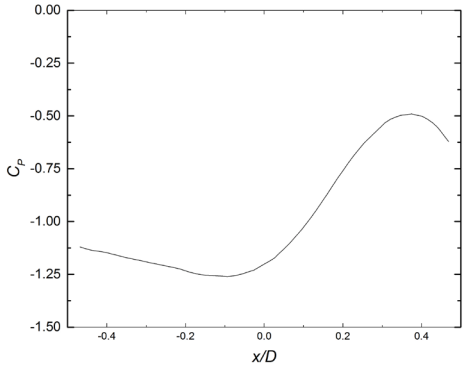

AR = 7.5

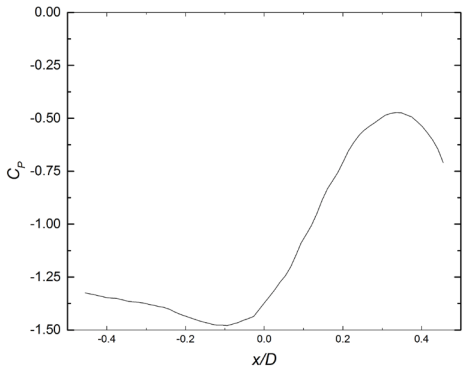

AR = 8

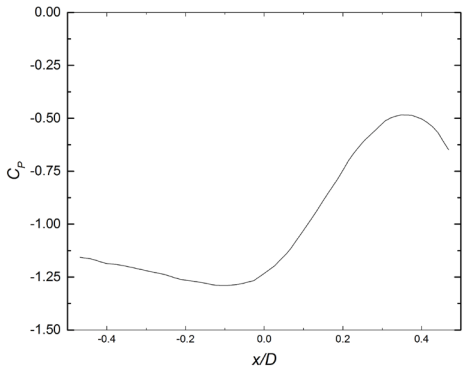

AR = 8

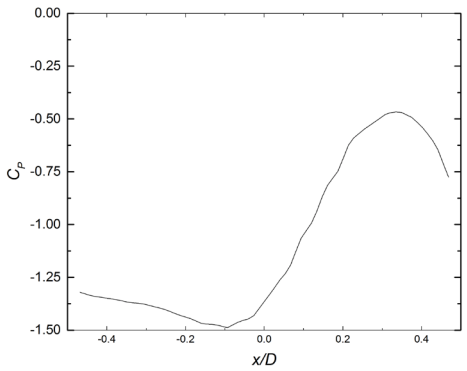

AR = 8.5

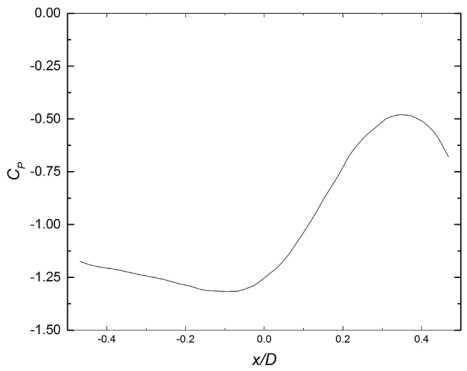

AR = 8.5

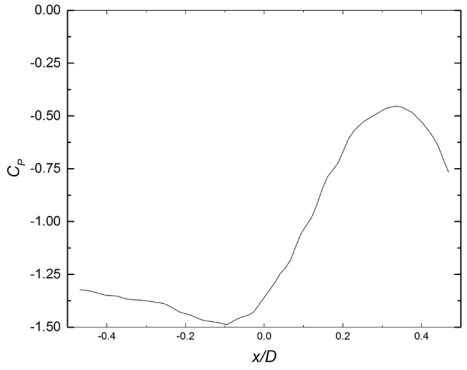 AR = 9	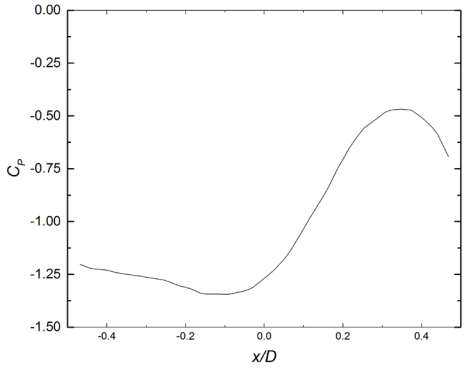 AR = 9
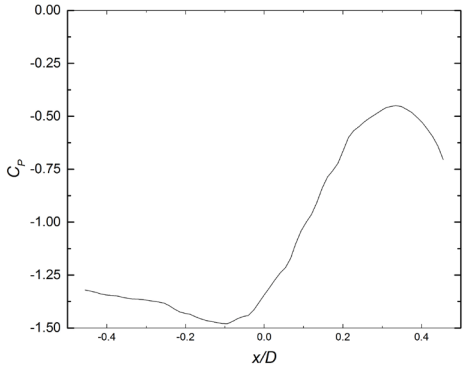 AR = 9.5	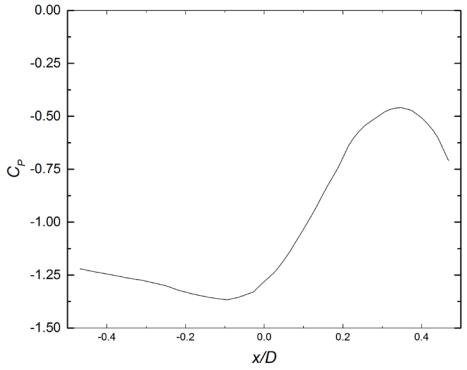 AR = 9.5
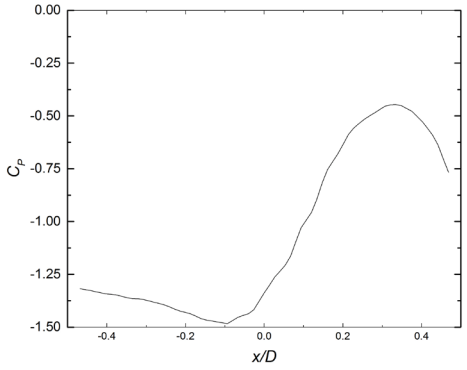 AR = 10	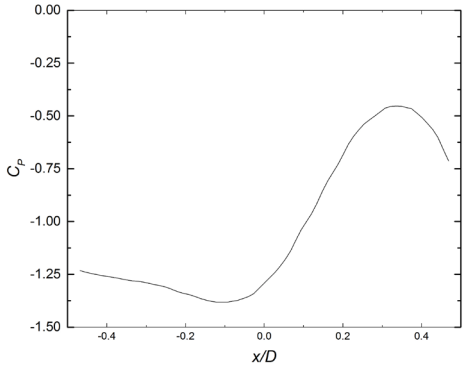 AR = 10

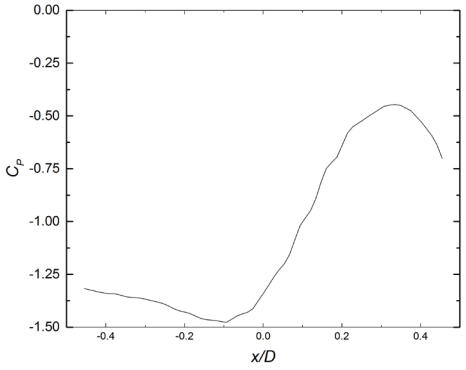

AR = 10.5

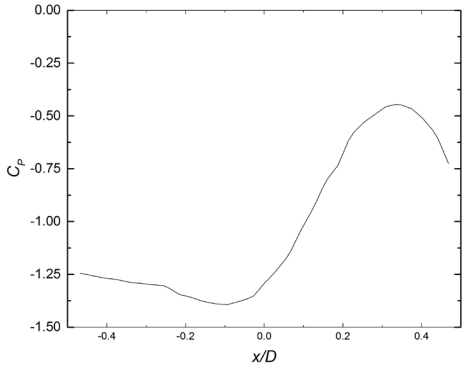

AR = 10.5

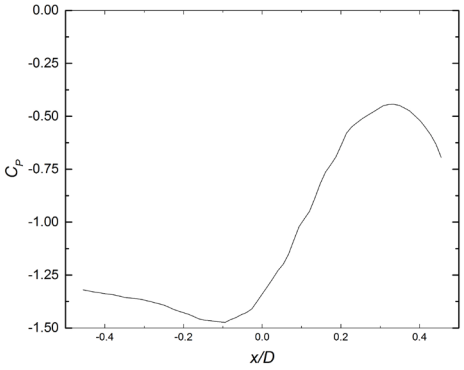

AR = 11

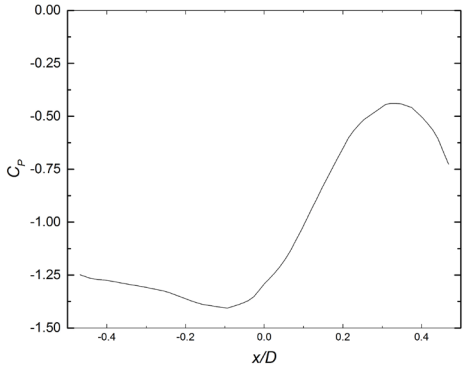

AR = 11

Appendix D – Surface Pressure Fluctuation Distributions

This appendix contains the distributions of the pressure coefficient fluctuations that were recorded for the thick cylinder. Fluctuations are shown with both a color map and contours.

Table D.1: Surface pressure fluctuation distributions for the free end of a surface-mounted finite-height cylinder of varying AR immersed in a thin and thick boundary layer. Re = 6.5×10^4. Flow is from top to bottom.

***δ/D* = 0.60**	***δ/D* = 1.88**	
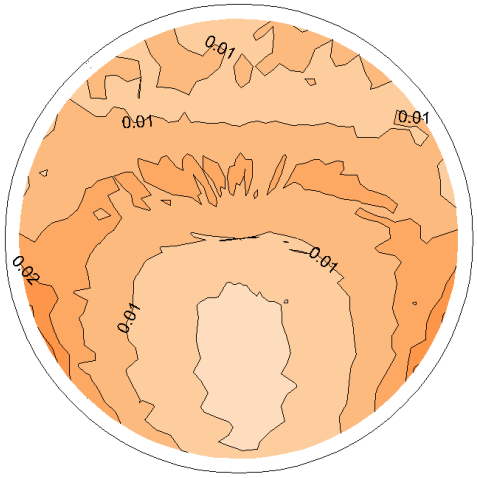 AR = 0.5	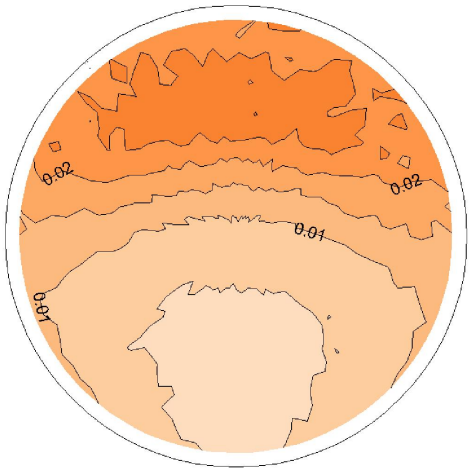 AR = 0.5	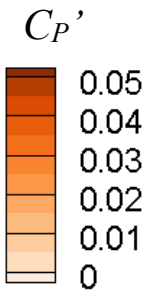
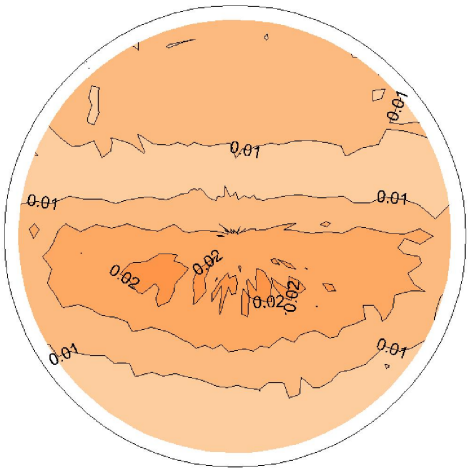 AR = 1	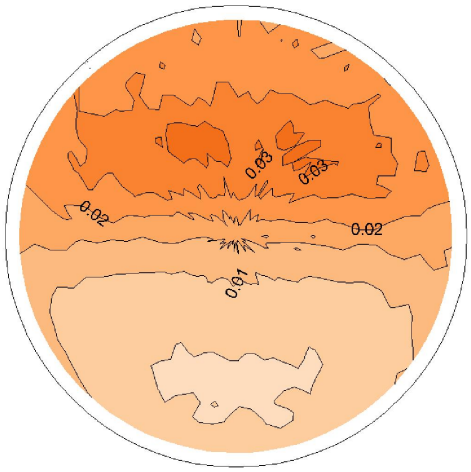 AR = 1	

δ/D = 0.60	δ/D = 1.88	
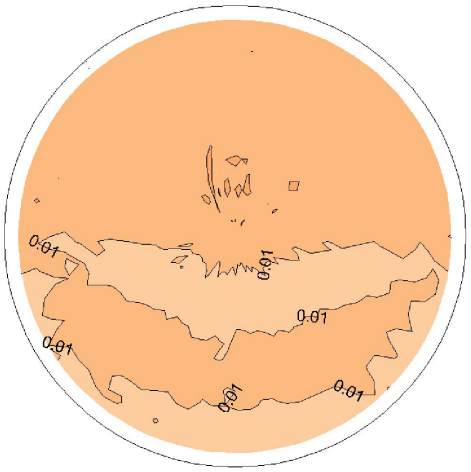	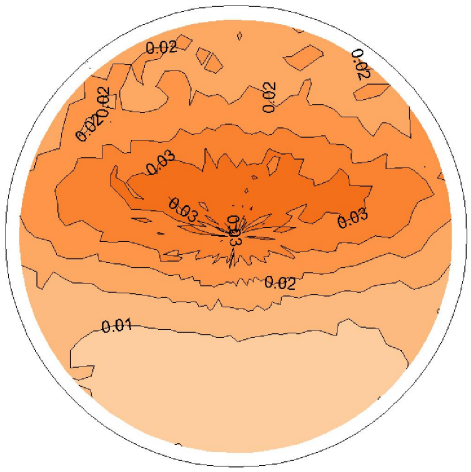	
AR = 1.5	AR = 1.5	
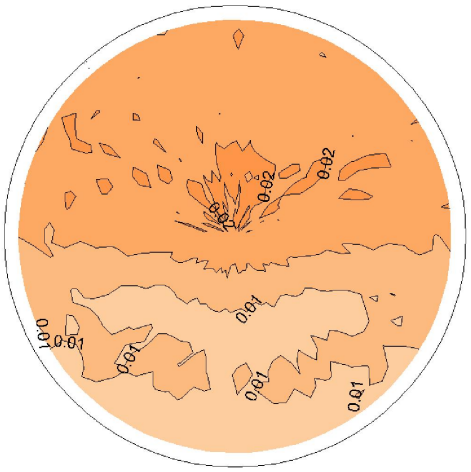	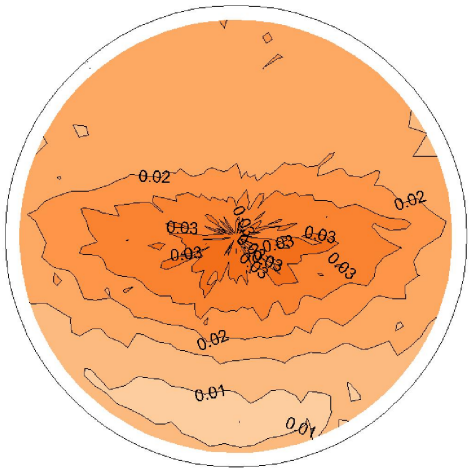	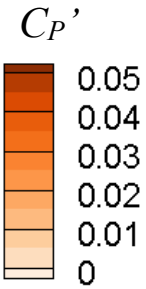
AR = 2	AR = 2	
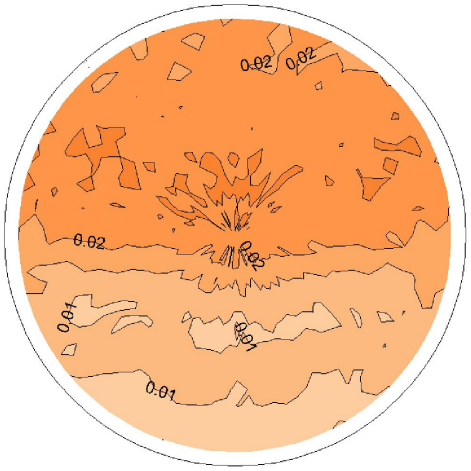	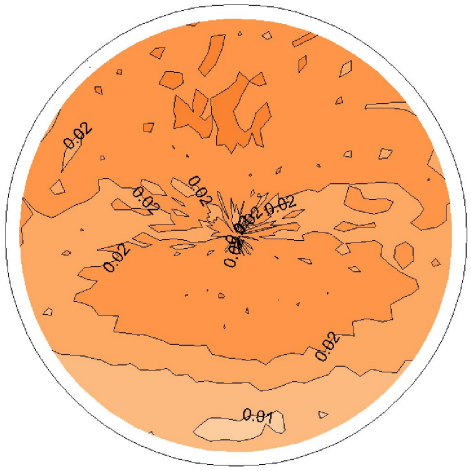	
AR = 2.5	AR = 2.5	

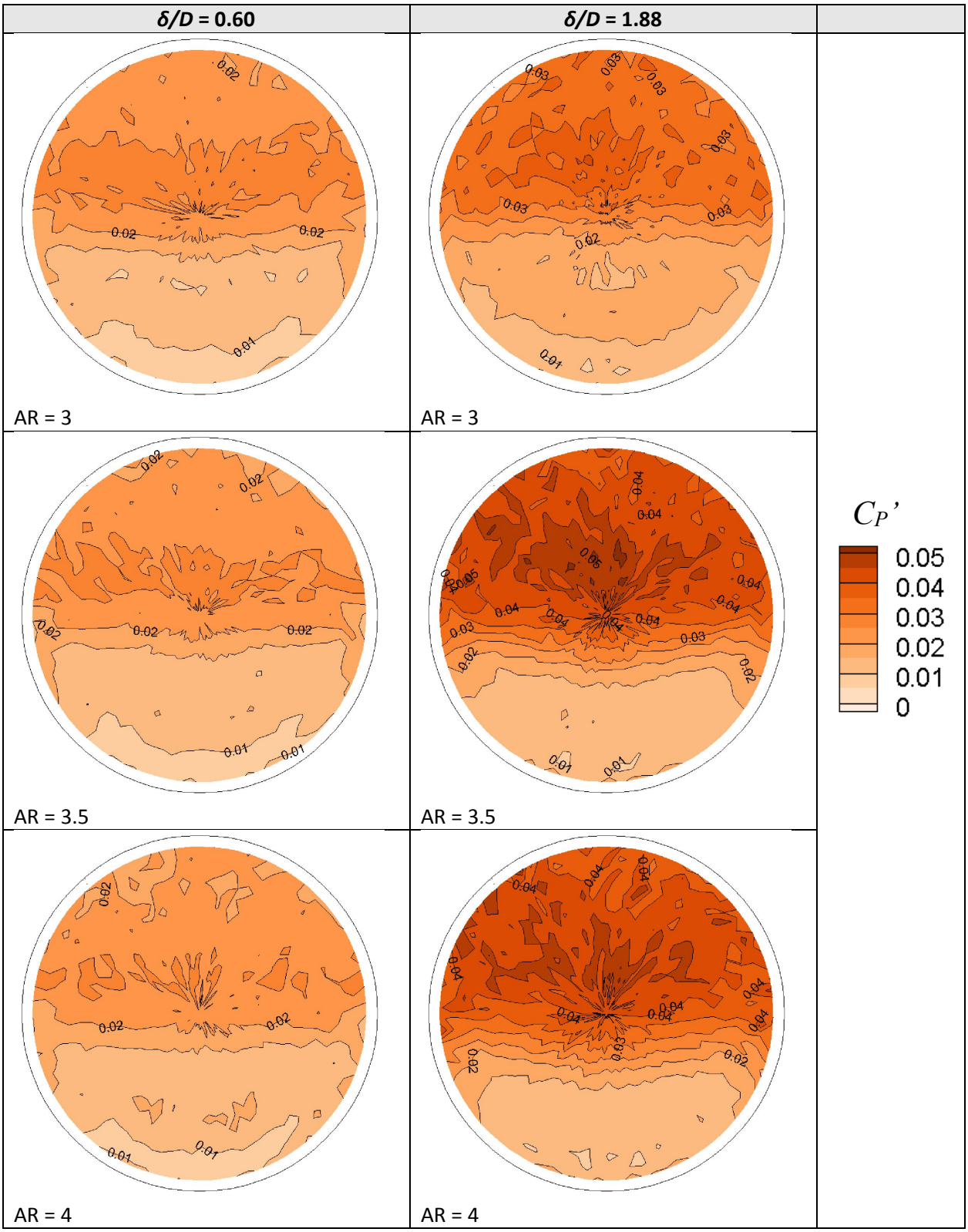
δ/D = 0.60
δ/D = 1.88
AR = 3
AR = 3
AR = 3.5
AR = 3.5
AR = 4
AR = 4
C_P'
0.05
0.04
0.03
0.02
0.01
0

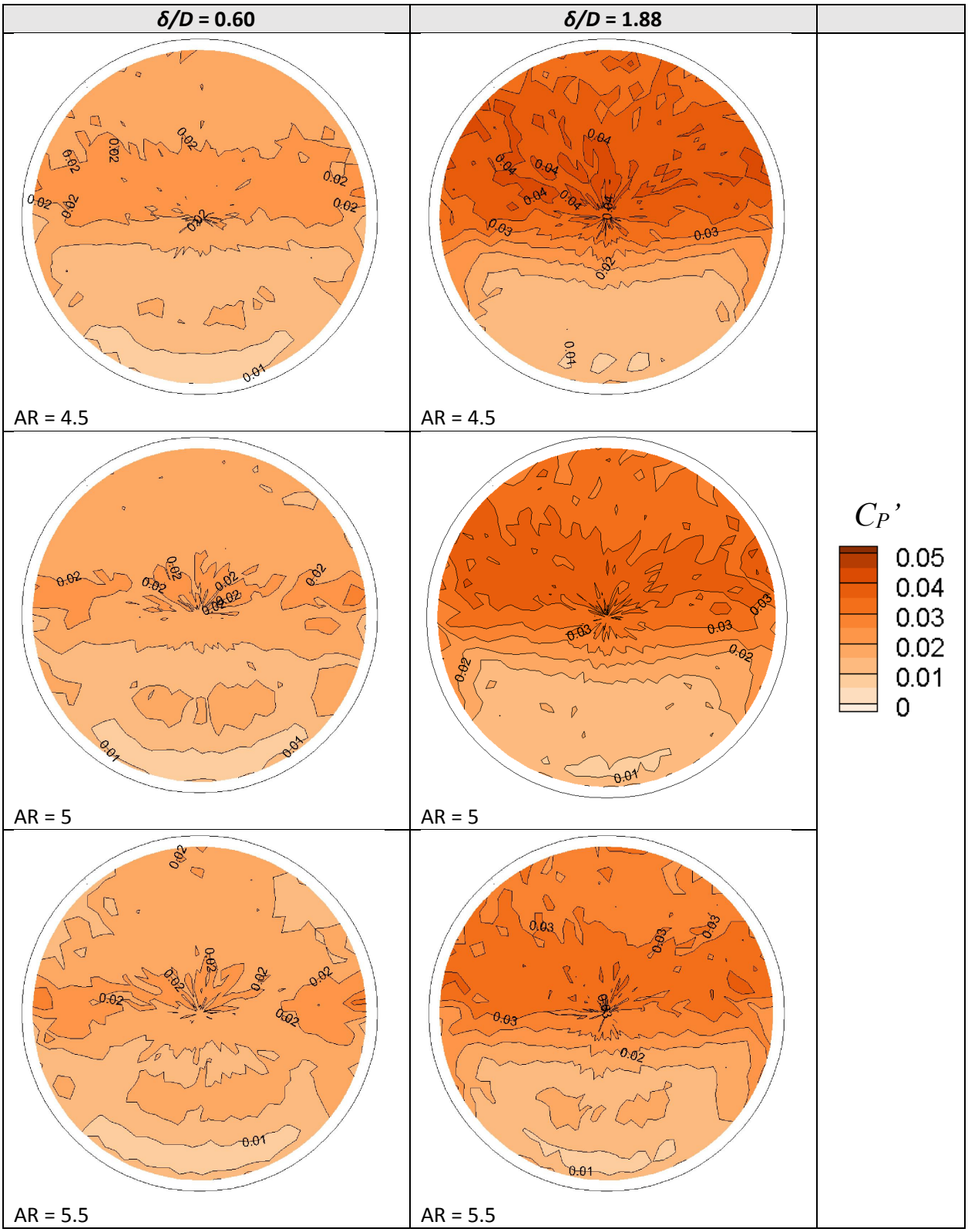
δ/D = 0.60
δ/D = 1.88
AR = 4.5
AR = 4.5
AR = 5
AR = 5
AR = 5.5
AR = 5.5
C_P'
0.05
0.04
0.03
0.02
0.01
0

δ/D = 0.60	δ/D = 1.88	
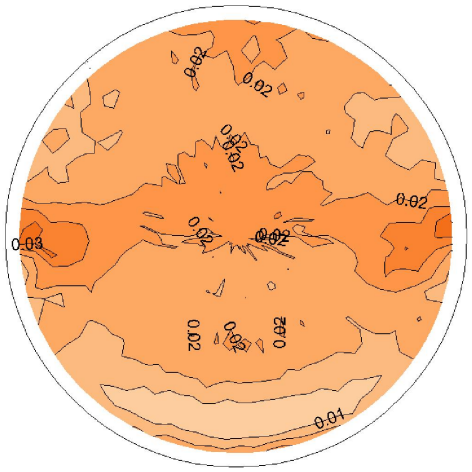 AR = 6	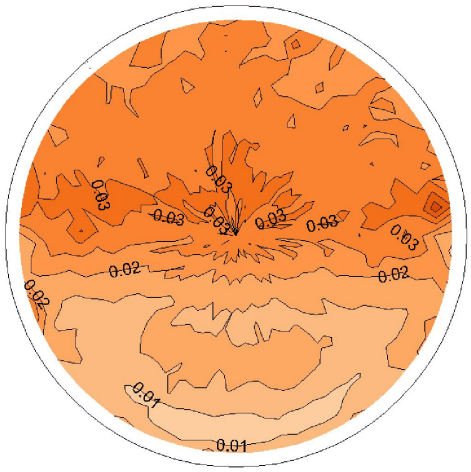 AR = 6	
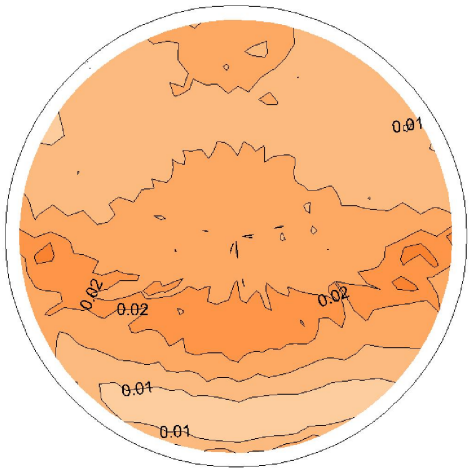 AR = 6.5	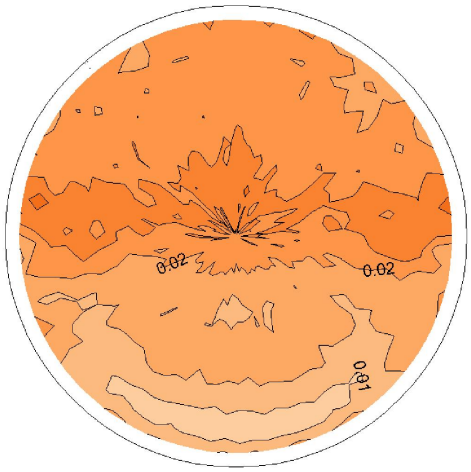 AR = 6.5	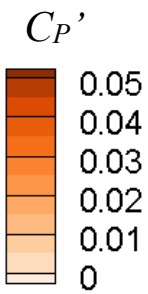
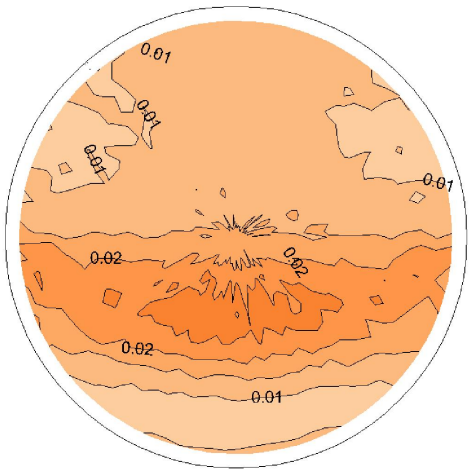 AR = 7	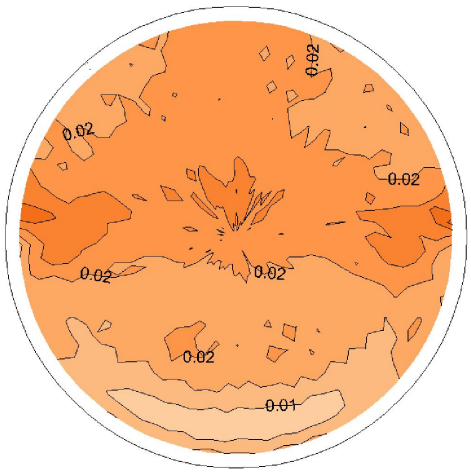 AR = 7	

δ/D = 0.60	δ/D = 1.88	
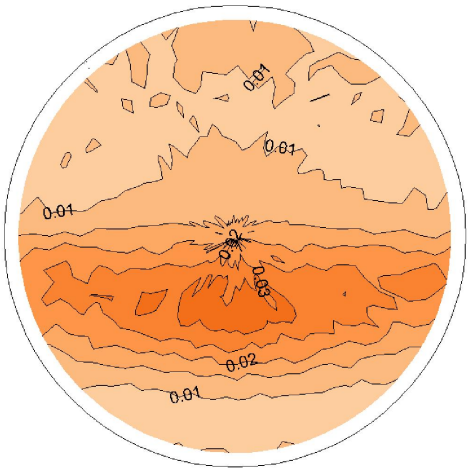 AR = 7.5	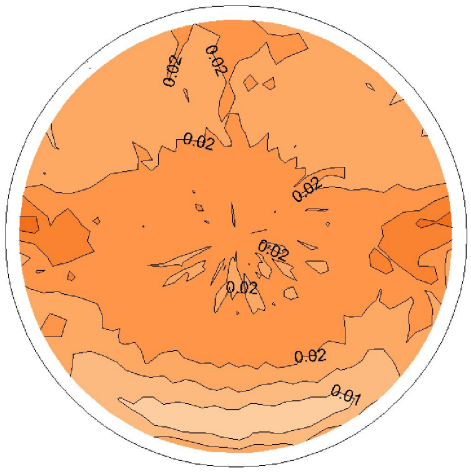 AR = 7.5	
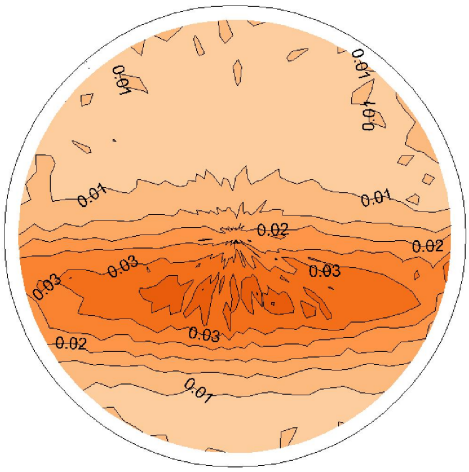 AR = 8	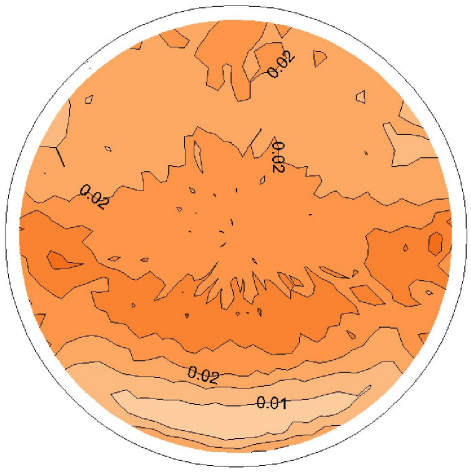 AR = 8	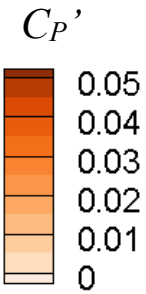
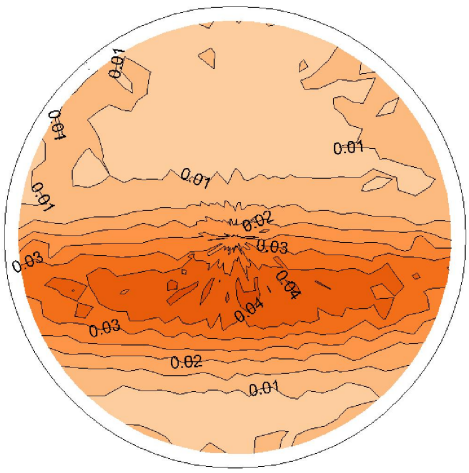 AR = 8.5	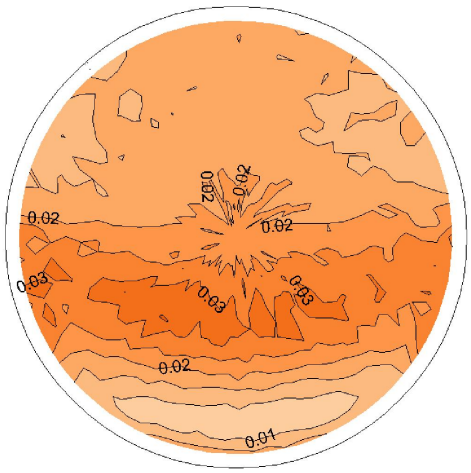 AR = 8.5	

δ/D = 0.60	δ/D = 1.88	
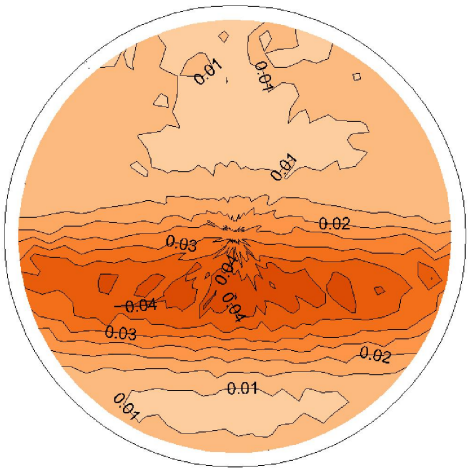 AR = 9	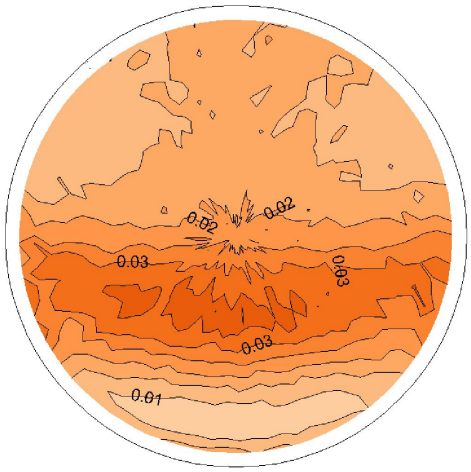 AR = 9	
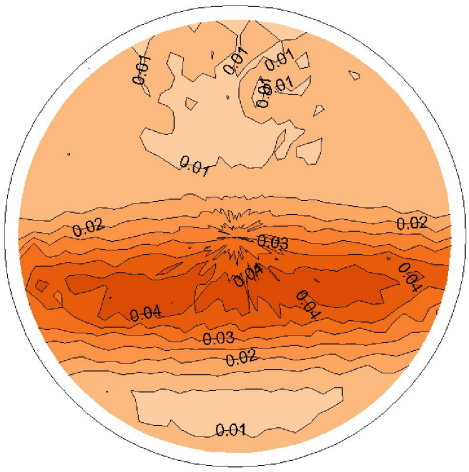 AR = 9.5	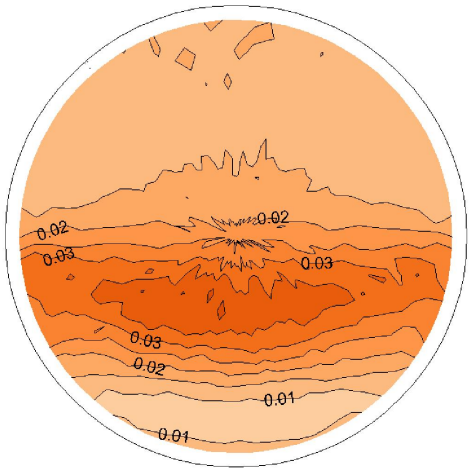 AR = 9.5	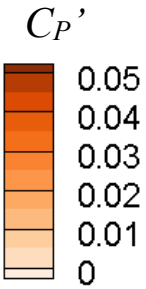
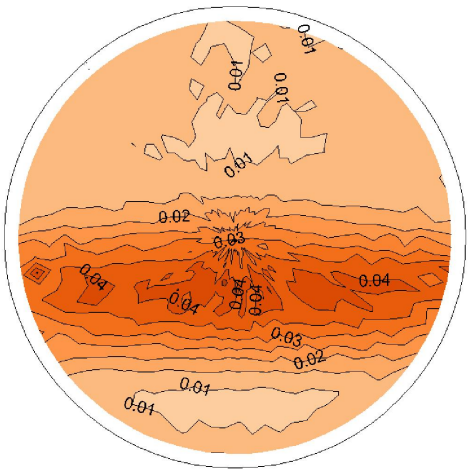 AR = 10	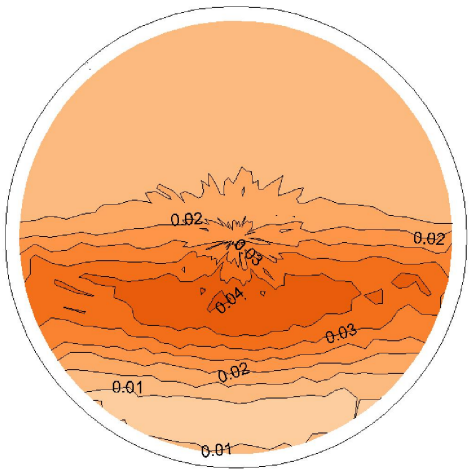 AR = 10	

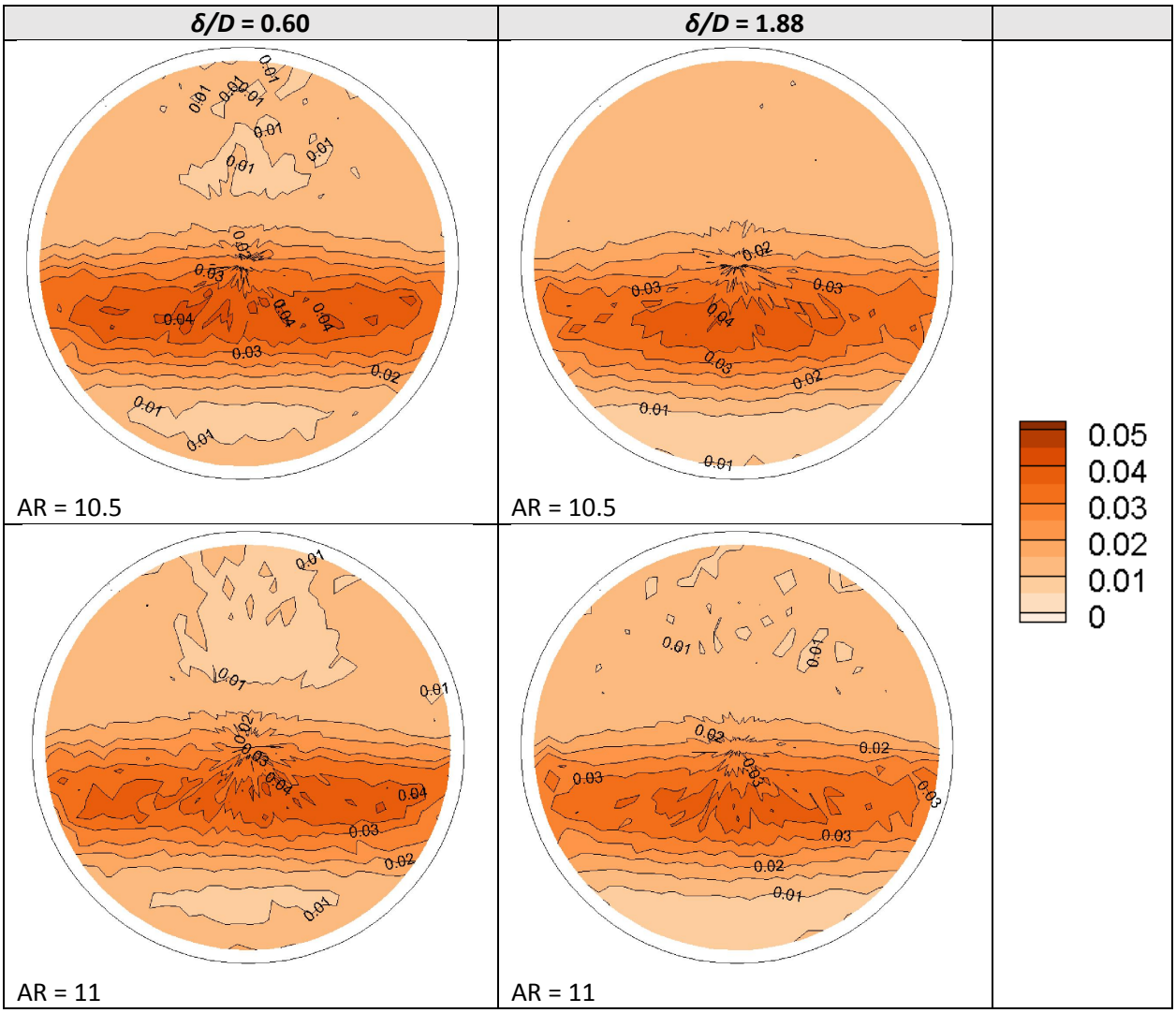
δ/D = 0.60
δ/D = 1.88
AR = 10.5
AR = 10.5
AR = 11
AR = 11
0.05
0.04
0.03
0.02
0.01
0

Appendix E – Permissions Agreements

This appendix contains the permissions agreements issued for the figures used in this thesis, presented in order of appearance.

ELSEVIER LICENSE TERMS AND CONDITIONS

This Agreement between University of Saskatchewan -- Adam Beitel ("You") and Elsevier ("Elsevier") consists of your license details and the terms and conditions provided by Elsevier and Copyright Clearance Center.

printable details	
License Number	4156571191023
License date	Jul 26, 2017
Licensed Content Publisher	Elsevier
Licensed Content Publication	Journal of Fluids and Structures
Licensed Content Title	Effects of free-end corner shape on flow structure around a finite cylinder
Licensed Content Author	C.W. Park,S.J. Lee
Licensed Content Date	Feb 1, 2004
Licensed Content Volume	19
Licensed Content Issue	2
Licensed Content Pages	18
Type of Use	reuse in a thesis/dissertation
Portion	figures/tables/illustrations
Number of figures/tables/illustrations	1
Format	both print and electronic
Are you the author of this Elsevier article?	No
Will you be translating?	No
Original figure numbers	Figure 5 (a)
Title of your thesis/dissertation	THE EFFECT OF ASPECT RATIO ON THE AERODYNAMIC FORCES AND FREE END PRESSURE DISTRIBUTION FOR A SURFACE-MOUNTED FINITE HEIGHT CYLINDER
Expected completion date	Aug 2017
Estimated size (number of pages)	150
Requestor Location	University of Saskatchewan 57 Campus Drive Saskatoon, SK s7n5a9 Canada Attn: Adam Beitel
Total	**0.00 CAD**

SPRINGER LICENSE
TERMS AND CONDITIONS

This Agreement between University of Saskatchewan -- Adam Beitel ("You") and Springer ("Springer") consists of your license details and the terms and conditions provided by Springer and Copyright Clearance Center.

printable details	
License Number	4156590459886
License date	Jul 26, 2017
Licensed Content Publisher	Springer
Licensed Content Publication	Experiments in Fluids
Licensed Content Title	Measurements of the flow over a low-aspect-ratio cylinder mounted on a ground plane
Licensed Content Author	R. J. Pattenden
Licensed Content Date	Jan 1, 2005
Licensed Content Volume	39
Licensed Content Issue	1
Type of Use	Thesis/Dissertation
Portion	Figures/tables/illustrations
Number of figures/tables/illustrations	1
Author of this Springer article	No
Order reference number	
Original figure numbers	Figure 2
Title of your thesis / dissertation	THE EFFECT OF ASPECT RATIO ON THE AERODYNAMIC FORCES AND FREE END PRESSURE DISTRIBUTION FOR A SURFACE-MOUNTED FINITE HEIGHT CYLINDER
Expected completion date	Aug 2017
Estimated size(pages)	150
Requestor Location	University of Saskatchewan 57 Campus Drive Saskatoon, SK s7n5a9 Canada Attn: Adam Beitel
Billing Type	Invoice
Billing address	University of Saskatchewan 57 Campus Drive Saskatoon, SK s7n5a9 Canada Attn: Adam Beitel
Total	**0.00 CAD**

CAMBRIDGE UNIVERSITY PRESS LICENSE TERMS AND CONDITIONS

This Agreement between University of Saskatchewan -- Adam Beitel ("You") and Cambridge University Press ("Cambridge University Press") consists of your license details and the terms and conditions provided by Cambridge University Press and Copyright Clearance Center.

License Number	4156150294890
License date	Jul 25, 2017
Licensed Content Publisher	Cambridge University Press
Licensed Content Publication	The Journal of Fluid Mechanics
Licensed Content Title	Flow around a tall finite cylinder explored by large eddy simulation
Licensed Content Author	SINIŠA KRAJNOVIĆ
Licensed Content Date	Apr 4, 2011
Licensed Content Volume	676
Licensed Content Issue	undefined
Start page	294
End page	317
Type of Use	Dissertation/Thesis
Requestor type	Author
Portion	Text extract
Number of pages requested	3
Author of this Cambridge University Press article	No
Author / editor of the new work	Yes
Territory for reuse	World
Title of your thesis / dissertation	THE EFFECT OF ASPECT RATIO ON THE AERODYNAMIC FORCES AND FREE END PRESSURE DISTRIBUTION FOR A SURFACE-MOUNTED FINITE HEIGHT CYLINDER
Expected completion date	Aug 2017
Estimated size(pages)	150
Requestor Location	University of Saskatchewan 57 Campus Drive Saskatoon, SK s7n5a9 Canada, Attn: Adam Beitel
Publisher Tax ID	123258667RT0001
Billing Type	Invoice
Billing address	University of Saskatchewan 57 Campus Drive Saskatoon, SK s7n5a9 Canada, Attn: Adam Beitel
Total	**0.00 CAD**

ELSEVIER LICENSE
TERMS AND CONDITIONS

This Agreement between University of Saskatchewan -- Adam Beitel ("You") and Elsevier ("Elsevier") consists of your license details and the terms and conditions provided by Elsevier and Copyright Clearance Center.

printable details	
License Number	4159420739525
License date	Jul 31, 2017
Licensed Content Publisher	Elsevier
Licensed Content Publication	Journal of Wind Engineering and Industrial Aerodynamics
Licensed Content Title	The turbulent horseshoe vortex
Licensed Content Author	C.J. Baker
Licensed Content Date	Jul 1, 1980
Licensed Content Volume	6
Licensed Content Issue	1-2
Licensed Content Pages	15
Type of Use	reuse in a thesis/dissertation
Portion	figures/tables/illustrations
Number of figures/tables/illustrations	1
Format	both print and electronic
Are you the author of this Elsevier article?	No
Will you be translating?	No
Original figure numbers	Figure 3
Title of your thesis/dissertation	THE EFFECT OF ASPECT RATIO ON THE AERODYNAMIC FORCES AND FREE END PRESSURE DISTRIBUTION FOR A SURFACE-MOUNTED FINITE HEIGHT CYLINDER
Expected completion date	Aug 2017
Estimated size (number of pages)	150
Requestor Location	University of Saskatchewan 57 Campus Drive Saskatoon, SK s7n5a9 Canada Attn: Adam Beitel
Total	**0.00 CAD**

ELSEVIER LICENSE
TERMS AND CONDITIONS

This Agreement between University of Saskatchewan -- Adam Beitel ("You") and Elsevier ("Elsevier") consists of your license details and the terms and conditions provided by Elsevier and Copyright Clearance Center.

printable details	
License Number	4156571455272
License date	Jul 26, 2017
Licensed Content Publisher	Elsevier
Licensed Content Publication	Journal of Wind Engineering and Industrial Aerodynamics
Licensed Content Title	Turbulence and separation induced pressure fluctuations on a finite circular cylinder — application of a linear unsteady strip theory
Licensed Content Author	Norbert Hölscher,Hans-Jürgen Niemann
Licensed Content Date	Dec 1, 1996
Licensed Content Volume	65
Licensed Content Issue	1-3
Licensed Content Pages	12
Type of Use	reuse in a thesis/dissertation
Portion	figures/tables/illustrations
Number of figures/tables/illustrations	1
Format	both print and electronic
Are you the author of this Elsevier article?	No
Will you be translating?	No
Original figure numbers	Figure 1
Title of your thesis/dissertation	THE EFFECT OF ASPECT RATIO ON THE AERODYNAMIC FORCES AND FREE END PRESSURE DISTRIBUTION FOR A SURFACE-MOUNTED FINITE HEIGHT CYLINDER
Expected completion date	Aug 2017
Estimated size (number of pages)	150
Requestor Location	University of Saskatchewan 57 Campus Drive Saskatoon, SK s7n5a9 Canada Attn: Adam Beitel
Total	**0.00 CAD**

SPRINGER LICENSE
TERMS AND CONDITIONS

This Agreement between University of Saskatchewan -- Adam Beitel ("You") and Springer ("Springer") consists of your license details and the terms and conditions provided by Springer and Copyright Clearance Center.

License Number	4156590651839
License date	Jul 26, 2017
Licensed Content Publisher	Springer
Licensed Content Publication	Heat and Mass Transfer
Licensed Content Title	Surface flow pattern and local mass transfer on the free-end surface of a finite circular cylinder
Licensed Content Author	Sung Cheoul Roh
Licensed Content Date	Jan 1, 2001
Licensed Content Volume	38
Licensed Content Issue	1
Type of Use	Thesis/Dissertation
Portion	Figures/tables/illustrations
Number of figures/tables/illustrations	1
Author of this Springer article	No
Order reference number	
Original figure numbers	Figure 2 (c)
Title of your thesis / dissertation	THE EFFECT OF ASPECT RATIO ON THE AERODYNAMIC FORCES AND FREE END PRESSURE DISTRIBUTION FOR A SURFACE-MOUNTED FINITE HEIGHT CYLINDER
Expected completion date	Aug 2017
Estimated size(pages)	150
Requestor Location	University of Saskatchewan 57 Campus Drive Saskatoon, SK s7n5a9 Canada, Attn: Adam Beitel
Billing Type	Invoice
Billing address	University of Saskatchewan 57 Campus Drive Saskatoon, SK s7n5a9 Canada, Attn: Adam Beitel
Total	**0.00 CAD**

SPRINGER LICENSE
TERMS AND CONDITIONS

This Agreement between University of Saskatchewan -- Adam Beitel ("You") and Springer ("Springer") consists of your license details and the terms and conditions provided by Springer and Copyright Clearance Center.

printable details	
License Number	4156590575772
License date	Jul 26, 2017
Licensed Content Publisher	Springer
Licensed Content Publication	Experiments in Fluids
Licensed Content Title	Vortical flow over the free end surface of a finite circular cylinder mounted on a flat plate
Licensed Content Author	S. Roh
Licensed Content Date	Jan 1, 2003
Licensed Content Volume	34
Licensed Content Issue	1
Type of Use	Thesis/Dissertation
Portion	Figures/tables/illustrations
Number of figures/tables/illustrations	1
Author of this Springer article	No
Order reference number	
Original figure numbers	Figure 6
Title of your thesis / dissertation	THE EFFECT OF ASPECT RATIO ON THE AERODYNAMIC FORCES AND FREE END PRESSURE DISTRIBUTION FOR A SURFACE-MOUNTED FINITE HEIGHT CYLINDER
Expected completion date	Aug 2017
Estimated size(pages)	150
Requestor Location	University of Saskatchewan 57 Campus Drive Saskatoon, SK s7n5a9 Canada Attn: Adam Beitel
Billing Type	Invoice
Billing address	University of Saskatchewan 57 Campus Drive Saskatoon, SK s7n5a9 Canada Attn: Adam Beitel
Total	**0.00 CAD**

SPRINGER LICENSE
TERMS AND CONDITIONS

This Agreement between University of Saskatchewan -- Adam Beitel ("You") and Springer ("Springer") consists of your license details and the terms and conditions provided by Springer and Copyright Clearance Center.

printable details	
License Number	4156590129507
License date	Jul 26, 2017
Licensed Content Publisher	Springer
Licensed Content Publication	Experiments in Fluids
Licensed Content Title	Tomographic and time resolved PIV measurements on a finite cylinder mounted on a flat plate
Licensed Content Author	Rainer Hain
Licensed Content Date	Jan 1, 2008
Licensed Content Volume	45
Licensed Content Issue	4
Type of Use	Thesis/Dissertation
Portion	Figures/tables/illustrations
Number of figures/tables/illustrations	2
Author of this Springer article	No
Order reference number	
Original figure numbers	Figures 8 and 9
Title of your thesis / dissertation	THE EFFECT OF ASPECT RATIO ON THE AERODYNAMIC FORCES AND FREE END PRESSURE DISTRIBUTION FOR A SURFACE-MOUNTED FINITE HEIGHT CYLINDER
Expected completion date	Aug 2017
Estimated size(pages)	150
Requestor Location	University of Saskatchewan 57 Campus Drive Saskatoon, SK s7n5a9 Canada Attn: Adam Beitel
Billing Type	Invoice
Billing address	University of Saskatchewan 57 Campus Drive Saskatoon, SK s7n5a9 Canada Attn: Adam Beitel
Total	**0.00 CAD**

ELSEVIER LICENSE
TERMS AND CONDITIONS

This Agreement between University of Saskatchewan -- Adam Beitel ("You") and Elsevier ("Elsevier") consists of your license details and the terms and conditions provided by Elsevier and Copyright Clearance Center.

printable details	
License Number	4156150663250
License date	Jul 25, 2017
Licensed Content Publisher	Elsevier
Licensed Content Publication	Journal of Wind Engineering and Industrial Aerodynamics
Licensed Content Title	Flow around a cylindrical structure mounted in a plane turbulent boundary layer
Licensed Content Author	Takayuki Tsutsui
Licensed Content Date	May–July 2012
Licensed Content Volume	104
Licensed Content Issue	n/a
Licensed Content Pages	9
Type of Use	reuse in a thesis/dissertation
Portion	figures/tables/illustrations
Number of figures/tables/illustrations	3
Format	both print and electronic
Are you the author of this Elsevier article?	No
Will you be translating?	No
Original figure numbers	Figures 4,6, and 7
Title of your thesis/dissertation	THE EFFECT OF ASPECT RATIO ON THE AERODYNAMIC FORCES AND FREE END PRESSURE DISTRIBUTION FOR A SURFACE-MOUNTED FINITE HEIGHT CYLINDER
Expected completion date	Aug 2017
Estimated size (number of pages)	150
Requestor Location	University of Saskatchewan 57 Campus Drive Saskatoon, SK s7n5a9 Canada Attn: Adam Beitel
Total	**0.00 CAD**

ELSEVIER LICENSE
TERMS AND CONDITIONS

This Agreement between University of Saskatchewan -- Adam Beitel ("You") and Elsevier ("Elsevier") consists of your license details and the terms and conditions provided by Elsevier and Copyright Clearance Center.

printable details	
License Number	4156581186522
License date	Jul 26, 2017
Licensed Content Publisher	Elsevier
Licensed Content Publication	Journal of Fluids and Structures
Licensed Content Title	Flow above the free end of a surface-mounted finite-height circular cylinder: A review
Licensed Content Author	D. Sumner
Licensed Content Date	Nov 1, 2013
Licensed Content Pages	23
Type of Use	reuse in a thesis/dissertation
Portion	figures/tables/illustrations
Number of figures/tables/illustrations	1
Format	both print and electronic
Are you the author of this Elsevier article?	No
Will you be translating?	No
Original figure numbers	Figure 30
Title of your thesis/dissertation	THE EFFECT OF ASPECT RATIO ON THE AERODYNAMIC FORCES AND FREE END PRESSURE DISTRIBUTION FOR A SURFACE-MOUNTED FINITE HEIGHT CYLINDER
Expected completion date	Aug 2017
Estimated size (number of pages)	150
Requestor Location	University of Saskatchewan 57 Campus Drive Saskatoon, SK s7n5a9 Canada Attn: Adam Beitel
Total	**0.00 USD**